INFORMATION TO USERS

This manuscript has been reproduced from the microfilm master. UMI films the text directly from the original or copy submitted. Thus, some thesis and dissertation copies are in typewriter face, while others may be from any type of computer printer.

The quality of this reproduction is dependent upon the quality of the copy submitted. Broken or indistinct print, colored or poor quality illustrations and photographs, print bleedthrough, substandard margins, and improper alignment can adversely affect reproduction.

In the unlikely event that the author did not send UMI a complete manuscript and there are missing pages, these will be noted. Also, if unauthorized copyright material had to be removed, a note will indicate the deletion.

Oversize materials (e.g., maps, drawings, charts) are reproduced by sectioning the original, beginning at the upper left-hand corner and continuing from left to right in equal sections with small overlaps.

Photographs included in the original manuscript have been reproduced xerographically in this copy. Higher quality 6" x 9" black and white photographic prints are available for any photographs or illustrations appearing in this copy for an additional charge. Contact UMI directly to order.

ProQuest Information and Learning
300 North Zeeb Road, Ann Arbor, MI 48106-1346 USA
800-521-0600

Influence of Bubbles on the Water-leaving Reflectance

by

Xiaodong Zhang

Submitted in partial fulfillment of the requirements
for the degree of Doctor of Philosophy

at

Dalhousie University
Halifax, Nova Scotia
November 2001

DALHOUSIE UNIVERSITY

FACULTY OF GRADUATE STUDIES

The undersigned hereby certify that they have read and recommend to the Faculty of Graduate Studies for acceptance a thesis entitled "Influence of Bubbles on the Water-leaving Reflectance" by Xiaodong Zhang in partial fulfillment of the requirements for the degree of Doctor of Philosophy.

Dated: November 23, 2001

External Examiner:

Research Supervisor:

Examining Committee:

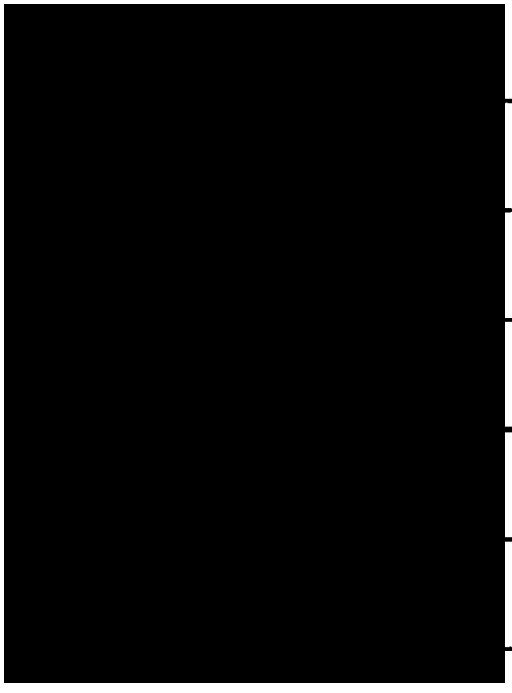

DALHOUSIE UNIVERSITY

Date: November 2001

Author: **Xiaodong Zhang**

Title: **Influence of bubbles on the water-leaving reflectance**

Department: **Oceanography**

Degree: **Ph. D.** Convocation: **May** Year: **2002**

Permission is herewith granted to Dalhousie University to circulate and to have copied for non-commercial purposes, at its discretion, the above title upon request of individuals or institutions.

Signature of the Author

Table of Contents

Table of Contents ..... *iv*
List of Figures ..... *vii*
List of Tables ..... *xi*
Abstract ..... *xii*
List of Abbreviations and Symbols Used ..... *xiv*
Acknowledgements ..... *xvii*
General Introduction *1*
Chapter 1 Volume Scattering Function of Natural Bubble Populations *8*
1.1 Introduction 8
1.2 Theoretical bases and background 10
1.2.1 Normalized volume scattering function 10
1.2.2 Characteristics of bubble populations 11
1.3 Methodology 15
1.3.1 Mie calculation 15
1.3.2 Volume scattering function measurements 15
1.3.3 Laboratory bubble generation 16
1.4 Results 18
1.5 Discussion and conclusions 20
Chapter 2 Volume Scattering Function of Coastal Water *32*
2.1 Introduction 32
2.2 Theoretical bases 33
2.2.1 Definitions 33
2.2.2 Two component system 35
2.3 Instrument and method 36
2.3.1 Volume Scattering Meter 36
2.3.2 VSM data processing 36
2.3.3 Field experiment 38
2.4 Results 39
2.4.1 Amplitude and shape of the VSF 39
2.4.2 Geographic variation 40
2.4.3 Backscattering ratio and its relation to specific angle scattering 40
2.5 Discussion 51
2.5.1 Relative errors 51
2.5.2 Parameter Ω and particle size distribution 52
2.5.3 Variation of phase functions and its implications 53
2.6 Conclusions 56
Chapter 3 Influence of an underwater bubble layer on the spectral reflectance *60*
3.1 Introduction 60
3.2 Background and theoretical bases 62
3.2.1 Bubbles under breaking waves 62
3.2.2 Reflectance at a wind-roughened sea 64
3.3 Method 66

3.4 Results 68
3.4.1 Angular distribution of the background reflectance 68
3.4.2 Spectral distribution of the background reflectance 69
3.5 Discussion 71
3.5.1 Remote sensing reflectance 71
3.5.2 Implication for remote sensing 73
3.6 Conclusions 75
Chapter 4 Optical Influence of Ship Wakes *91*
4.1 Introduction 91
4.2 Background and theoretical bases 92
4.2.1 Ship-generated bubbles 92
4.2.2 Spectral effects of bubbles on the reflectance 94
4.3 Methodology 97
4.4 Results 99
4.4.1 Equatorial Pacific Ocean 99
4.4.2 LEO-15 100
4.5 Discussion 101
4.5.1 Errors in the TSRB algorithm 102
4.5.2 The spectral backscattering coefficients 103
4.5.3 Estimation of the backscattering coefficients for bubbles 105
4.5.4 Effect of turbulence-induced scattering 105
4.6 Conclusions 106
General Conclusions *117*
Appendix A Radiometric quantities and optical properties *120*
A.1 Radiometric quantities 120
A.2 Optical properties 122
A.2.1 Macroscopic IOP's 122
A.2.2 Microscopic IOP's 124
A.2.3 AOP's 127
A.3 Radiative transfer equation 128
A.3.1 Optical models 129
A.4 Bio-optical models 132
Appendix B Natural bubbles *136*
B.1 Mechanics and dynamics of individual bubbles 136
B.2 Stable bubbles 139
B.2.1 Observations 140
B.2.2 Skin model 141
B.2.3 Crevice model 142
B.2.4 Particle model 142
B.3 Natural bubble size distributions 142
B.3.1 Minimum and maximum sizes 143
B.3.2 Shape of bubble size distributions (PDF) 144
B.3.3 Number density N_0 146
B.4 Spatial distribution of bubbles 147
B.4.1 Horizontal distribution 147
B.4.2 Vertical distribution 148

B.5 Effect of bubbles on the acoustic properties of the ocean 150
B.5.1 Resonance frequency 150
B.5.2 Speed of sound 151
B.5.3 Acoustic cross sections 152
References *157*

List of Figures

Figure 1.1 Schematic diagram of the VSM..... 25
Figure 1.2 The single-bubble angular scattering efficiency Q_β for bubbles (black lines) with radius between10 μm and 300 μm are plotted along with the single-particle angular scattering efficiency for particles (grey lines) with refractive index of 1.02, 1.05, 1.10, 1.05 and 1.20 falling in the same size range. Note the critical angle scattering at angles between 60° and 80° separates bubbles from other particles.... 26
Figure 1.3 The calculated phase functions for both clean and coated bubbles with different size distributions, which include populations with a Junge distribution with exponents of -3, -3.5, -4, -4.5 and -5, and a set with bubble size following a normal distribution with mean radius of 20 μm and standard deviation of 10 μm. There is little effect of variations in the size distribution. 27
Figure 1.4 Comparison for the phase functions between laboratory observations and Mie calculations. Bubbles were generated following a normal distribution with mean radius of 20 μm and standard deviation of 10 μm. Because of the reliable angular range of the measurement was from 10° and 170°, the measured data was scaled such that the integrations of the phase function between 10° and 170° for both the measurement and the theoretical calculation are the same..... 28
Figure 1.5 The effect of organic coating on the light scattering by bubbles. The measurement taken before the injection of surfactant is plotted in dotted lines ($\bar{b}_b$=0.196), and the measurement after the injection is in solid line ($\bar{b}_b$=0.318). The inset shows the portion of the angular scattering in the backward directions..... 29
Figure 1.6 The phase functions for clean bubbles with various size distributions. 30
Figure 1.7 The phase functions for a bubbly water as a function of the relative contribution (η) to the total scattering by bubbles..... 31
Figure 2.1 The VSF's were measured at these stations, as indicated by different symbols corresponding to the day of July 2000, when the measurements were conducted. .. 42
Figure 2.2 The mean phase function and its standard deviations of all the measurements observed at the LEO-15 experiment are compared with Petzold's data (denoted as P in the legend).Figure 2.3-a The volume scattering functions estimated for stations with concurrent measurements (550 nm) of the total scattering coefficients (from AC-9 and the values are shown in the legend) are compared with Petzold's VSF data (530 nm)..... 43
Figure 2.3-a The volume scattering functions estimated for stations with concurrent measurements (550 nm) of the total scattering coefficients (from AC-9 and the values are shown in the legend) are compared with Petzold's VSF data (530 nm).. 44
Figure 2.3-b The same as Fig. 2.4-a except the phase functions are plotted..... 45
Figure 2.4 The horizontal variation of phase functions along the A line. Each data line is the mean of the surface measurements at stations along the A line..... 46
Figure 2.5 The variation of the backscattering ratio with depth at Stations A1 and A3... 47
Figure 2.6 The comparison of backscattering ratios estimated from angles between 0.6° to 177.3° (method A) with the estimates from 0.1° and 180° (method B)..... 48

Figure 2.7 The scatter plot of the backscattering ratio estimated using Method B along with the volume attenuation coefficients measured using AC-9. The $r^2 = 0.52$ if the Method A was used. 49
Figure 2.8 The observed parameter Ω at the LEO-15 site. Each curve corresponds to one measurement. 50
Figure 2.9 Ratio of the backscattering coefficient to the volume scattering function at 120° for various particle size distributions simulated by $\sim r^{-\xi}$. The value of ξ varies from 3 to 5, and the minimum radius r_{min} varies from 0.01 to 100 μm. The refractive indexes for particles are assumed to be 0.75 (bubbles), 1.02 (very soft particle containing mostly water), 1.05 (phytoplankton), 1.10 (lipid type particle), 1.15 (hard particle), and 1.20 (calcite particle). 58
Figure 2.10 Effective radius as a function of particle size distribution, which is simulated by truncated Junge distribution. 59
Figure 3.1. The phase function calculated for bubble populations that have been observed in the ocean. The dotted line is the phase function calculated using the analytic formula by Fournier and Forand [*Fournier and Forand*, 1994] with the same backscattering ratio as the bubbles. 79
Figure 3.2-a The angular distribution of the background reflectance ρ_b at 555 nm as a function of exiting zenith angle for the mesotrophic water under various ambient geometric and wind conditions. 80
Figure 3.2-b The increased background reflectance ρ_b at 555 nm as a function of exiting zenith angle simulated for the mesotrophic water for 4 different configurations of incident solar radiance. 81
Figure 3.3-a The background reflectance ρ_b with zero zenith angle as a function of wavelength from 350 nm to 800 nm for various wind speeds for oligotrophic waters. The solar angle is 10°. The inset in the figure is the enlarged plot for the red and infrared wavelengths. The background reflectance at 410 nm measured by Moore *et al.* in equatorial Pacific is shown as a diamond. Solid line is for no wind, and dotted lines, from bottom to top, are for wind speeds of 10, 12, 14, 16, 18, and 20 m s^{-1}, respectively. 82
Figure 3.3-b The same as Fig. 3.3-a except for mesotrophic waters. 83
Figure 3.4-a The enhanced background reflectance with zero zenith angle due to the presence of bubbles as a function of wavelength from 350 nm to 800 nm for various wind speeds for oligotrophic waters. The solar angle is 10°. The inset in the figure is the enlarged plot for the red and infrared wavelengths. Solid lines from bottom to top are for wind speeds of 10, 12, 14, 16, 18, and 20 m s^{-1}, respectively. 84
Figure 3.4-b The same as Fig. 3.4-a except for mesotrophic waters. 85
Figure 3.5. The exponent *l* and the coefficient *j* of Eq. 3.7, as statistically regressed from data shown in Fig. 3.4, are plotted as a function of wavelength from 600 nm to 800 nm. The *l* is scaled to the left y-axis and the *j* to the right y-axis. 86
Figure 3.6. The comparison of the angular distribution of the background reflectances (φ = 45°) calculated for oligotrophic waters containing phytoplankton alone (dotted lines), inclusion of an underwater bubble layer (solid line), and inclusion of a particle layer (solid line with circles). The solar angle is 30°. The vertical distribution profile, the total scattering coefficient and the backscattering ratio are all

the same between the bubbles and the particles. The only difference is that bubbles display critical angle scattering while the particles do not. 87
Figure 3.7-a The remote sensing reflectance (solid line) simulated for one remote sensing pixel for oligotrophic waters at 765 nm as a function of wind speed. The remote sensing reflectance is partitioned into (Eq. 3.4) background reflectance for whitecap-free waters, ρ_b, (line with open circles), and augmented reflectance due to whitecaps, $W\Delta\rho$, (line with closed circles). The reflectance corresponding to 1 digital count for SeaWiFS band 5 is plotted as dotted lines. 88
Figure 3.7-b The same as Fig. 3.7-a except for 445 nm. The remote sensing reflectance is partitioned into (Eq. 3.4) background reflectance for whitecap-free waters, ρ_b, (line with open circles), and augmented reflectance due to whitecaps, $W\Delta\rho$, (line with closed circles). 89
Figure 3.8. The magnitude of the Color Ratio (CR) after wind is compared to CR before wind as a function of wind speed for both oligotrophic (solid line) and mesotrophic (dotted lines) waters. The Color Ratio is defined as the ratio of the reflectance at 445 nm to that at 555 nm. The corresponding errors in chlorophyll estimations (lines with diamonds) are also shown. 90
Figure 4.1 Wakes generated by R/V Mirai at the Equatorial Pacific Ocean. 107
Figure 4.2-a The measured mean reflectances inside (thick lines) and outside ship wakes (thin lines) for Clear Wake experiment. The values shown in the legend are the longitudes and calculated blue-green ratios $\rho_{440\text{-}550}$ for each curve. All the measurements were on the Equator. 108
Figure 4.2-b The reflectance spectra normalized by the total reflectance over the entire spectrum for the station 170.19 W. The spectra are normalized by the integral over the waveband 400-800 nm. 109
Figure 4.3-a The same as Fig 4.2-a except for Turbid Wake experiment. 110
Figure 4.3-b The same as Fig 4.2-b except for Turbid Wake experiment. 111
Figure 4.4 The size distributions of the ship wake bubbles determined by underwater camera observation at the Turbid Wake experiment, and their variation with time. N_0 in the legend denotes the total number density of bubbles that could be resolved by the camera. 112
Figure 4.5 The relative error in the derived upwelling radiance just below the surface based on measurements taken at 0.6 m below the surface. The '+' is for $[Chl] = 0.1$ mg m^{-3}, the 'o' for $[Chl] = 1.0$ mg m^{-3}, the '◊' for $[Chl] = 5.0$ mg m^{-3}, the 'x' is for $[Chl] = 10.0$ mg m^{-3}. 113
Figure 4.6 Spectral variations of $b_b(\lambda)$ normalized at 400 nm for both Clear Wake (dotted lines) and Turbid Wake (dashed lines) experiments. The modeled is $b_b(\lambda)$ also shown (solid line) for comparison. 114
Figure 4.7 The spectral total backscattering coefficient (solid curve) for waters outside of the wakes estimated from Eq. 4.6. Also shown is the backscattering coefficient for particles (dotted curve), derived by subtraction of the theoretical backscattering coefficient of water molecules. 115
Figure 4.8 The estimated backscattering coefficients by wake bubbles from the measurements of the remote sensing reflectances of the ship wakes in the Clear Wake experiment. 116
Figure A.1 Geometry used in defining volume scattering functions. 134

Figure A.2 Schematic views of the geometry of the angular configurations related to in-water and above-water quantities. The zenith angles correspond to the direction of photon travel and are measured from the local zenith for water-leaving radiance (θ) and zenith sun angle (θ_0), or from nadir when dealing with the in-water upwelling radiance (θ'). The azimuth angle φ is 0 and π for the sun and the antisolar directions, respectively. 135

List of Tables

Table 3.1 Field experiments and derived mean radius and optical properties for oceanic bubble populations..... 78
Table B.1 Historical *in situ* bubble measurements in the global ocean and the summaries of measured bubble size and vertical distributions, total number density, and wind speeds..... 156

Abstract

Bubbles in the upper ocean are ubiquitous and are formed primarily as a result of breaking waves, and secondarily as a result of biological activity. This thesis is concerned with the influence of these bubble populations on the optical properties of the upper ocean, primarily scattering, and on the subsequent influence on the radiative transfer of solar energy in the sea.

I have examined the optical properties of oceanic bubble populations from a theoretical, laboratory, and field perspective. Bubbles have a backscattering efficiency at least five times higher than phytoplankton, the most optically important component in the upper ocean. Theoretical predictions and laboratory observations confirm that organic film coatings will further enhance the scattering over the backward direction by a factor up to four. The critical angle scattering by bubbles resulting from the total reflectance at the local water-bubble surface (at angles of 60-80 degrees) is one order of magnitude higher than the scattering by any other particle of similar size. The effects of smaller bubbles (radius $< 10\ \mu m$) on the derived phase function are modeled by assuming that the number of bubbles increases with decreasing size following the Junge distribution. The extension of the bubble size distribution to smaller sizes than are currently measured by a variety of techniques will alter the backscattering ratio of thus derived phase function by less than 20%, as long as the absolute value of the Junge exponent for submicron bubbles is < 3; the most pronounced variations are restricted to angles less than 10°.

Based on historical *in situ* data on natural bubble populations, a model was developed to link the vertical distribution of the bubble layer in the upper ocean with

wind speeds. Based on this model, I estimate that in the visible domain, the increased reflectance in the ocean as a result of strong winds, which produce bubbles and whitecaps simultaneously, is primarily attributable to underwater bubbles. This is in contrast to the common belief that high reflectance of whitecaps should dominate, even though this is true in the infrared wavelengths as our model suggested. As well, the color of the ocean will be shifted towards green. The presence of bubbles will cause an overestimate of chlorophyll concentration from remotely observed spectral reflectance; the situation will be more serious in clear water, where both atmospheric and bio-optical algorithms for ocean color remote sensing are assumed to be largely well constrained. The critical angle scattering of bubbles however, which mostly contributes to light coming out of the ocean at angles greater than 70°, has a limited influence on the remote sensing signals.

Field experiments were conducted to measure the variation of remote sensing reflectance and size distribution of bubbles within the ship wake zone in two different water regimes, namely, clear Equatorial Pacific Ocean and turbid coastal waters of New Jersey. While the color of ship wakes appear greener in clear waters, a shift of reflectance spectra towards blue, albeit slightly, was observed in turbid coastal waters. Colorless themselves, bubbles change the color of the ocean in a way that depends on the spectral backscattering of the background waters. A new method is also proposed to indirectly derive the spectral backscattering, which is difficult to measure correctly, from measurements of remote sensing reflectance, which are easily obtained.

List of Abbreviations and Symbols Used

0^-	symbol indicating the quantity it follows is just below the sea surface
0^+	symbol indicating the quantity it follows is just above the sea surface
A	parameter (coefficient) statistically derived for the natural bubble concentration at surface as a function of wind speed U_{10}
$a(\lambda)$	absorption coefficient (m^{-1})
$b(\lambda)$	scattering coefficient (m^{-1})
$b_b(\lambda)$	backscattering coefficient (m^{-1})
$\overline{b_b}$	backscattering ratio
$b_{b,bub}$	backscattering coefficient due to bubbles
b_p	scattering coefficient due to particles
$\overline{b_{bp}}$	backscattering ratio for scattering by particles
b_w	scattering coefficient due to water molecules (m^{-1})
C	parameter (coefficient) statistically derived for the volume scattering function at small angles as a function of scattering angle
$c(\lambda)$	attenuation coefficient (m^{-1})
CDOM	Colored Dissolved Organic Matter
$[Chl]$	chlorophyll concentration (mg m^{-3})
CR	Color Ratio, defined as a ratio of the background reflectance at 440nm ($\rho_b(440)$) to the background reflectance at 550 nm ($\rho_b(550)$).
CZCS	Coastal Zone Color Scanner
E	irradiance (W m^{-2})
$E_d(0^-,\lambda)$	downwelling irradiance just below the surface (W m^{-2} nm^{-1})
$E_d(0^+,\lambda)$	downwelling irradiance just above the surface (W m^{-2} nm^{-1})
$E_u(0^-,\lambda)$	upwelling irradiance just below the surface (W m^{-2} nm^{-1})
FWHM	Full-Width Half Maximum
f	parameter relating R to the ratio of total backscattering coefficient to the total absorption coefficient
f_{bub}	same as f but for bubbly water
G	a parameter accounting for combined effect of the air-sea interface on transmissions of light into and out of water
GLI	Global Imager
IOP	Inherent Optical Property
I	radiant intensity (W sr^{-1})
j	parameter (coefficient) derived for the elevated background reflectance ρ_{bubble} as a function of wind speed U_{10}.
l	parameter (exponent) derived for the elevated background reflectance ρ_{bubble} as a function of wind speed U_{10}.

$L_u(0^+,\lambda)$	upwelling radiance just above the sea surface viewed at nadir (W m^{-2} sr^{-1} nm^{-1})
$L_w(\lambda,\theta,\theta_0,\varphi)$	water-leaving radiance, which includes contributions from both specularly scattered radiance from foam and radiance backscattered form ocean interior (W m^{-2} sr^{-1} nm^{-1})
m	parameter (exponent) statistically derived for the volume scattering function at small angles as a function of scattering angle
MERIS	Medium Resolution Imaging Spectrometer
MISR	Multi-angle Imaging SpectroRadiometer
MODIS	Moderate Resolution Imaging Spectroradiometer
MOS	Modular Optoelectronic Scanner
$n(r)$	bubble density per unit radius interval at radius r (m^{-3} μm^{-1})
$N(z)$	number density of bubbles at depth z (m^{-3})
N_0	total bubble number density in a unit volume at surface (m^{-3})
OCI	Ocean Color Imager
OCM	Ocean Color Monitor
OCTS	Ocean Color and Temperature Scanner
OCTS-China	China's Ocean Color and Temperature Scanner
OSMI	Ocean Scanning Multispectral Imager
$p(r)$	probability density function for bubble population at radius r (μm^{-1})
POLDER	POLarization and Directionality of the Earth's Reflectance
Q	ratio of the upwelling irradiance to the upwelling radiance, both are defined just below the surface (sr)
$Q_\beta(\psi,r)$	scattering efficiency per unit solid angle for scattering angle ψ and for particle of size r (sr^{-1})
$\overline{Q_b}$	mean scattering efficiency
Q_{bub}	same as Q but for bubbly water (sr)
r	radius (μm)
$R(\lambda)$	diffuse reflectance at wavelength λ defined just below the surface (nm^{-1})
$R_{bub}(\lambda)$	same as $R(\lambda)$ but for bubbly water
r_{eff}	effective radius (μm), defined as the ratio of the third momentum to the second momentum of a bubble size distribution $n(r)$.
r_{max}	maximum radius used in Mie calculation (μm)
r_{min}	minimum radius used in Mie calculation (μm)
$R_{rs}(\lambda)$	remote sensing reflectance at wavelength λ defined just above the sea surface (sr^{-1} nm^{-1})
$R_{rs,bub}(\lambda)$	same as $R_{rs}(\lambda)$ but for bubbly water (sr^{-1})
$\bar{s}$	mean geometrical cross section area (m^2)
SAR	Synthetic Aperture Radar
SeaWiFS	Sea-viewing Wide Field-of-View Sensor
TSRB	Tethered Suspending Radiometer Buoy
U_{10}	wind speed at 10 m above sea surface (m s^{-1})
v	volume (m^3)
VSF	Volume Scattering Function

VSM	Volume Scattering Meter
W	fractional area covered by whitecaps
z	depth (m^{-1})
z_0	e-folding depth for natural bubble populations, which are assumed to decay exponentially with depth (m^{-1})
α	parameter (exponent) statistically derived for the natural bubble concentration at surface as a function of wind speed U_{10}.
$\beta(\psi)$	volume scattering function at scattering angle ψ(m^{-1} sr^{-1})
$\overline{\beta}$	phase function (sr^{-1})
$\overline{\beta}(\psi)$	normalized volume scattering function, or phase function (sr^{-1})
$\overline{\beta}_o$	phase function before bubble injection (sr^{-1})
$\overline{\beta}_b$	phase function due to injected bubbles (sr^{-1})
$\beta_p(\psi)$	volume scattering function due to particles (m^{-1} sr^{-1})
$\overline{\beta_p}(\psi)$	phase function for scattering by particles (sr^{-1})
$\beta_w(\psi)$	volume scattering function due to water molecules (m^{-1} sr^{-1})
$\overline{\beta_w}(\psi)$	phase function for scattering by water molecules (sr^{-1})
$\Delta\rho$	augmented reflectance over the background due to whitecaps (= ρ_f - ρ_b) (sr^{-1})
η	the fractional contribution of bubbles to the total scattering coefficient
θ	zenith angle (with respect to vertical) for radiance (degree)
θ_0	soloar incident angle (with respect to vertical) (degree)
λ	wavelength (nm)
ξ	exponent for a power law distribution (Junge distribution)
$\rho_{440\text{-}550}$	ratio of *R(440)* to *R(550)*
$\rho(\lambda, \theta, \theta_0, \varphi)$	remote sensing reflectance (sr^{-1})
$\rho_b(\lambda, \theta, \theta_0, \varphi)$	background reflectance of foam-free water (sr^{-1})
ρ_{bubble}	elevated background reflectance by the bubble layer (sr^{-1})
$\rho_f(\lambda)$	reflectance of foam-covered water (sr^{-1}), the reflection of foam is assumed to be Lambertian.
$\overline{\sigma_b}$	mean scattering cross section area (m^2)
φ	azimuth angle of radiance relative to the Sun (degree)
ψ	scattering angle (degree)
$\Omega(\psi)$	the ratio of the backscattering coefficient to the volume scattering function at scattering angle ψ(sr)
$\Re$	ratio of $\rho_{440\text{-}550}$ for bubbly water to $\rho_{440\text{-}550}$ for water before bubble injection

Acknowledgements

Special thanks to my supervisor, Prof. Marlon Lewis, whose insight and guidance were irreplaceable during the course of this thesis and whose interest in my welfare have helped me to live a better life and to concentrate on my study. I especially appreciate the opportunities I have had to attend a number of scientific meetings to present various aspects of this work. I would also like to thank Dr. Alex Hay, Dr. Bruce Johnson, and Dr. Ulrike Lohmann, the other members of my supervisory committee, for their continuing and valuable advices and comments. It is a great honor to have Dr. Andre Morel as my external reviewer.

I am grateful to all the staff members at the Department of Oceanography of Dalhousie University. I have enjoyed great pleasure of discussing with Prof. John Cullen, whose rigorous attitude towards science will be benefited for life. The friendship and assistance of Yannick Huot, Daniela Turk, Moritz Lehmann, and Richard Davis were of particular importance in making these years as a graduate student so pleasant. I also thank Wes Paul and Regine Maass for their help in instrument calibrations.

I feel indebted to Juri Seldam of Satlantic Inc. for his help in data processing. Also I thank Scott McLean, Cyril Dempsey, and Geoff MacIntyre of Satlantic for their help in field experiments.

The financial support during the course of this work was provided by the Office of Naval Research of US Navy and is deeply appreciated.

Especially I would like to thank Prof. Ming-Xia He of Ocean University of Qingdao for her constant encouragement. Most of all I want to thank Hong and my parents for their love, patience and support.

General Introduction

The forerunner of all ocean color satellite sensors, the CZCS (1978-1986) [*Hovis et al.*, 1980], has led to a series of increasingly-sophisticated instruments: the deceased OCTS and POLDER operated between August 1996 and July 1997; MOS, SeaWiFS, OCI, OCM, MODIS, MISR and OSMI are currently operating; and OCTS-China, MERIS, MODIS-FM1, GLI, and POLDER-2 are scheduled to be launched in 2001 or later [*IOCCG*, 2001]. In addition to the advancement in the instrumentation, such as better radiometric performance and increased number of spectral channels, these satellite sensors reflect the continuous and increased interests around the world in ocean color variations and applications. For example, satellite ocean color data provide the only practical means for large scale monitoring of the spatial and seasonal variations of near-surface phytoplankton concentration in the ocean [e.g. *McClain*, 1993; *Yoder et al.*, 1993; *Mitchell*, 1994]. These data also provide useful input into evaluations of carbon flux and primary production [*Smith and Baker*, 1982; *Balch et al.*, 1988; *Platt et al.*, 1988; *Dugdale et al.*, 1989; *Morel*, 1991a; *Platt et al.*, 1991; *Sathyendranath et al.*, 1991b; *Balch et al.*, 1992; *Lewis*, 1992; *Antoine et al.*, 1995; *Antoine et al.*, 1996; *Behrenfeld and Falkowski*, 1997; *Field et al.*, 1998], upper ocean heat flux [*Lewis et al.*, 1990; *Sathyendranath et al.*, 1991a], large scale phenomena such as El Niño [*Feldman et al.*, 1984; *Fielder*, 1984; *Chavez et al.*, 1999], and coastal zone management [*Pernetta and Milliman*, 1995].

Ocean color satellite sensors are designed to retrieve the spectral distribution of radiance exiting the ocean. The geometrical and spectral distributions of this water-leaving radiance are governed by the radiative transfer equation and depend on the optical properties of water, its constituents, the air-sea interface, and the incident radiance distribution. To a first approximation, the remote sensing reflectance, $R_{rs}(\lambda)$ ($\equiv \frac{L_u(0^+,\lambda)}{E_d(0^+,\lambda)}$, where $L_u(0^+,\lambda)$ is the upwelling radiance viewed at nadir and $E_d(0^+,\lambda)$ is the downwelling irradiance, and both are defined just above the surface) is proportional to the ratio of the total backscattering coefficient, $b_b(\lambda)$, to the total absorption coefficient, $a(\lambda)$.

The total backscattering and the total absorption coefficients, which are inherent to the water body [*Preisendorfer*, 1976b], are generally partitioned into contributions from pure water, phytoplankton, dissolved organic material, and inorganic particles [e.g. *Gordon et al.*, 1988; *Morel*, 1988]. Each of the substances involved can, in principle, contribute independently according to their concentration and their specific absorption and scattering characteristics.

Water scatters more but absorbs less in shorter wavelengths (violet and blue) than in longer wavelengths (red) [*Morel*, 1974; *Smith and Baker*, 1981; *Pope and Fry*, 1997]; this explains why the color of the open ocean is blue. Besides water, pigment-containing phytoplankton are the predominant optical component in the global open ocean owing to the strong absorption by pigments (especially chlorophyll-a) in the blue and red wavelengths. Their presence tends to change the color of the water to green. The magnitude of this color change, therefore, provides an indication of the abundance of

phytoplankton. Dissolved organic materials absorb strongly at ultraviolet and blue wavelengths [e.g. *Bricaud et al.*, 1981].

The spectral variations of scattering and absorption for water, phytoplankton and dissolved organic matter, and their relative concentration, can explain most of the observed variation in the color of the ocean. However, the overall amplitude of the reflected signal relative to unit surface irradiance, is mainly related to the strength of backscattering processes in the ocean.

The magnitude of pure water scattering cannot account for the magnitude of observed water-leaving radiances; the minimum scattering coefficient observed in the surface ocean at 555 nm is about 0.02 m^{-1} [*Gordon and Morel*, 1983], while the scattering coefficient of pure seawater is 0.0019 m^{-1} at the same wavelength [*Morel*, 1974]. Phytoplankton contribute 50% to 90% of the total volume scattering coefficient as the chlorophyll concentration increases from 0.01 mg m^{-3} to 10 mg m^{-3} [*Morel and Ahn*, 1991]. In oligotrophic water, the heterotrophic organisms, such as bacteria, contribute up to 35%. This is consistent with theoretical studies that suggest that 10% to 90% of the total scattering originates from particles in the size range of 1 to 10 μm in diameter [*Morel*, 1991b; *Stramski and Kiefer*, 1991].

Despite their dominant role in total light scattering, phytoplankton have extremely low backscattering efficiency on both theoretical and experimental grounds [*Morel and Bricaud*, 1981; *Morel and Ahn*, 1991; *Stramski and Kiefer*, 1991]. The backscattering by heterotrophic organisms is about an order of magnitude higher than phytoplankton; however, the accumulated backscattering by bacteria and phytoplankton can only account

for about 10% of the observed particulate backscattering coefficient [*Morel and Ahn*, 1991; *Ulloa et al.*, 1992; *Zhang et al.*, 1998].

There continues to be uncertainty with respect to the sources of the variability in the backscattering process. Theoretical calculations using Mie theory indicate that the missing backscatterers might be in the submicron size range [*Morel and Ahn*, 1991; *Stramski and Kiefer*, 1991; *Ulloa et al.*, 1994]. The analysis of *in situ* optical observations also suggest that the particle size distribution has to be extended down to the submicron range in order to agree with observations [*Beardsley et al.*, 1970; *Gordon and Brown*, 1972; *Brown and Gordon*, 1973; *Brown and Gordon*, 1974]. Recent laboratory observations indicated that marine viruses, whose mean size is 70 nm, are not a major source of backscattering [*Balch et al.*, 2000]. On theoretical grounds, colloids (40 –50 nm) and larger submicron particles (0.5 μm – 1 μm) that are found in natural waters could make sizable contributions to the backscattering if their refractive indices are 1.20 and 1.05 respectively [*Zhang*, 1998].

Bubbles are known to be created in the upper ocean through a variety of mechanisms, including rain drops [*Pumphrey and Elmore*, 1990], melting snow [*Blanchard and Woodcock*, 1957], biological processes [*Medwin*, 1970], outgassing of sediments [*Mulhearn*, 1981], or growth from stable cavitation nuclei due to gas supersaturation [*Johnson and Cooke*, 1981] or supersonic pressure [*Messinó et al.*, 1963]. Under moderate wind conditions, however, most bubbles near the ocean surface are generated by breaking waves [*Blanchard and Woodcock*, 1957; *Kolovayev*, 1976; *Koga*, 1982]. Natural bubble populations have been shown to be involved in a number of physical processes, including ambient noise production [*Urick*, 1986; *Medwin and Breitz*,

1989], interaction with sound waves [*Medwin*, 1970; *Medwin*, 1977], air-sea gas transport [*Thorpe*, 1982; *Farmer et al.*, 1993], formation of marine sea-salt aerosols [*Monahan*, 1986; *Blanchard and Syzdek*, 1988], and participation in oceanic carbon flux [*Monahan and Dam*, 2001].

Zhang *et al.* [1998] proposed that microbubbles in the upper ocean could be responsible for a large portion of oceanic backscattering. Based on average *in situ* measurements of the bubble size distribution and number density (see table B.1), they calculated the total volume scattering and backscattering coefficients for the bubble populations. They also found that organic coatings on bubble surfaces significantly enhance the backscattering efficiency but barely alter the total scattering. Bubbles can potentially explain the unaccounted part of the observed backscattering in the ocean, and through a general increase in the spectral water-leaving radiance, can alter the relative proportion of light in the blue and green wavelengths used to compute the concentration of chlorophyll-*a* in the upper ocean from remote observation of ocean color.

The first overall goal of this thesis is to examine in more detail the angular distribution of light scattering from bubbles. The resulting volume scattering function (VSF) so derived completely determines the optical properties of bubbles since absorption is negligible. The second goal is to examine the influence of bubbles on variations in the surface reflectance, and the consequences for retrieval of geophysical quantities from remote observation of ocean color.

In Chapter 1, the Mie theory of light scattering is used to calculate the volume scattering function (VSF) by bubbles of size ranges that have been observed in the global ocean. Bubbles of similar mean size are reproduced in the laboratory and their volume

scattering functions are measured using a newly designed volume scattering meter (VSM) [*Lee and Lewis*, 2001], and compared with the theoretical derivation. The optical effect of organic film coatings on bubble surfaces is also tested. The possible influence on the VSF by smaller bubbles, whose existence and quantities are still uncertain, is analyzed.

In Chapter 2, field measurements of phase functions in coastal water off New Jersey (LEO-15) are reported in terms of the spatial and vertical variations, and compared with scant historical VSF measurements. The relationship between the phase function and the particle size distribution is examined in detail, and is utilized to infer particle characteristics information at the LEO-15 site based on the observed VSF.

In Chapter 3, a radiative transfer model, HydroLight, is used to investigate the influence of submerged bubbles on the ocean color remote sensing. The spectral and angular distributions of water-leaving reflectances, as affected by bubbles, are estimated as a function of wind speed. The effects on the atmospheric correction and bio-optical algorithms are explored.

In Chapter 4, a particular case of intense bubble injection by ship wakes and its optical effects are examined in detail. The measurements of hyperspectral remote sensing reflectances, and number and size distributions of bubbles, are combined with theory to infer the spectral backscattering coefficients for both bubble free and bubbly waters. Finally, a general discussion and main conclusions of the thesis are given.

The definitions of those optical properties that are relevant to the thesis and their relationship are provided in Appendix A. Appendix B gives a general review of natural

bubbles in terms of their origin, stabilization mechanisms, spatial and size distribution, and their observations

Chapter 1 Volume Scattering Function of Natural Bubble Populations

1.1 Introduction

Remote observations of the spectral distribution of light emitted from the upper ocean provide the only practical means for diagnosing the spatial and seasonal variations of near-surface phytoplankton concentration in the ocean [*McClain*, 1993; *Behrenfeld et al.*, 2001]. These data provide useful input into evaluations of carbon flux and primary production [e.g. *Smith and Baker*, 1982; *Morel*, 1991a; *Field et al.*, 1998; *Behrenfeld et al.*, 2001], upper ocean heat flux [e.g. *Lewis et al.*, 1990], large scale phenomena such as El Niño-Southern Oscillation (ENSO) variations [e.g. *Feldman et al.*, 1984; *Chavez et al.*, 1999], and scientific analysis and management of the coastal zone [*Pernetta and Milliman*, 1995].

Because of their strong absorption in the blue and red, phytoplankton pigments are the major determinant of the spectral distribution of water-leaving radiance ("ocean color"). The amplitude of the signal however, relates largely to the backscattering coefficient. Laboratory observations of various phytoplankton species confirm that their backscattering efficiency is very low [*Ahn et al.*, 1992], a result that is consistent with theory [*Morel and Bricaud*, 1981]. Paradoxically, the concentration of phytoplankton, a major product derived from ocean color remote sensing, only accounts for 5% to 10% of

the particulate backscattering that sets the scale for the water-leaving radiance [*Morel and Ahn*, 1991; *Zhang et al.*, 1998]. There continues to be uncertainty with respect to the sources of variability in the backscattering process in the upper ocean.

Zhang *et al.* [1998] proposed that microbubbles in the upper ocean could be responsible for a large portion of oceanic backscattering. Based on average *in situ* measurements of the bubble size distribution and number density, Zhang *et al.* [1998] calculated the total volume scattering and backscattering coefficients for typical oceanic bubble populations. They found that organic coatings on the bubble surface significantly enhance the backscattering efficiency but barely alter the total scattering. Bubbles can therefore potentially explain the amplitude of observed backscattering in the ocean, and through a general increase in the spectral water-leaving radiance, can alter the relative proportion of light in the blue and green wavelengths used to compute ocean phytoplankton concentration.

Here, we examine the angular distribution of the scattering of light by natural populations of bubbles in the ocean. The resulting volume scattering function so derived completely determines the optical properties of bubbles since absorption is negligible. We present the volume scattering function for both single bubbles, and bubble populations with various size distributions. The theoretical result is compared with new, high precision, laboratory measurement of the volume scattering function of artificially produced bubbles of known size distribution. Finally, the effects on the derived phase function by smaller bubbles, whose existence and number density are still uncertain, are analyzed.

1.2 Theoretical bases and background

1.2.1 Normalized volume scattering function

The volume scattering function $\beta(\psi)$ is defined as the radiant intensity, I, deriving from a volume element in a given direction (ψ), per unit of incident irradiance (E) and per unit volume (dv), i.e.,

$$\beta(\psi) = \frac{I(\psi)}{E\, dv} \ (\mathrm{m^{-1}\ sr^{-1}}) \qquad 1.1$$

For a group of particles, e.g., a bubble population, the volume scattering function $\beta(\psi)$ is computed as

$$\beta(\psi) = \int_{r_{min}}^{r_{max}} Q_\beta(\psi, r)\pi r^2 n(r) dr\,, \qquad 1.2$$

where $Q_\beta(\psi, r)$ with a unit of $\mathrm{sr^{-1}}$, is the scattering efficiency per unit solid angle at scattering angle ψ for a particle of size, r, and can be calculated by Mie theory if the particle is spherical [e.g. *Bohren and Huffman*, 1983]. $n(r)$ ($\mathrm{m^{-3}\ \mu m^{-1}}$) is the bubble number-size distribution, representing the bubble number per unit volume per unit radius interval at radius r. The limits r_{min} and r_{max} denote the minimum and maximum radius of the bubble population. We use Eq. 1.2 to calculate the volume scattering function of a bubble population.

The normalized volume scattering function or phase function,

$$\bar{\beta}(\psi) = \frac{\beta(\psi)}{2\pi \int_{\psi=0}^{\pi} \beta(\psi)\sin(\psi) d\psi} = \frac{\beta(\psi)}{b} \ (\mathrm{sr^{-1}}) \qquad 1.3$$

provides information about the relative angular distribution of the scattering. The denominator of Eq. 1.3 is the total volume scattering coefficient, b (m^{-1}).

If we express the bubble size distribution $n(r)$ as

$$n(r) = N_0 p(r) \qquad 1.4$$

where N_0 (m^{-3}) is the total bubble number density in a unit volume of water, and $p(r)$ (μm^{-1}) is the bubble probability density function at radius r, then $\overline{\beta}$ for the bubble populations depends solely on the size distribution ($p(r)$) and not on the total bubble number density. The backscattering ratio, describing the proportion of the light scattered in the backward hemisphere to the total scattering, can be derived as,

$$\overline{b_b} = 2\pi \int_{\psi=\frac{\pi}{2}}^{\pi} \overline{\beta}(\psi)\sin(\psi)d\psi. \qquad 1.5$$

1.2.2 Characteristics of bubble populations

Despite application of various techniques, including holography [*O'Hern et al.*, 1988], optical reflection [*Su et al.*, 1988], sound speed [*Farmer and Vagle*, 1989], or acoustic backscatter [*Vagle and Farmer*, 1992], the minimum bubble size for a bubble population observed to date in the ocean is about 10 μm. This, however, should be interpreted as a resolution limit of the instruments. The holographic instrument used could not distinguish a bubble from a particle below 10 μm [*O'Hern et al.*, 1988]. The linearity of the calibration curve used for the optical reflection method [*Su et al.*, 1988] is valid only for bubbles larger than 10 μm [*Su et al.*, 1994]. The acoustic resonance frequency for a 10 μm bubble is about 325 kHz at the surface and will increase with

depth [*Clay and Medwin*, 1977]. In acoustic bubble detection, the highest frequency that has been used to date is 200 kHz except in Vagle and Farmer's experiment [*Vagle and Farmer*, 1992], during which one frequency of 400 kHz (bubble resonant size of 8 μm) was used. However, they also indicated that the off-resonant contributions from larger bubbles [*Commander and Moritz*, 1989] is very large at this frequency, making it difficult, if not impossible, to deduce the bubble density at that size.

There have been no *in situ* observations for smaller bubbles. Under laboratory conditions however, stable bubbles between 1 and 10 μm have been observed in both fresh and seawater [*Gavrilov*, 1969; *Johnson and Cooke*, 1981]. Yount [1984] estimated that cavitation nuclei of radii from 0.1 to 1 μm in distilled water exist at densities of ~ 4×10^{10} m^{-3}. It is expected that seawater will host more bubbles than fresh water [*Cartmill and Su*, 1993; *Haines and Johnson*, 1995].

Immediately after wave breaking, entrained bubbles can be larger than 1 mm [*Deane*, 1997; *Deane*, 1999]. These large bubbles quickly rise to the surface leaving behind a diffuse cloud of microbubbles [*Lamarre and Melville*, 1991]. The measured maximum bubble size for the resident bubble population with some persistence is about several hundred microns [e.g. *Medwin*, 1977; *Johnson and Cooke*, 1979].

Early bubble measurements using photographic methods [*Kolovayev*, 1976; *Johnson and Cooke*, 1979] suggested a modal distribution with reported peak radius varying between 40 μm and 100 μm. This contradicted the acoustical measurements [*Medwin*, 1970; *Medwin*, 1977; *Medwin and Breitz*, 1989], which showed that the bubble density continued to increase as the radius decreased from 60 μm to about 15 μm. Walsh

and Mulhearn [1987] suggested that the photographic observations lack the resolution to discriminate smaller bubbles; however, Su *et al.* [1988], using an optical device based on dark-field specular reflection, confirmed a peak located at about 20 μm. Using an acoustical-backscatter technique, Farmer and Vagle [1989] measured bubbles between 8 and 130 μm with a peak at about 20 μm.

From these disparate results, it is difficult to define the general form of the bubble distribution in water, or whether it follows a modal (e.g. Gaussian) or monotonic distribution. However, for the larger part (right side of the peak) of the modal distribution or for the entire monotonic distribution, the bubble PDF, $p(r)$, are found to follow a power law in general, i.e.,

$$p(r) \propto r^{\xi} \qquad 1.6$$

Reported values for the exponent ξ have been between –3 and –7 [*Johnson and Cooke*, 1979; *Walsh and Mulhearn*, 1987; *O'Hern et al.*, 1988; *Su et al.*, 1988; *Vagle and Farmer*, 1992; *Su and Cartmill*, 1994; *Terrill et al.*, 1998]. The value of ξ has also been found to change for small and large portions of the bubble distribution and the pattern of the variation is different for bubbles of different origins.

For example, for wind-generated bubbles, Garrett *et al.* [2000] suggested, based on dimensional grounds, that the initial bubble size spectrum has $\xi = -\frac{10}{3}$; dissolution and rising under buoyancy will modify the spectrum such that the slope is ξ+1 (≈ -2) for bubbles less than 100 μm and is ξ-2 (≈ -5) for bubbles greater than 100 μm. This is consistent with the result observed by Su *et al.* [1988] and Terrill *et al.* [1998] under

windy conditions. This however disagrees with the data from Medwin and Breitz [1989], which showed ξ being –4 for bubbles less than 50 μm and –2.6 for large bubbles. Wu [1994] suggested that these data, especially at large sizes, actually represented newly generated bubbles.

It has also been suggested that the number density of bubbles from other sources would have different size dependence. Cavitation nuclei (< 60 μm) observed in relatively calm seas [*Medwin*, 1977; *O'Hern et al.*, 1988] have ξ of –4 [*Mulhearn*, 1981], and bubble populations (> 60 μm) formed from biological activity or outgassing by decayed sediment have a slope of –2 [*Medwin*, 1970; *Medwin*, 1977; *Mulhearn*, 1981]. Woolf and Thorpe [1991] found that –4 fit most of the results reasonably well and it was also in agreement with their model simulations.

Finally, once generated, natural bubbles with sizes less than 300 μm are coated with a layer of organic film on a time scale of seconds and only for a very small part of their lifetime may bubbles be considered as clean [*Thorpe*, 1982]. The organic film will help to stabilize microbubbles by altering buoyancy and blocking gas transfer [*Yount*, 1979] or by providing mechanical strength [*Johnson and Wangersky*, 1987]. The thickness of the organic coating for oceanic bubbles ranges from 0.01 μm for lipids such as fatty esters, fatty acids, and fatty alcohols, to 1 μm for proteins such as glycoproteins and proteoglycans [see *Zhang*, 1998].

1.3 Methodology

1.3.1 Mie calculation

The deformation from sphericity for a rising bubble of size 500 μm is only 4% [*Thorpe*, 1982]. Therefore natural persistent bubbles can be assumed to be spherical for all practical purposes and Mie theory [*Bohren and Huffman*, 1983] can be used to calculate the angular scattering efficiency ($Q_\beta(\psi,r)$) for clean and coated bubbles. The refractive index of bubbles relative to water is 0.75. In our initial calculations, the maximum bubble radius is set to be 300 μm, and the minimum radius 10 μm. The organic coating is assumed to be of protein origin (the refractive index relative to water is 1.2) with a thickness of 0.1 μm. For comparison purposes, we also calculated $Q_\beta(\psi,r)$ for other particles with relative indices of 1.02, 1.05, 1.10, 1.15 and 1.20.

The bubble size distributions were simulated using 2 general forms; one is a Junge distribution (Eq. 1.6) and the other is a normal distribution (to simulate a modal distribution). Finally, we then considered the consequences of extending the lower limit of the size distribution below that supported by measurements (e.g. < 10 μm).

1.3.2 Volume scattering function measurements

The volume scattering function of bubble populations was measured using a newly designed volume scattering meter (VSM) [*Lee and Lewis*, 2001]. A simple schematic diagram of the VSM is shown in Figure 1.1. The salient design feature of this instrument is that unlike previous volume scattering meters [e.g. *Kullenberg*, 1968; *Petzold*, 1972], the light source and receiver are fixed in position, while the angular

measurement of scattering is achieved by rotating a newly designed periscope prism. This arrangement simplifies the scanning mechanism and allows a high angular resolution of 0.3°. Volume scattering functions over the full angular range can be measured with a single run, which takes one and half a minute. The final volume scattering function is the average of the measurements from 0° to 180° and from 360° to 180°. The light source is a halogen lamp of 50 W with a small-sized filament. During the measurement, a filter centered at 550 nm is used to provide spectral conditioning of the input beam.

Due to spurious scattering contamination for small angles and angles close to 180°, we only use the measurements from 10° to 170° for this analysis, although recent improvements to the device have extended the useful angular coverage to the range from 0.5° to 178°. The total scattering coefficient, b, and backscattering coefficient, b_b, are estimated within this angular range. Because we are only interested in the normalized volume scattering function in this study, this reduced angular range will not affect interpretations of the results.

1.3.3 Laboratory bubble generation

To test the conclusions based on Mie theory, we generated laboratory bubble population of known size, and measured the volume scattering function. Natural seawater (S ~ 35‰) was filtered twice, first through a 1.5 μm filter and then through a 0.2 μm filter. The seawater was decanted into a glass column (20 cm in diameter, 40 cm length), and was bubbled by passing gas through 3 sintered glass frits (4 – 10 μm pore size) to strip off dissolved surface-active material. The seawater was introduced at the top of the

column and removed from the bottom, thus flowing counter to the bubble rise. The residence time of the water in the column was about 20 minutes. Adsorbed organic material was collected as the bubbles collapsed at the surface and was used later as a source of added surfactant. All fittings for the bubbling column were made of Pyrex or Teflon, and all surfaces were carefully cleaned before use. The air used to generate bubbles was passed through a water trap, an active charcoal column, and a 0.2 μm filter.

Bubbles for analysis were generated at a cylindrical frit surface by applying a shear field [*Johnson and Gershey*, 1991]. Bubbles produced in this way follow a normal distribution, whose mean and standard deviation can be controlled by adjusting water and air flow rate, and the pore size of the frit. The controllable mean radius of bubble populations ranges from 15 μm to 100 μm.

A well-defined bubble population with a known mean radius produced in the treated seawater was pumped into the VSM chamber continuously, while the volume scattering function was being determined. The measurements under these conditions are assumed to be representative for relatively clean bubbles. We then added the collected surfactant back into the prepared seawater and created the defined bubble population again. The measurements under this condition are assumed to be representative of bubbles that are coated. It is recognized that it is virtually impossible to remove all surfactant materials from the water, and consequently, bubbles in the first treatment were only relatively cleaner than those in the second.

The continuous pumping of seawater was intended to maintain the bubble number-size distribution during the measurement. Also we took 2 runs (totally about 3 minutes) for each experiment, with each run recording the volume scattering function

twice, i.e., for angles between 0°-180° and between 180° and 360°. We did not notice any significant changes between each measurements and the final data is the average of the four measurements.

1.4 Results

Figure 1.2 shows the theoretical angular scattering efficiencies $Q_\beta(\psi, r)$ for single bubbles, and for other particles (> 10 μm) with various refractive indexes. The most significant feature of the angular scattering distribution by bubbles is the elevated scattering between 60° and 80°, caused by the total reflection at the bubble surface when the incident angle is greater than 48°. The magnitude of this critical angle scattering is at least one order of magnitude higher than the scattering by any other particles.

The effect of the bubble size distribution on the phase function of a bubble population is demonstrated in Figure 1.3. We used a Junge distribution with the exponent set to -3, -3.5, -4, -4.5 and -5, and a normal distribution with mean radius of 20 μm and standard deviation of 10 μm. For a bubble population with sizes normally found in the ocean, the size distribution has a limited effect on the mean volume scattering function. This is not surprising since Zhang *et al.* [1998] found that the exact shape of the size distribution has virtually no impact on the mean total scattering and total backscattering coefficients of bubbles with mean radius larger than 4 μm. This is because the forward angular scattering efficiency does not change very much for large bubbles or particles, while large angle scattering is primarily determined by particle index and structure [*Morel and Bricaud*, 1981; *Zaneveld and Kitchen*, 1995]. The critical angle scattering is clearly visible and is not altered with coatings [*Marston et al.*, 1988]. The coating,

however, elevates the backward scattering relative to clean bubbles. The magnitude of this effect depends on the thickness and refractive index of the film. In general, coated bubbles with a protein film of 0.1 μm thickness scatter about 4 times more than clean bubbles between about 100° and 170°, which is consistent with our previous result [*Zhang et al.*, 1998].

Our theoretical results were tested with observations of a defined bubble population using the volume scattering meter. The bubbles produced in the laboratory experiment followed a normal distribution, but we believe the phase function thus determined is representative of the natural bubble population found in the ocean as justified by Figure 1.3. Figure 1.4 shows the comparison of the normalized VSF between our measurements and the theoretical calculations for normally distributed clean bubbles with mean radius of 25 μm. The critical angle scattering was observed in the artificially produced bubbles and its position and magnitude agreed very well with the theoretical prediction.

The effect of the organic film coating on backscattering is demonstrated in Figure 1.5. The scattering in the backward direction was enhanced after surface-active materials contaminated the bubbles. The backscattering ratio increased from about 0.02 before the injection of the surfactant to about 0.03 after the injection. Zhang *et al.* [1998] estimated that the backscattering ratio for clean bubbles larger than 1 μm is about 0.01; it is likely that our measurement of the backscattering ratio for clean bubbles is higher than the theoretical estimate because the bubbles produced in the first step of the laboratory experiment were not fully clean, and that Fig. 1.5 should rather be interpreted to conclude

that bubbles with a thick film scatter more in the backward direction than bubbles with a thin film. As predicted, the critical angle scattering is not altered with coatings.

1.5 Discussion and conclusions

The angular scattering distribution by natural, persistent bubbles can be predicted precisely by Mie scattering theory because bubbles less than 500 μm are virtually spherical. Rays with incident angles greater than 48° experience total reflection at bubble surfaces; as a result, scattering at angles between 60° and 80° is elevated, with a magnitude at least 10 times higher than the scattering by other particles at these angles. The backward scattering (90° - 180°), which is higher than the scattering by typical phytoplankton, will be further amplified by the organic film coatings, which are ubiquitous. The laboratory observations by the new volume scattering meter confirmed the theoretical calculations.

The major uncertainty in translating these results to prediction of scattering by natural bubbles is due to the unknown size distribution of bubble population in the ocean at very small radius. Despite the use of many different techniques, bubbles below about 10 μm have not been resolved in nature. Johnson and Cooke [1981] reported bubbles stabilized at radius ~3 μm in laboratory experiments, and Yount *et al.* [1984] found stable bubbles in both distilled water and gelatin of radius of 1 μm or less. Lack of observations of bubbles at small sizes prevents us from extending the bubble size distribution down to smaller sizes with confidence. As well, there is controversy over the shape of the size distribution for smaller bubbles, i.e., a continuous increase vs. a rapid drop-off. If the bubble concentration decreases rapidly at small size, then our calculation and observation

of the VSF for bubbles is applicable to natural bubble populations; however, if the distribution is characterized by a continuous increase in the number density as size decreases (although clearly, this must be bounded), then this could change the VSF in a way dependent on the size distribution of the small bubbles.

To address this uncertainty to some extent, we extended the Junge distribution for bubble size down to 1 μm and to 0.1 μm respectively using various slopes. The lower limits of radii chosen here correspond to the smallest bubbles observed under laboratory conditions for seawater [*Johnson and Cooke*, 1981] and distilled water [*Yount et al.*, 1984], respectively.

The original bubble size distribution we used was assumed to follow a Junge distribution with $\xi = -4$ and $r_{min} = 10$ μm, and the phase function for such a bubble population is shown in Figure 1.6 as a solid line. We then extended the bubble distribution down to 1 μm following different exponents, ξ, (Eq. 1.6) and estimated the corresponding phase functions based on the results for clean bubbles. We tested exponents as small as –10 and found no significant changes in the resulting phase functions for angles greater than 10°, most of the variations occur for small angles. The general shape of the VSF, as assessed by the backscattering ratio, changes less than 10%. One of the tests for $\xi = -6$ is shown in Fig. 1.6 as the dashed line.

Similarly, we evaluated the effect for bubbles as small as 0.1 μm. The inclusion of submicron bubbles will change the general shape of bubble phase functions considerably depending on concentrations of these small bubbles. For example, extending the bubble population down to 0.1 μm following an exponent of –4 will more

than double the backscattering ratio (dash dotted line in Fig. 1.6). However, as long as the exponent ξ of Eq. 1.6 is –3 (dotted line in Fig. 1.6) or larger (i.e., slower increase), the backscattering ratio changes by less than 20% in general and again most of the variations are due to scattering at angles less than 10°.

The size distribution of small bubbles could be optically important if these bubbles are present in abundance, however the existence of significant populations of these small bubbles has not been confirmed nor their size distribution measured. The reported laboratory measurement of the bubble phase function, which is determined for bubbles larger than 10 μm, could be used for natural bubbles as long as the bubble size distributions are bounded, i.e., the bubbles are larger than 1 μm or the number density of submicron bubbles increases with a slope of –3 or greater. Moreover, field measurements of volume scattering in waters where bubbles dominate the scattering process can potentially be used to infer information about the size distribution of small bubbles based on Fig. 1.6.

The organic coating on bubbles, which happens almost immediately after bubble genesis, will significantly change the scattering at backward angles but will exert little influence on the critical angle scattering between 60° and 80° (Figs. 1.3 and 1.4). D'Arrigo [1984] characterized the bubble stabilizing substance chemically and concluded that the surfactant material is a natural and ubiquitous degradation product of the light-harvesting chlorophyll a/b-protein, present in almost all marine algae. The ocean contains a large pool of such surfactant material (either dissolved or particulate), and it is more appropriate to use coated instead of clean bubbles in the simulation of the radiative

transfer in the upper ocean based on a full understanding of the variability in the volume scattering coefficient in the upper ocean.

The injection of bubbles will change the shape of the volume scattering function according to,

$$\overline{\beta} = (1-\eta)\overline{\beta_o} + \eta\overline{\beta_b}, \qquad 1.7$$

where the subscripts o and b indicate the background phase function, and that due to injected bubbles respectively, and η is the fractional contribution of bubbles to the total scattering coefficient. Assuming the original phase function is represented by Petzold's data for the deep clear ocean [*Petzold*, 1972], the resulting phase functions for bubbly water are shown in Figure 1.7. Clearly, the presence of bubbles changes the shape of the phase functions. The most significant variation occurs for the critical angular range, where the scattering by bubbles is much higher than by non-bubble particles. The backscattering ratio for the original phase function used is about 0.04, which is the highest among Petzold's observations. It could be envisioned that for waters with lower backscattering ratio, the presence of bubbles will also enhance the proportion of backscattering by virtue of their own high backscattering efficiency [*Zhang et al.*, 1998]. It is now recognized that the angular distribution of scattering of light in the ocean is at least as important as the integral quantity (scattering), and the absorption coefficient, in determining the spectral and angular distribution of the water-leaving radiance, which is the basis for current applications of remote sensing of ocean color [*Mobley et al.*, 2001]. To the extent that bubble populations in the ocean are largely responsible for the amplitude of the backscattered light, and to the extent that their concentration and perhaps size distribution are variable over a range of time and space scales, then these

results are of considerable significance for an accurate diagnosis of biological processes from remotely-sensed observations of ocean color.

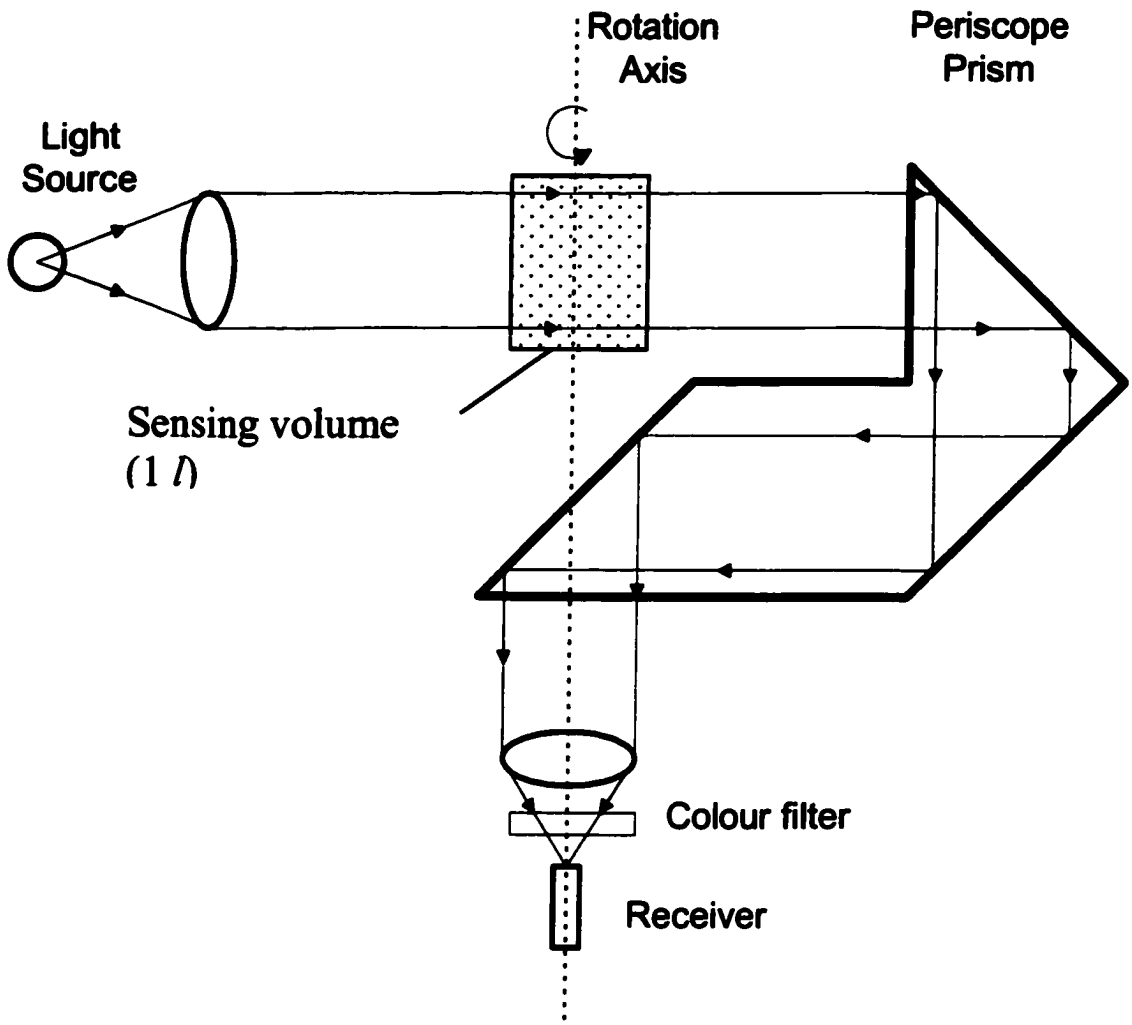

Figure 1.1 Schematic diagram of the VSM.

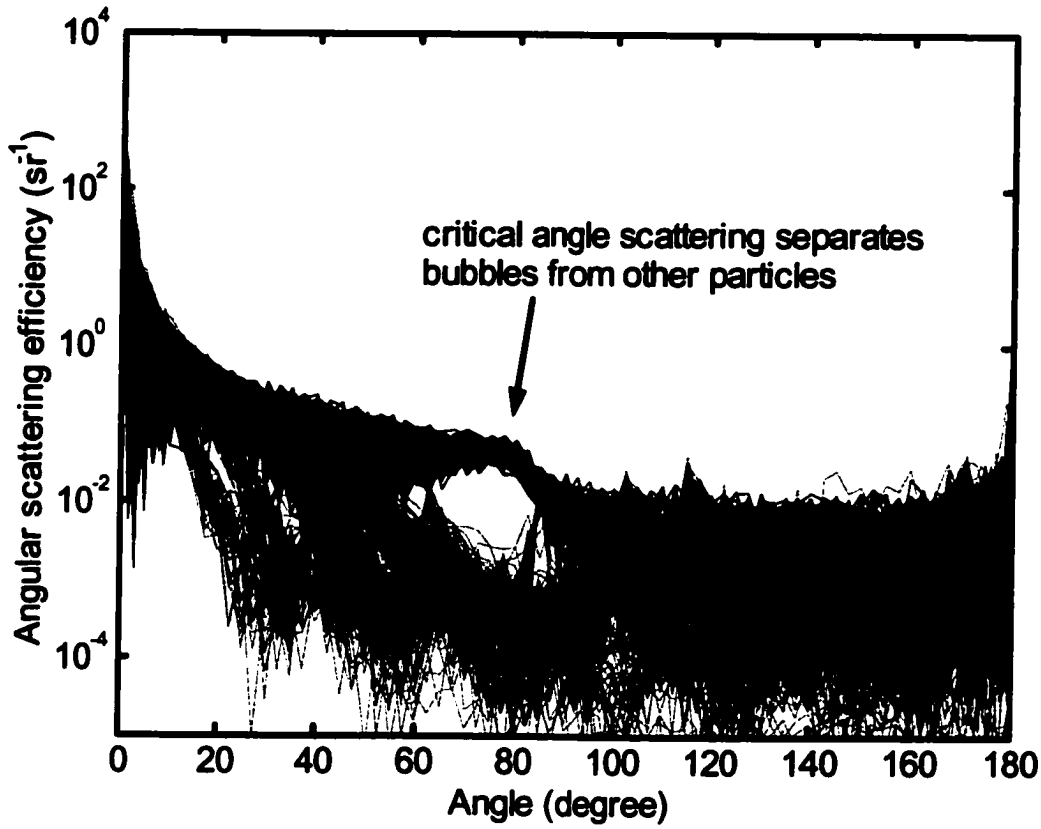

Figure 1.2 The single-bubble angular scattering efficiency Q_β for bubbles (black lines) with radius between10 μm and 300 μm are plotted along with the single-particle angular scattering efficiency for particles (grey lines) with refractive index of 1.02, 1.05, 1.10, 1.05 and 1.20 falling in the same size range. Note the critical angle scattering at angles between 60° and 80° separates bubbles from other particles.

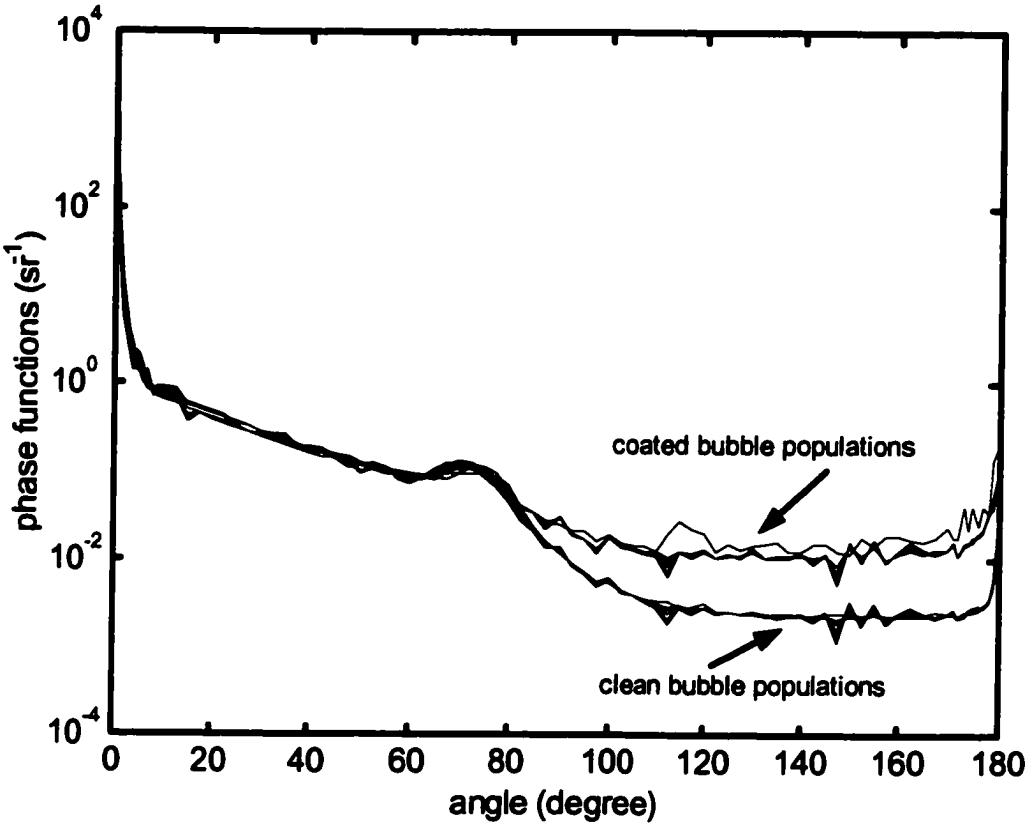

Figure 1.3 The calculated phase functions for both clean and coated bubbles with different size distributions, which include populations with a Junge distribution with exponents of -3, -3.5, -4, -4.5 and -5, and a set with bubble size following a normal distribution with mean radius of 20 μm and standard deviation of 10 μm. There is little effect of variations in the size distribution.

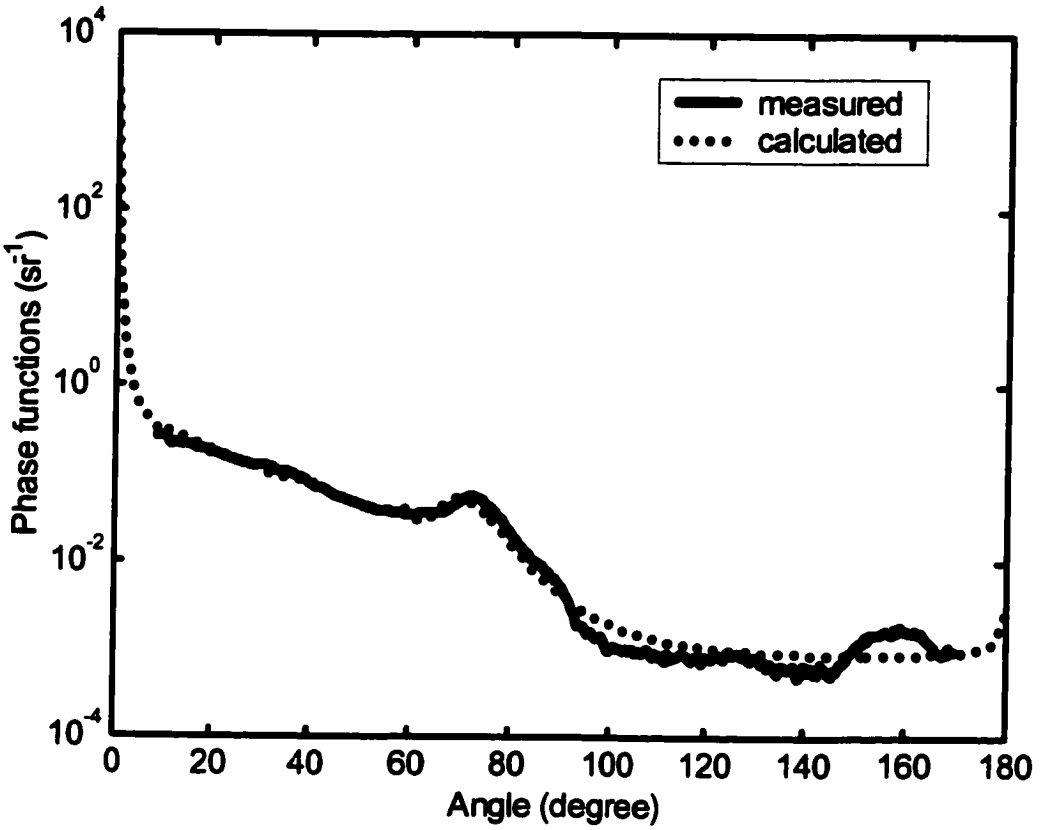

Figure 1.4 Comparison for the phase functions between laboratory observations and Mie calculations. Bubbles were generated following a normal distribution with mean radius of 20 μm and standard deviation of 10 μm. Because of the reliable angular range of the measurement was from 10° and 170°, the measured data was scaled such that the integrations of the phase function between 10° and 170° for both the measurement and the theoretical calculation are the same.

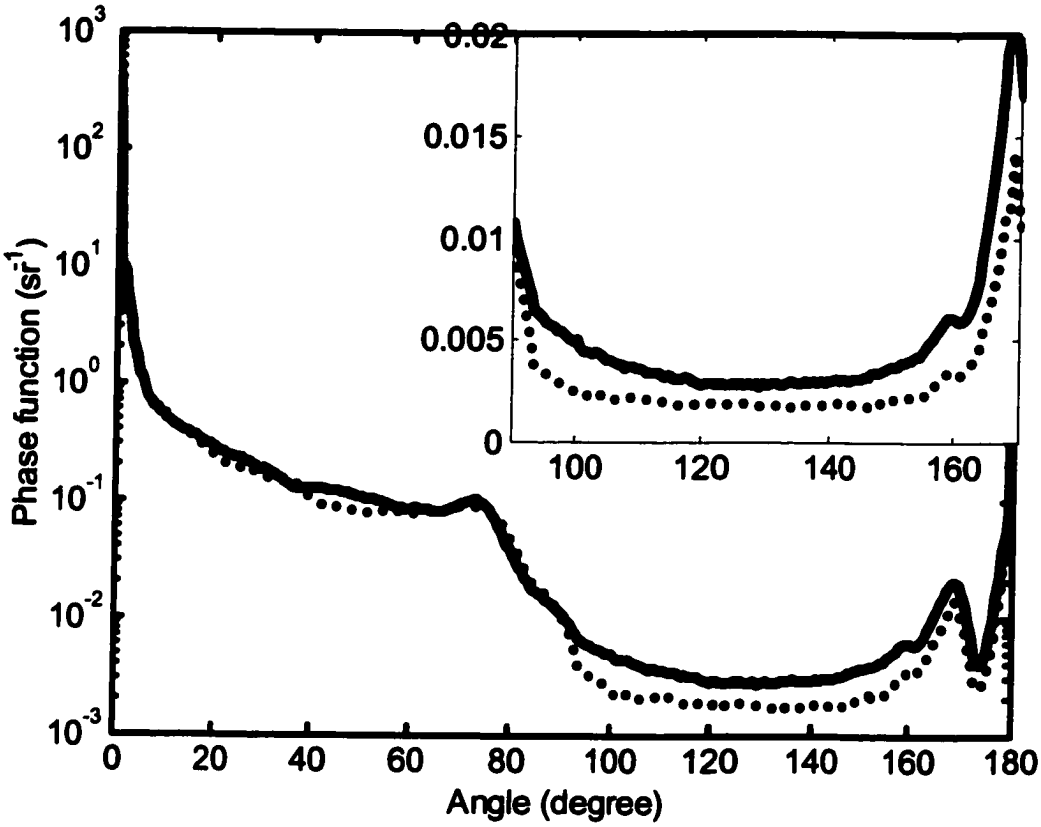

Figure 1.5 The effect of organic coating on the light scattering by bubbles. The measurement taken before the injection of surfactant is plotted in dotted lines ($\bar{b}_b$=0.196), and the measurement after the injection is in solid line ($\bar{b}_b$=0.318). The inset shows the portion of the angular scattering in the backward directions.

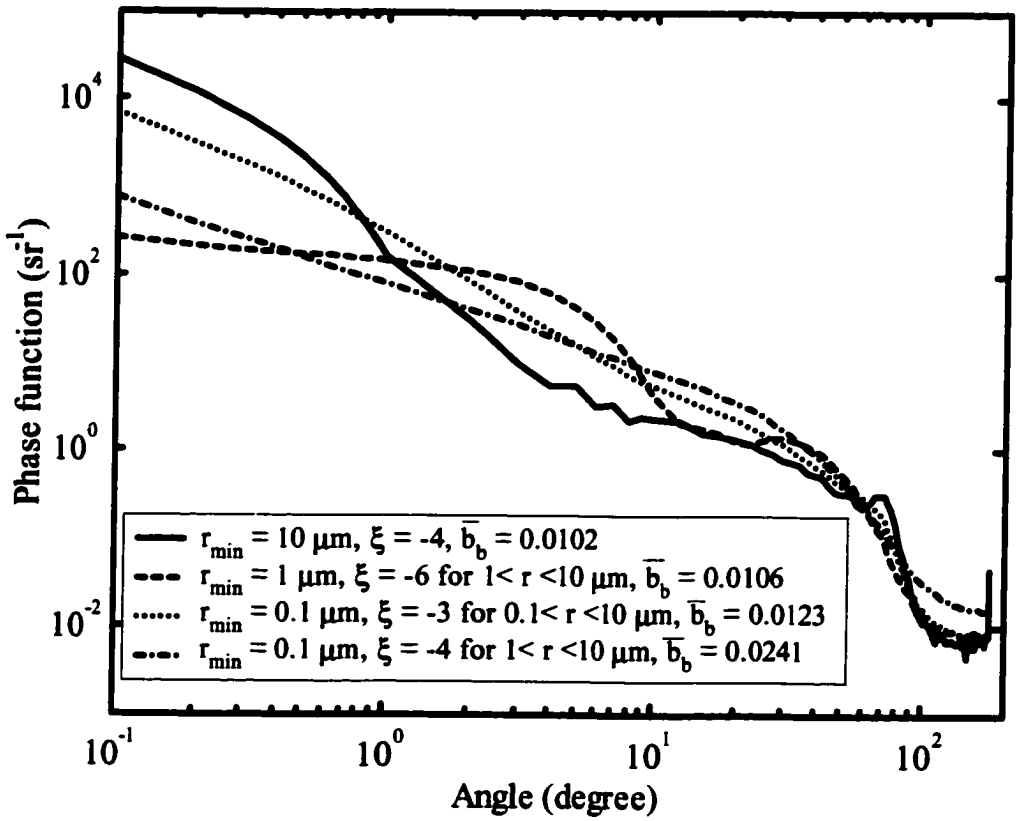

Figure 1.6 The phase functions for clean bubbles with various size distributions.

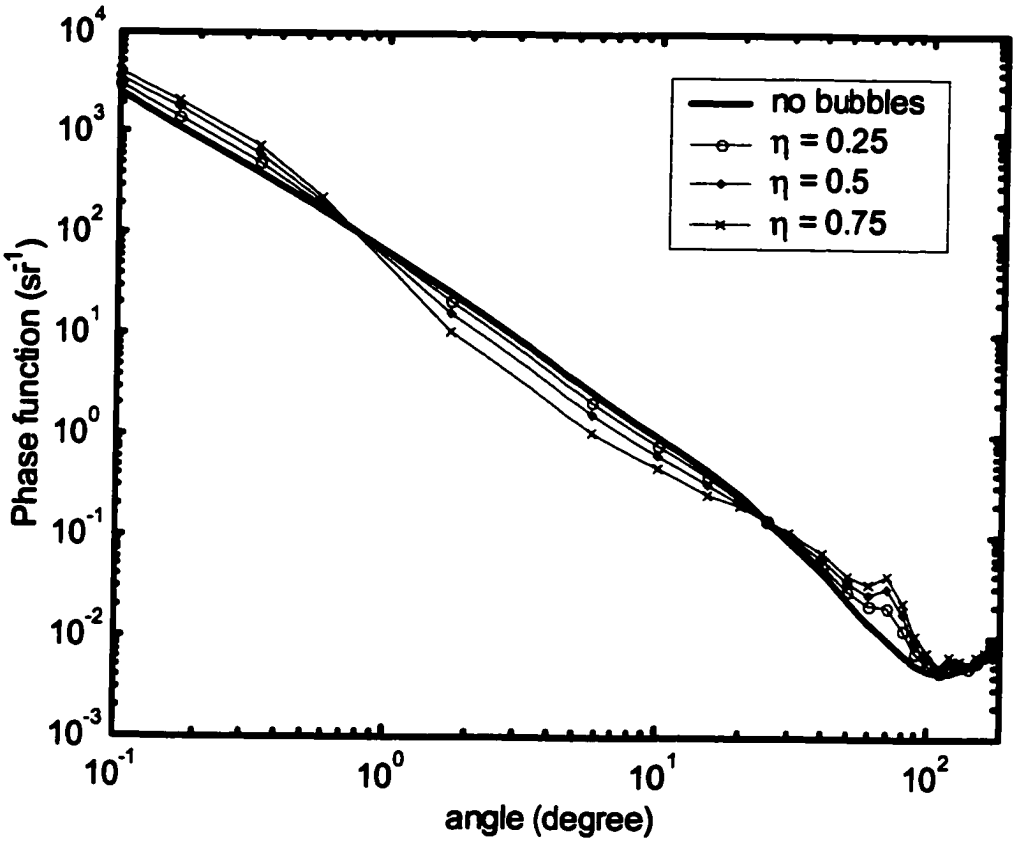

Figure 1.7 The phase functions for a bubbly water as a function of the relative contribution (η) to the total scattering by bubbles.

Chapter 2 Volume Scattering Function of Coastal Water

2.1 Introduction

The volume scattering function and the beam attenuation coefficient are two fundamental inherent optical properties (IOP's) of seawater [*Preisendorfer*, 1976b]. The beam attenuation coefficient, which is routinely measured by commercially available instruments, has been extensively studied [e.g. *Bricaud et al.*, 1995; *Barnard et al.*, 1998; *Loisel and Morel*, 1998; *Claustre et al.*, 1999]. The volume scattering function (VSF) describes the angular distribution of the scattered light and uniquely determines the total volume scattering and total volume backscattering coefficient, the latter of which is an important parameter within the context of ocean color remote sensing [*Gordon and Morel*, 1983]. The actual shape of the volume scattering function, or the phase function, is one of the primary factors that determine the bi-directional remote sensing reflectance [*Morel and Gentili*, 1993; *Zaneveld*, 1995]. Despite its critical role in underwater radiative transfer and ocean color remote sensing, there have been virtually no *in situ* measurements of the VSF in the ocean during the past 30 years.

Morel [1973] provides a thorough review of the historical measurements of the volume scattering function of seawater. Among the *in situ* measurements, the most widely cited experiment was conducted by Petzold [1972] in 1971. He measured the VSF at 530 nm (FWHM = 100 nm) in three locations, near the Bahama Islands, offshore southern California, and in San Diego Harbor, representing three types of water, i.e., deep clear oceanic water, nearshore ocean water, and turbid harbor water, respectively. Two instruments were used. One was a small angle scattering meter (path length 0.5 m)

measuring the scattering at 0°-0.057°, 0.057°-0.114°, 0.114°-0.229°, and 0.229°-0.459°. The other measured the volume scattering function between 10° and 170° in a 10° step. Petzold also performed corrections due to the attenuation along the path length, which he estimated to be about 5%.

A new volume scattering meter (VSM) was developed and tested recently in the lab [*Lee and Lewis*, 2001; *Zhang et al.*, 2001]. In this paper, we present the first field measurements using this VSM in the coastal water of New Jersey. The historical data by Petzold will be reevaluated in terms of its applicability in this coastal region.

2.2 Theoretical bases

2.2.1 Definitions

The volume scattering function $\beta(\psi)$ is defined as the radiant intensity I, from a volume element in a given direction (ψ), per unit incident irradiance (E) and per unit volume (V), i.e.,

$$\beta(\psi) = \frac{I(\psi)}{EV} \ (\mathrm{m^{-1}\ sr^{-1}}). \qquad 2.1$$

For a group of particles with known refractive index and size distribution, the volume scattering function $\beta(\psi)$ could be theoretically estimated as

$$\beta(\psi) = \int_{r_{min}}^{r_{max}} Q_\beta(\psi, r)\pi r^2 n(r) dr, \qquad 2.2$$

where $Q_\beta(\psi, r)$, with a unit of $\mathrm{sr^{-1}}$, dependent on the refractive indexes of both particle and medium, and on size of the particle and light wavelength, is the scattering efficiency

per unit solid angle at scattering angle ψ for a single particle with radius r [*Bohren and Huffman*, 1983]. The $n(r)$ (m^{-3} μm^{-1}) is the particle size distribution, representing the particle numbers per unit volume per unit radius interval at radius r. The r_{min} and r_{max} denote the minimum and maximum radius of the particle population.

Two IOP's, the total volume scattering coefficient, b, describing how much light has been scattered in all directions from the incident light, and the total volume backscattering coefficient, b_b, describing how much has been scattered in all backward directions, can be derived from the VSF

$$b = 2\pi \int_{\psi=0}^{\pi} \beta(\psi)\sin(\psi)d\psi \ (m^{-1}), \text{ and} \qquad 2.3$$

$$b_b = 2\pi \int_{\psi=\frac{\pi}{2}}^{\pi} \beta(\psi)\sin(\psi)d\psi \ (m^{-1}). \qquad 2.4$$

The backscattering ratio, $\overline{b_b} = \frac{b_b}{b}$, gives the fraction of the total scattered radiant flux that is directed in the backward hemisphere. The normalized volume scattering function, or phase function, describing the shape of the angular scattering, is defined as

$$\overline{\beta}(\psi) = \frac{\beta(\psi)}{b}. \qquad 2.5$$

Note that the phase function does not depend on the total particle concentration, and is solely determined by the size distribution, particle shape and particle composition.

In natural waters, the optical properties defined above are often wavelength dependent; the spectral dependence is suppressed for simplicity in what follows.

2.2.2 Two component system

The scattering of natural water can be partitioned into two parts, one due to pure seawater and the other due to particulates,

$$b = b_w + b_p, \tag{2.6}$$

$$\beta(\psi) = \beta_w(\psi) + \beta_p(\psi), \tag{2.7}$$

where the subscript w and p denote water and particulate respectively. Therefore,

$$\overline{\beta}(\psi) = \frac{\beta_w(\psi) + \beta_p(\psi)}{b} = \frac{b_w \overline{\beta_w}(\psi) + b_p \overline{\beta_p}(\psi)}{b}, \tag{2.8}$$

$$\overline{b_b} = \frac{b_{bw} + b_{bp}}{b} = \frac{0.5 b_w + (b - b_w)\overline{b_{bp}}}{b}. \tag{2.9}$$

The scattering properties of pure water are known [*Morel*, 1974] and the its backscattering ratio is 0.5. By measuring the volume scattering function ($\beta(\Psi)$) of a water body, the scattering properties due to particulates can be derived as

$$\overline{\beta_p}(\psi) = \frac{\overline{\beta}(\psi) - \frac{b_w}{b}\overline{\beta_w}(\psi)}{1 - \frac{b_w}{b}}, \text{ and} \tag{2.10}$$

$$\overline{b_{bp}} = \frac{\overline{b_b} - 0.5\frac{b_w}{b}}{1 - \frac{b_w}{b}}. \tag{2.11}$$

An internal check for the measurements of the volume scattering functions in the marine environment is that the total backscattering ratio derived has to satisfy,

$$\overline{b_b} > 0.5 \cdot \frac{b_w}{b} > 0.5 \cdot \frac{b_w}{c} \qquad 2.12$$

where c is the total attenuation coefficient. Eq. 2.12 follows directly from Eq. 2.9.

2.3 Instrument and method

2.3.1 Volume Scattering Meter

A new volume scattering meter (VSM) with a specially designed, telescope-like, prism was developed jointly by Marine Hydrophysical Institute, Ukraine and Satlantic. Inc., Canada [*Lee and Lewis*, 2001]. A salient feature of this VSM is that the light source and the detector are fixed and a rotating prism provides the angular resolution, which eliminates many difficulties in design and calibration. Though capable of measuring spectral volume scattering functions, the volume scattering meter operated at only one wavelength of 550 nm during the experiment reported here. It measures the angular scattering from 0° to 360° with a 0.3° angular resolution and the final result is the average between the measurements from 0° to 180° and 360° to 180°.

2.3.2 VSM data processing

The instrument has yet to be calibrated radiometrically, therefore only phase functions and backscattering ratios estimated are meaningful. Due to contamination by spurious scattering, and uncertainties in volume estimates for angles close to 0° and 180°, only the measurements from 0.6° to 177.3° are used. The integrations of Eqs. 2.3 and 2.4, if performed within this angular range, however, will underestimate b and b_b and will consequently affect the estimates of phase functions and backscattering ratios.

The omission of scattering at these angles mainly influences the estimate of the total volume scattering coefficient, b, because small angle scattering in natural water increases rapidly as the angle approaches 0°, which can be described as a power function,

$$\beta(\psi) = C\psi^{-m} \qquad for\ \psi \le 0.45^{\circ}, \tag{2.13}$$

with the values for m normally between 0 and 2 [*Petzold*, 1972]. However the extrapolation of Eq. 2.13 into small angles would suggest an infinite phase function at 0°. Here, we extend the VSF measurement down to angle of 0.1° by estimating the parameters C and m of Eq. 2.13 from the VSM measurements at angles of 0.6° and 0.9°. We then assume the scattering at 0° is the same as that of 0.1°. The reasons are as follows:

First of all, simulation of small angle scattering confirmed that the scattering caused by turbulence would dominate the scattering for angles less than 0.1° with a magnitude increasing with turbulence strength [*Bogucki et al.*, 1998]. However the volume scattering function simulated does not increase infinitely as angles approaches 0°; it levels off depending on the turbulence strength. For example, at some stations, the extension of Eq. 2.13 down to smaller angles, say, 0.01° would make the derived backscattering too small to meet the internal consistency check described by Eq. 2.12 because the estimated exponent of Eq. 2.13, m, is too steep.

Secondly, as pointed out by Pegau *et al.* [1995], inter-instrument comparisons for IOP's will only be meaningful if the measurements could be matched to ensure the accounting of all scattered light while ensuring no overlapping region where scattered

light is accounted for a second time. The smallest angle that Petzold's instrument could measure for small angle scattering is about 0.1°.

We assume the VSF at angles larger than 177.3° is the same as that of 177.3°. Maffione and Honey [1992] measured the scattering from 178.8° to 180° at Monterey Bay and found an increment of about 10%. Because the calculation of b and b_b will be weighted by $\sin(\Psi)$, where Ψ is the scattering angle, the error associated with this assumption is expected to be small.

2.3.3 Field experiment

The field measurements of the VSF's were carried out at the LEO-15 site off the New Jersey coast from July 18 to 28, 2000. A total of 423 measurements of the VSF were conducted at 20 stations, which are listed in Figure 2.1. Each day is indicated by a different symbol in the figure. The measurements sometimes were taken at several depths at each station. For some stations, there were concurrent measurements of attenuation coefficients and/or absorption coefficients (AC-9, Wetlabs Inc.).

The depth for this coastal area is less than 30 m. The attenuation coefficients at 555 nm range from 2.0 m^{-1} to 5.0 m^{-1}. The extreme value of the attenuation (1 occurrence) of 8.8 m^{-1} was reported inside Great Bay, and the lowest value, 0.47 m^{-1} (1 occurrence) was found at 21 m depth at station 1 along the A line. For comparison, Petzold [1972] measured the attenuation coefficients at 530 nm of about 1.3 – 2.2 m^{-1} for San Diego harbor waters. Based on the attenuation coefficients measured, we divide the LEO-15 site into 3 regions: inside the bay ($c > 4$ m^{-1}), surface coastal ($1 < c < 4$ m^{-1}), and deep coastal ($c < 1$ m^{-1}).

2.4 Results

2.4.1 Amplitude and shape of the VSF

The mean phase function and its standard deviation for all the measurements combined are shown in Figure 2.2 along with Petzold's data. Despite the difference in the total attenuation coefficient, the LEO-15 coastal waters have a very similar phase function as compared to the California coast water in general. The proportion of scattering of California water for angles from 120° to 180°, however, is somewhat higher than that of LEO-15.

The volume scattering functions measured inside the bay (high b) and in the deep coastal water (low b) are shown in Figure 2.3-a. The volume scattering functions are calculated by multiplying the measured phase functions with the total scattering coefficients estimated from AC-9 measurements at stations indicated by arrows in Fig. 2.1. The highest VSF is found inside the bay and the lowest VSF found at the deep coast stations. At LEO-15, the VSF amplitude varies by a factor of about 50 between stations.

The phase functions, corresponding to the VSF in Fig. 2.3-a and shown in Fig. 2.3-b, however, vary over a smaller range (4 fold). In general, the phase functions inside the bay are of similar shape (b_b ratio varies from 0.02 to 0.03). They are, however, quite different from measurements taken in the deep coastal water, which show a lower backscattering ratio, and display a rapidly increased scattering towards 180°. The variability in the observed phase functions found at the LEO-15 site is larger than Petzold's data, which covered a range from deep clear water of open ocean to turbid harbour water. This might indicate a significant transition in terms of the particle size

distribution and composition from inside the bay to deep coastal water at the LEO-15 site.

2.4.2 Geographic variation

We took the average of all the surface measurements during the entire experiment at locations around Station 1, 2, 3 and 4 along the A line (Fig. 2.1) and the resulting phase functions are shown in Figure 2.4. The proportion of scattering at large angles (> 10°) increases shoreward, with the backscattering ratio increasing by a factor of 4.

The backscattering ratios measured from the surface down to 12 meters at Station A3, and down to 21 meters at Station A1 are plotted in Figure 2.5. In both stations, the backscattering ratios have a minimum at about 3 to 5 meters and then increase towards bottom, probably due to the resuspension of sediments.

2.4.3 Backscattering ratio and its relation to specific angle scattering

We compared the estimated backscattering ratio $\overline{b_b}$, using 2 different integration ranges, i.e., one from 0.6° to 177.3° (method A) and the other from 0.1° to 180° (method B), and found that method A systematically overestimated $\overline{b_b}$ relative to method B by about 25% (Figure 2.6). This is primarily due to the underestimate of b by method A due to exclusion of the strong forward scattering at angles less than 0.6°. $\overline{b_b}$ estimated using method A ranges from 0.005 to 0.04 and from 0.003 to 0.035 with method B. Similarly, the overall magnitude of phase functions estimated by method A is about 25% higher than that by method B. Note however, all these errors are systematic and will only

influence the result of cross-instrument comparisons. For self-comparison, the result does not depend on the integration limits.

Figure 2.7 shows the backscattering ratio plotted along with the volume attenuation coefficient, c. Generally, the backscattering ratio increases with the total attenuation coefficient. The correlation coefficient r^2 is about 0.67 for method B and 0.52 for method A.

The ratios of the backscattering coefficient to the volume scattering function (referred to as Ω) are shown in Figure 2.8 for angles between 90° and 180°. Note the value of $\Omega(\psi)$ ($= \frac{b_b}{\beta(\psi)} = \frac{\overline{b_b}}{\overline{\beta}(\psi)}$) does not depend on the absolute calibration of the instrument and the way the VSM data were processed (i.e., method A or method B). Oishi [1990] demonstrated that the value of $\Omega(120°)$ approached a constant value of about 6.9±0.4 sr when small particles dominate. Practically, the HydroScat instrument (HOBI-Lab) measures the scattering at about 140° to infer the backscattering coefficient by assuming a constant value of $\Omega(140°)$ [*Maffione and Dana*, 1997].

As shown in Fig. 2.8, the variability of Ω at each angle is small for angles less than 160°. The mean values of $\Omega(\Psi)$ observed at LEO-15 varied from about 4.6 sr at 90° to about 6.5 sr at 160° and the maximum is 7.3 sr at 140°. The relative error in estimation of b_b by assuming a constant Ω at a certain angle is less than 5% for these waters.

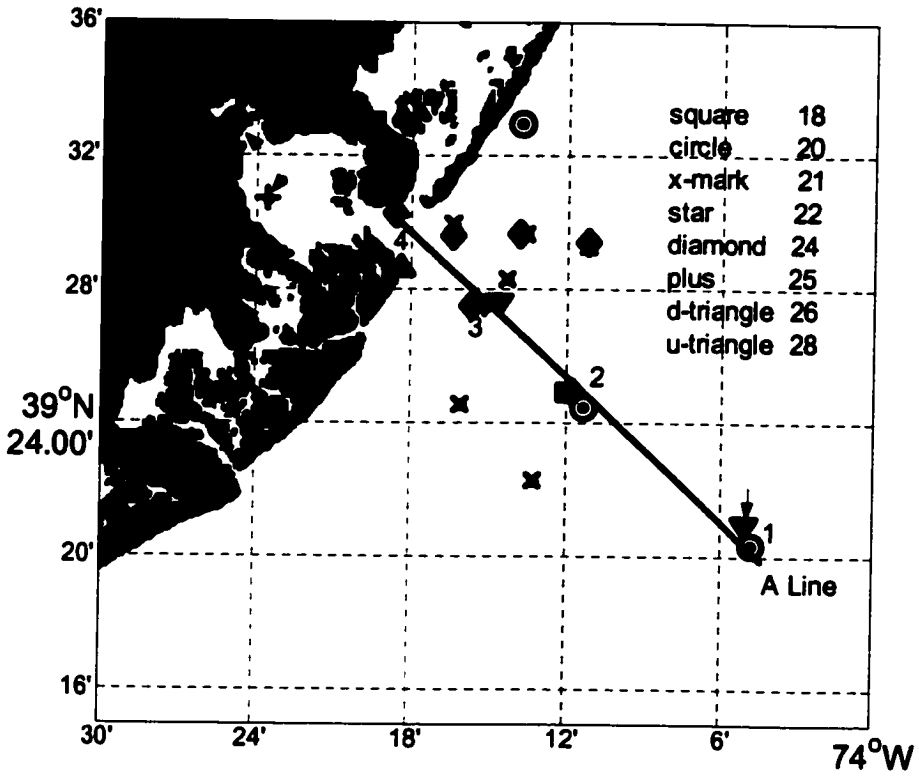

Figure 2.1 The VSF's were measured at these stations, as indicated by different symbols corresponding to the day of July 2000, when the measurements were conducted.

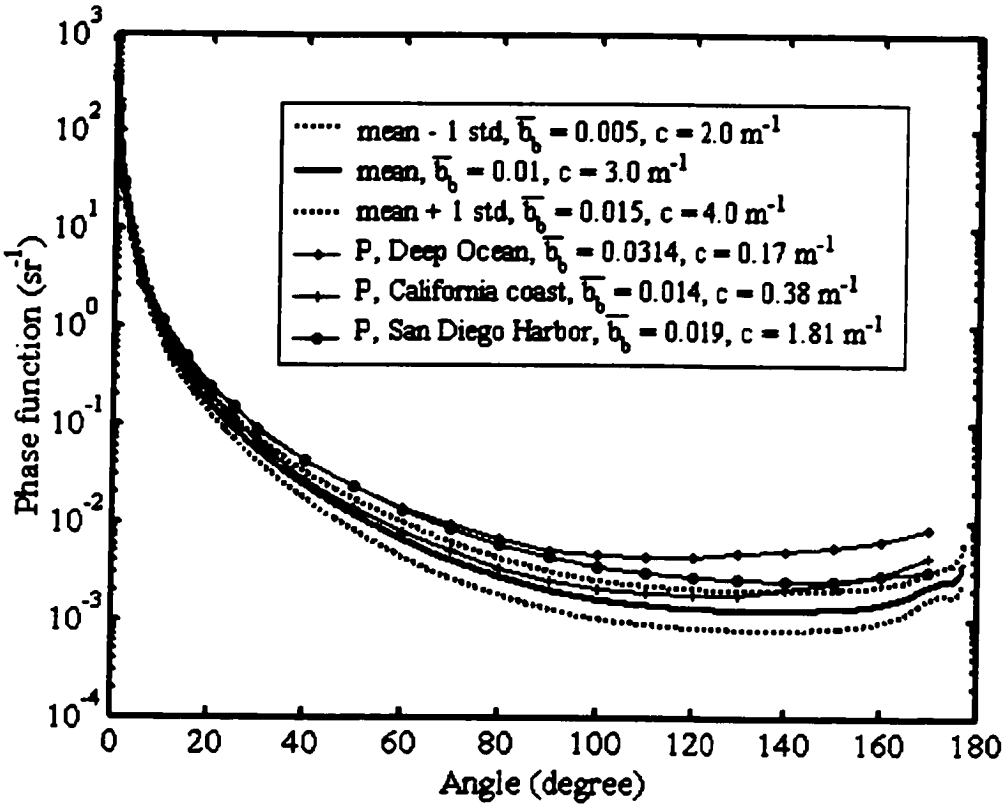

Figure 2.2 The mean phase function and its standard deviations of all the measurements observed at the LEO-15 experiment are compared with Petzold's data (denoted as P in the legend).

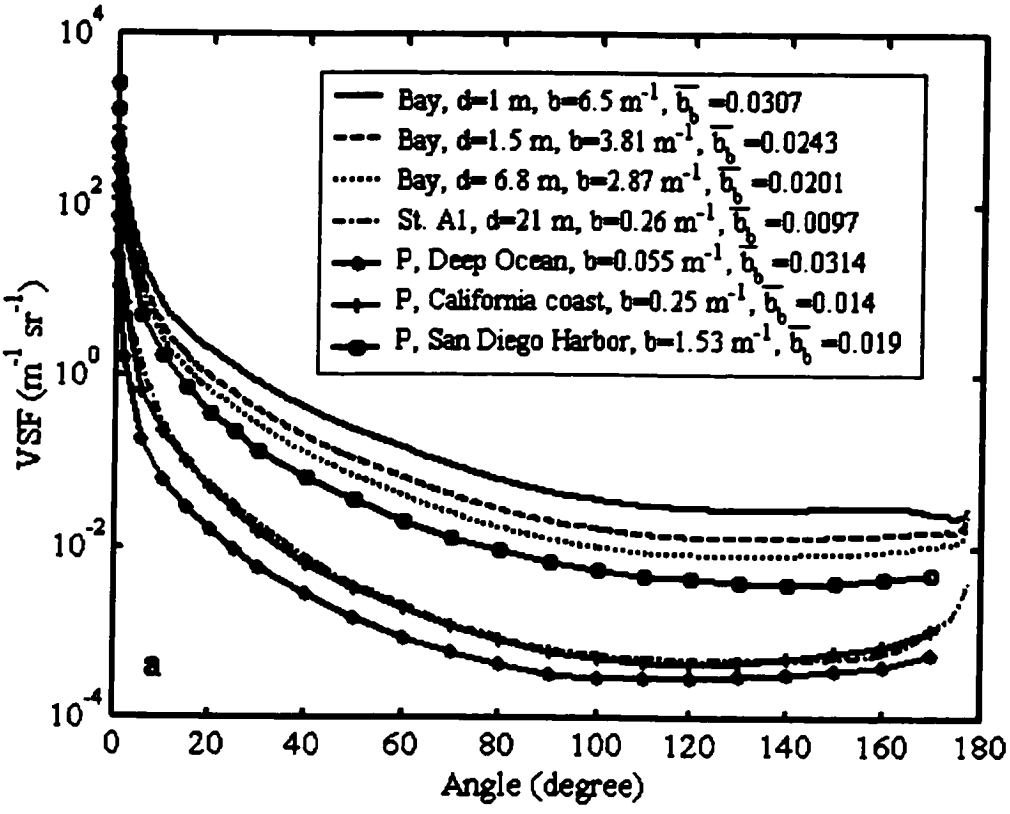

Figure 2.3-a The volume scattering functions estimated for stations with concurrent measurements (550 nm) of the total scattering coefficients (from AC-9 and the values are shown in the legend) are compared with Petzold's VSF data (530 nm).

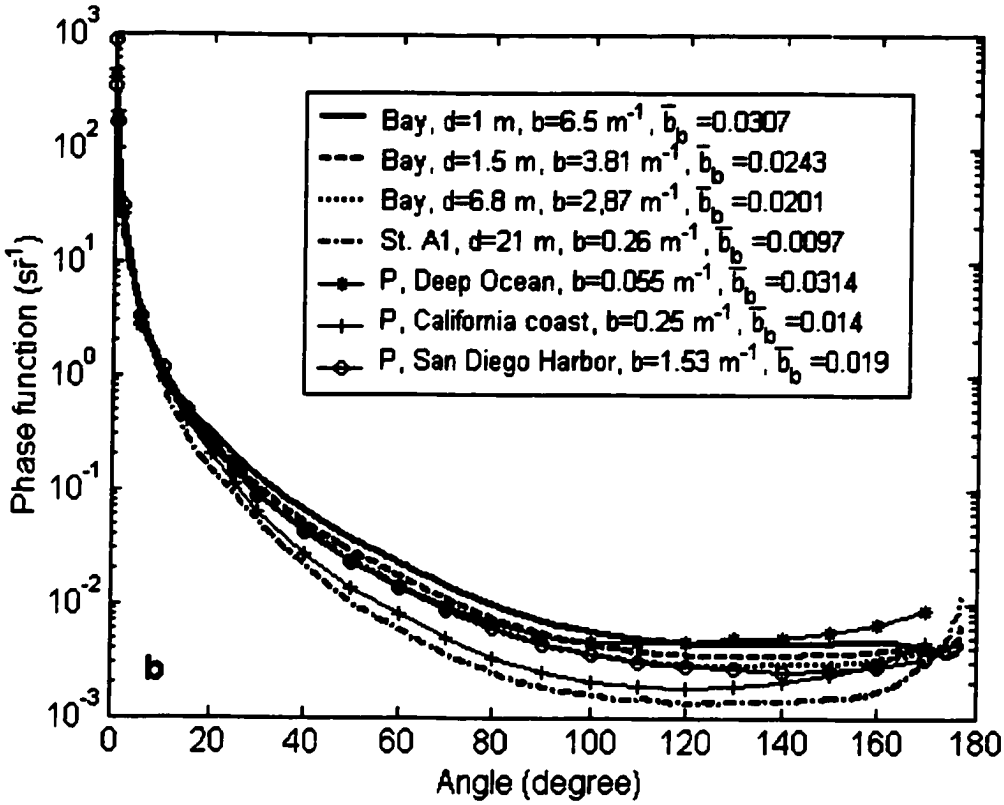

Figure 2.3-b The same as Fig. 2.4-a except the phase functions are plotted.

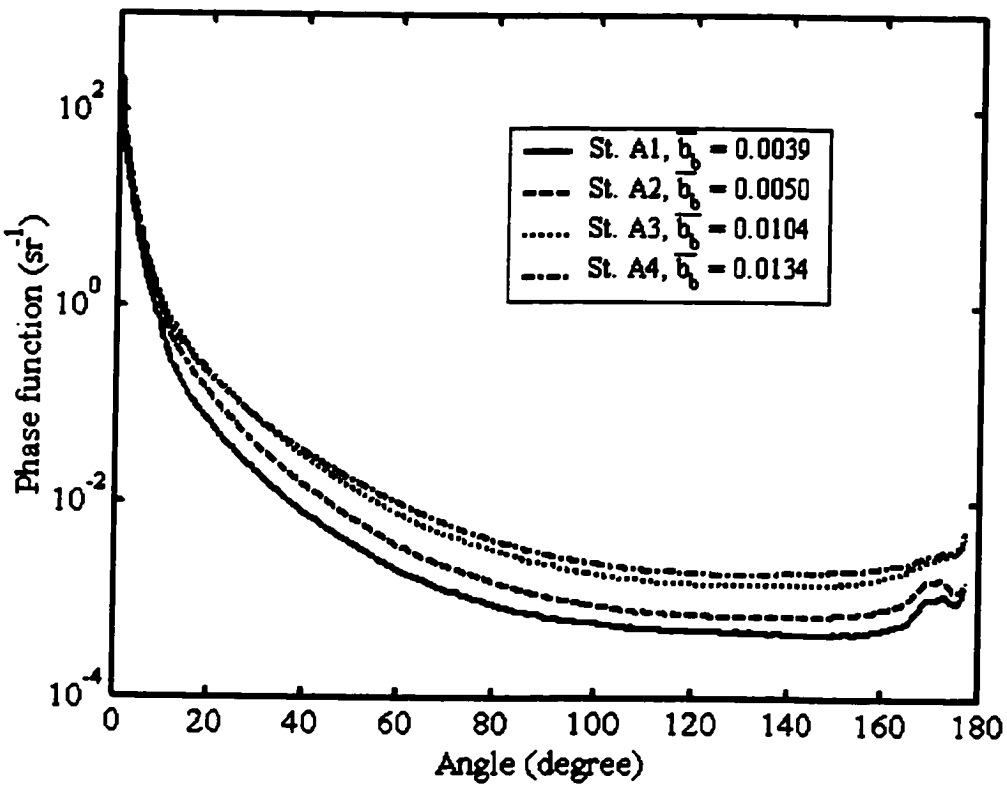

Figure 2.4 The horizontal variation of phase functions along the A line. Each data line is the mean of the surface measurements at stations along the A line.

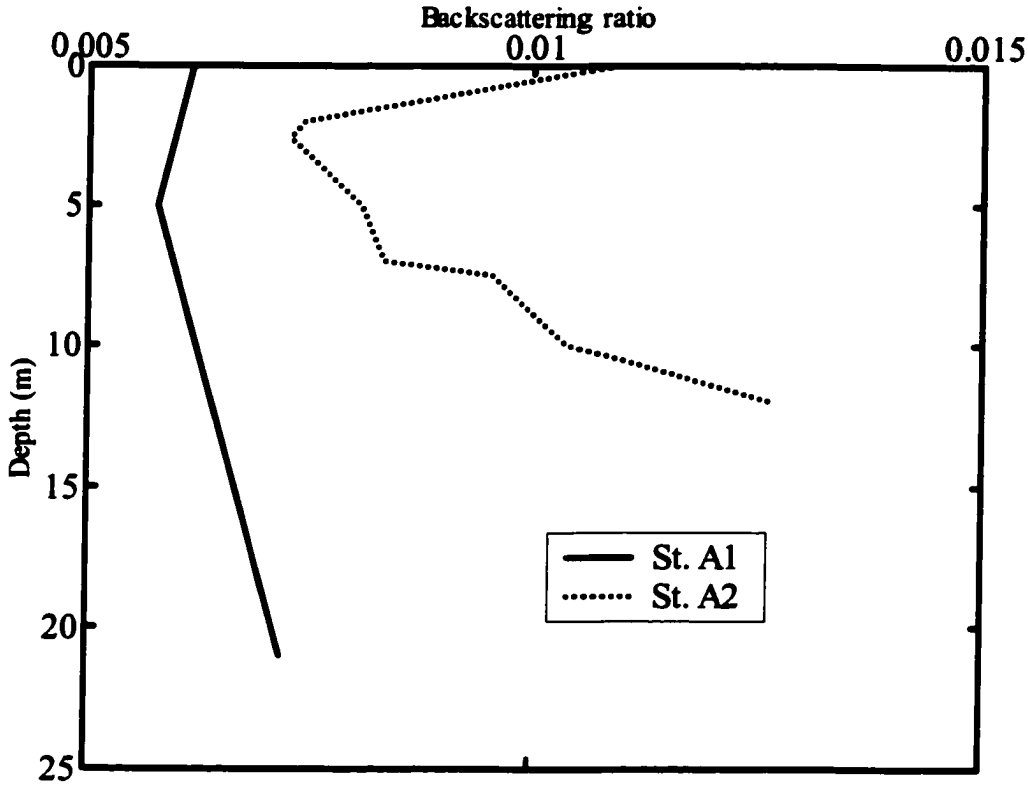

Figure 2.5 The variation of the backscattering ratio with depth at Stations A1 and A3.

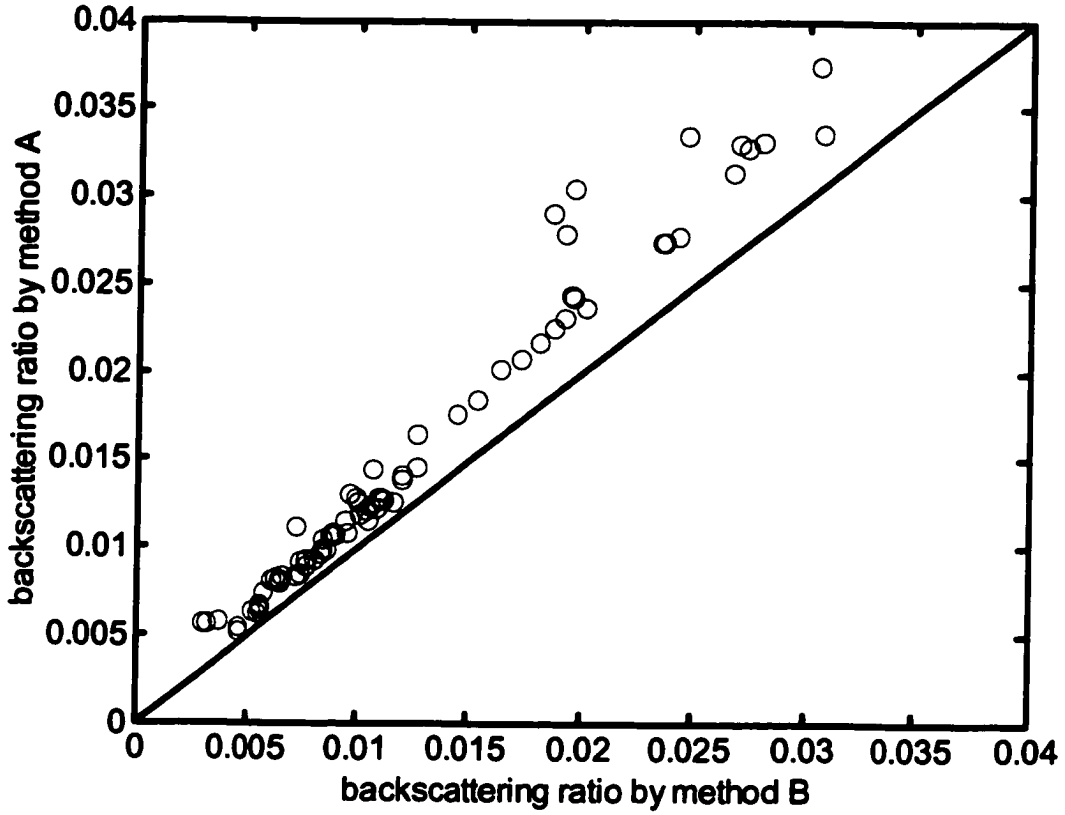

Figure 2.6 The comparison of backscattering ratios estimated from angles between 0.6° to 177.3° (method A) with the estimates from 0.1° and 180° (method B).

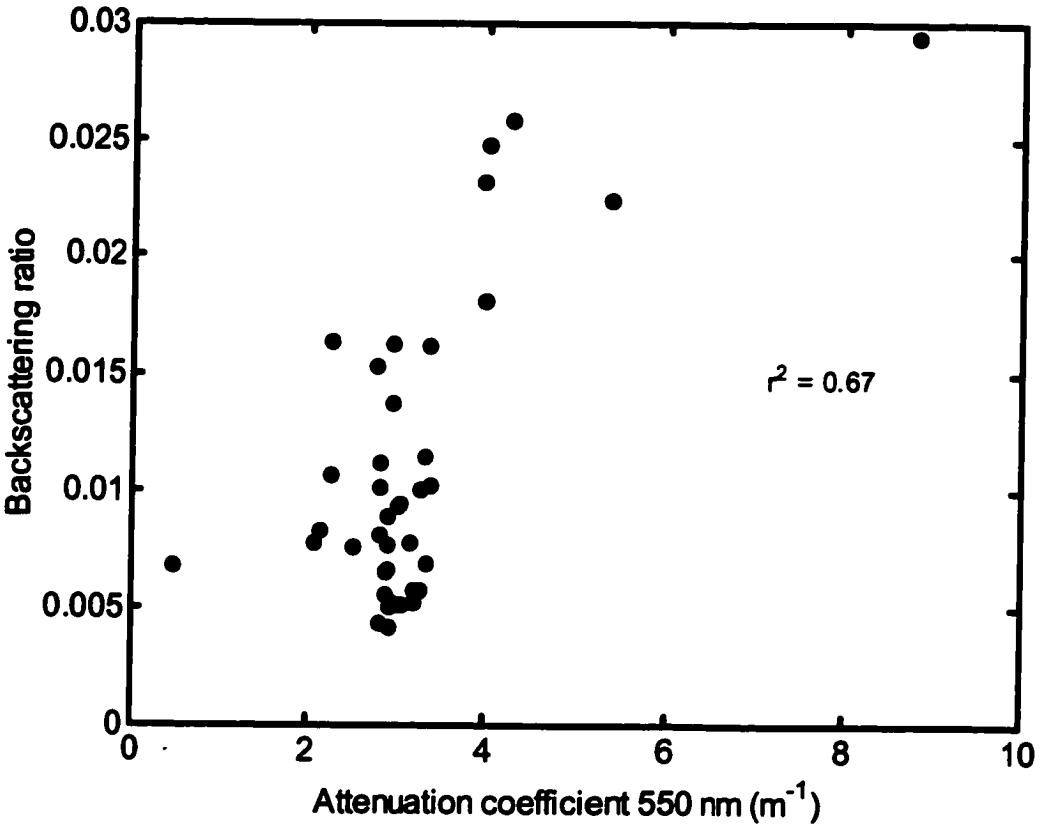

Figure 2.7 The scatter plot of the backscattering ratio estimated using Method B along with the volume attenuation coefficients measured using AC-9. The $r^2 = 0.52$ if the Method A was used.

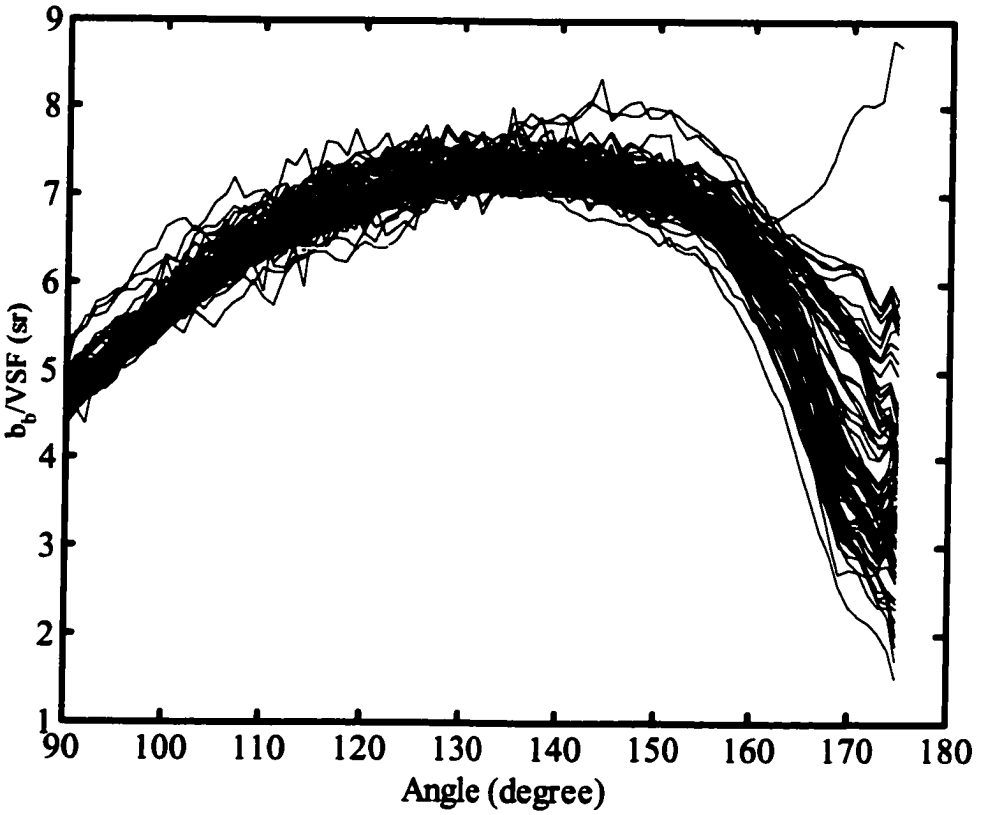

Figure 2.8 The observed parameter Ω at the LEO-15 site. Each curve corresponds to one measurement.

2.5 Discussion

2.5.1 Relative errors

The volume scattering function is one of the most important, yet least studied, IOP's. Since the scattering properties of pure water are well known, the interest is in the scattering by particulates suspended in the sea.

In the above analysis, the phase functions for the entire water sample were used instead and assumed to be representative of the particulates. From Eq. 2.10, the relative error of the assumption is,

$$\frac{\overline{\beta_p}(\psi)-\overline{\beta}(\psi)}{\overline{\beta_p}(\psi)}=\frac{b_w}{b}\left(1-\frac{\overline{\beta_w}(\psi)}{\overline{\beta_p}(\psi)}\right), \qquad 2.14$$

for the phase function, and,

$$\frac{\overline{b_{bp}}-\overline{b_b}}{\overline{b_{bp}}}=\frac{b_w}{b}\left(1-\frac{0.5}{\overline{b_{bp}}}\right), \qquad 2.15$$

for the backscattering ratio.

We estimated that the maximum error and the average error of using directly measured phase functions as representative of the particulate scattering is about 45% and 10% respectively. For the backscattering ratio, the maximum error is 30% and the average error is 5%.

2.5.2 Parameter Ω and particle size distribution

The parameter Ω, defined as the ratio of the backscattering coefficient to the volume scattering function, changes with angles from 90° and 180°; however at a given angle less than 160°, it exhibits a coefficient of variation (ratio of standard deviation to the mean) less than 5%. Figure 2.9 plots the variation of Ω at 120°, calculated by Mie theory, as a function of relative importance of small particles for various particles with different refractive indexes. The particle size distributions are simulated using the truncated Junge distribution,

$$n(r) = const \times r^{\xi}, \quad r \geq r_{\min}, \tag{2.15}$$

where ξ is assumed to vary from –3 to –5, and minimum radius r_{min} to vary from 0.01 μm to 100 μm. The relative importance of small particles is represented by the effective radius, which is defined as

$$r_{eff} = \frac{\int_{r_{min}}^{r_{max}} rn(r)\pi r^2 dr}{\int_{r_{min}}^{r_{max}} n(r)\pi r^2 dr}. \tag{2.16}$$

Figure 2.10 shows the variation of the effective radius as a function of particle size distribution. For particles following the Junge distribution (Eq. 2.15), changes in the minimum radius r_{min}, and the exponent ξ, have the same effect, i.e., changing the proportion of particles of different sizes. The combined effect can be represented by changes in the effective radius.

It is clear from Fig. 2.9 that the ratio Ω changes with the particle size distribution as well as with the refractive index. The value of Ω(120°), however, approaches a constant value (about 6.6 sr) when the effective radius is below 0.1 μm regardless of the refractive index. This is consistent with the measurement at the LEO-15 site (Fig. 2.8). The plot of Ω at other angles (results not shown) also agrees with the measurements. In reference to Fig. 2.10, for r_{eff} to be smaller than 0.1 μm, the Junge type particle size distribution must have an exponent below –4 and a minimum radius less than 0.1 μm. In other words, small particles (< 0.1 μm) appear to dominate the scattering at the LEO-15 site. We have no data on the particle size distribution at LEO-15. However, if it could be represented by a Junge distribution, then based on our measurement, the exponent should be –4 or less and the range should extend down to at least 0.1 μm.

2.5.3 Variation of phase functions and its implications

Phase functions and hence backscattering ratios are determined, to the first approximation, by size distributions and refractive indices of particles. The mean phase function at LEO-15 (Fig. 2.4) is similar to that of California offshore water. However, the phase functions measured at the deep coastal stations and inside the bay (Fig. 2.3-b) form an envelope over the phase functions measured by Petzold, suggesting a larger transition in particle size distribution and composition at the LEO-15 from the bay to coast.

This transition is also manifested by Fig. 2.5, which shows an increasing backscattering ratio from coast to shore. The increase of the backscattering ratio with depth (Fig. 2.6) is probably due to the influence of resuspended sediments.

It has been assumed that the backscattering ratio varies inversely with the chlorophyll concentration [e.g. *Gordon et al.*, 1988; *Morel*, 1988]. This is based on the laboratory observation that large phytoplankton cells, which prevail in waters with high chlorophyll concentration, display low backscattering efficiencies; conversely, waters with low phytoplankton content tend to contain small cells, with relatively higher backscattering ratios. In Case 1 clear water [*Morel and Prieur*, 1977], where the attenuation coefficients were below 1.0 m^{-1}, Loisel and Morel [1998] found that $c_p(660) = 0.407[Chl]^{0.795}$, where $c_p(660)$ is the particulate attenuation coefficient at 660 nm and $[Chl]$ is the chlorophyll concentration. Therefore it could be inferred that the backscattering ratio is inversely related to the attenuation at least for $c < 1$ m^{-1}. Fig. 2.7, however, suggests that the backscattering ratio is positively related to the attenuation coefficient for $c > 1$ m^{-1}. Petzold's data actually also showed a slight increase of backscattering ratio from California coast to San Diego Harbour.

It is expected that the optical properties at the LEO-15 site and in San Diego Harbour are largely determined by non-chlorophyll containing particles. When non-chlorophyll particles dominate, as suggested by Fig. 2.7, the backscattering ratio increases with the attenuation coefficient. Among the factors (particle density, size distribution, refractive index, and particle structure) that affect the attenuation coefficient, the numeric abundance of particles does not affect the estimate of backscattering ratios, which, however, increase with the proportion of small particles and refractive index [*Morel and Bricaud*, 1981] and also change if particles are layered [*Zaneveld and Kitchen*, 1995].

Assuming that the particle concentration (and absorption at 550 nm is negligible) is the only factor that explains the incoherency between the measured backscattering ratio and attenuation coefficient, then about 30% ($\approx 1-67\%$) of the variabilities observed in the attenuation coefficient are due to the variation in particle concentration. The correlation (67%) between the two variables can be accounted for by changes in size distribution, refractive index, and structure, of the particles in the LEO-15 site.

Assuming the conclusion reached in the previous section regarding the particle size distribution at the LEO-15 site applies, namely, small particles less than 0.1 μm in radius prevail throughout the entire experiment site, then the changes in the particle refractive index and structure will explain the positive correlation coefficient found between the backscattering ratio and the attenuation coefficient. For small particles, the higher refractive index increases both backscattering and total scattering (hence total attenuation) coefficient.

On the other hand, for a fixed refractive index, the relative importance of small particles will exert opposite influences on the backscattering and the total scattering, because on theoretical grounds, particles between 1 and 10 μm contribute most efficiently to the total scattering (and hence total attenuation); whereas the dominant particles in the backscattering process are within the range of 0.1 and 0.4 μm [*Morel and Ahn*, 1991; *Stramski and Kiefer*, 1991]. This justifies the inverse relationship found between the backscattering and attenuation coefficient for Case-1 waters, where the refractive index of particles (as dominated by phytoplankton species) does not change very much. The changes in particle size distributions, say by the introduction of one phytoplankton

species of smaller sizes, will on the one hand increase the total attenuation coefficient, and on the other hand decrease the backscattering coefficient.

2.6 Conclusions

The measurements made at LEO-15 site off New Jersey coast by the new volume scattering meter provide the first *in situ* data set of the phase function of natural waters in nearly 30 years. The mean phase function has a backscattering ratio of about 0.01, which is lower than Petzold's measurements. The backscattering ratio was found to increase with the total attenuation coefficient, which is in contradiction with the assumption made based on the laboratory observation of phytoplankton species and the observations in Case 1 clear water with low attenuation coefficients. This is not surprising, since the water is very turbid at LEO-15 and definitely belongs to Case 2 [*Morel and Prieur*, 1977]. Meanwhile, we suggest that caution should be used in modelling the scattering in coastal waters, because the backscattering ratio seemed to increase with the total scattering.

The variations in phase functions observed at LEO-15 are larger than Petzold's observations covering deep clear water, offshore water and harbour water. About 30% of the variability in the light attenuation is due to the variations in the particle concentration, and the rest is due to the changes in the particle size distribution, refractive index and structures (Fig. 2.7). The behaviour of the parameter, Ω, however, suggested that the small particles (< 0.1 μm) predominate light scattering at LEO-15. If this is true, then it is expected that the increase of the backscattering ratio from offshore to inshore (Figs. 2.3-b and 2.4), and towards the bottom, are largely due to the increase of the particle refractive

index, resulting in more light scattered in the backward directions. Bubbles injected by numerous boats transversing the region can also account for the increase of the refractive index [*Zhang et al.*, 1998].

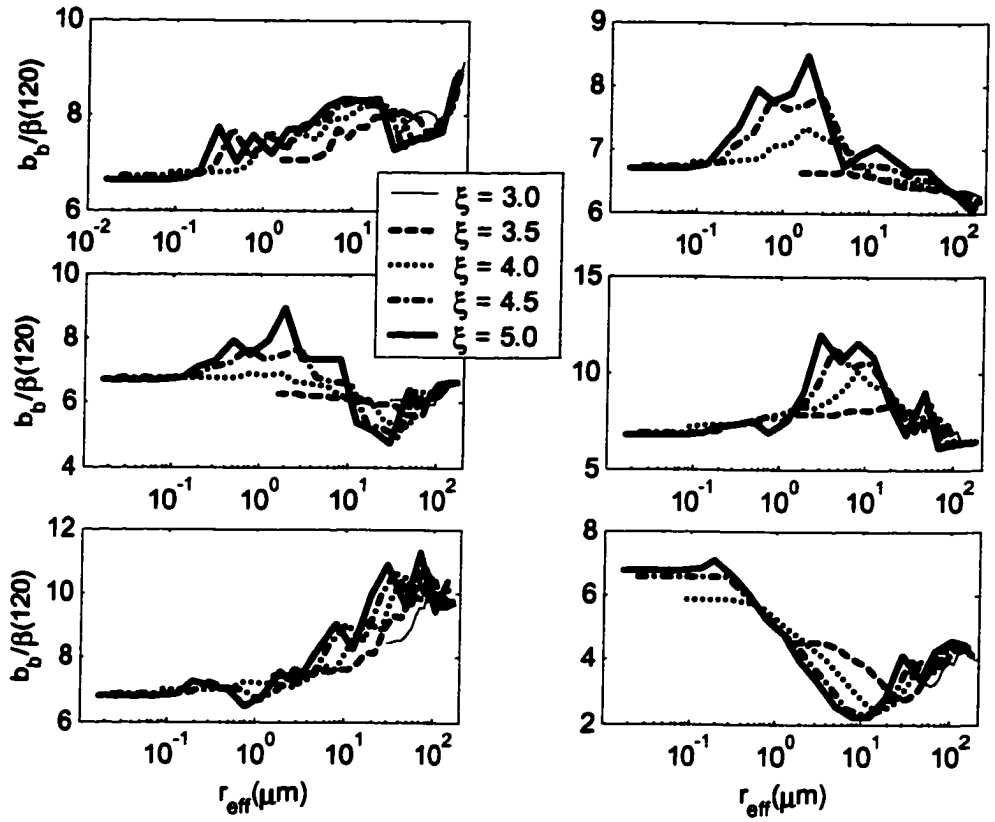

Figure 2.9 Ratio of the backscattering coefficient to the volume scattering function at 120° for various particle size distributions simulated by $\sim r^{-\xi}$. The value of ξ varies from 3 to 5, and the minimum radius r_{min} varies from 0.01 to 100 μm. The refractive indexes for particles are assumed to be 0.75 (bubbles), 1.02 (very soft particle containing mostly water), 1.05 (phytoplankton), 1.10 (lipid type particle), 1.15 (hard particle), and 1.20 (calcite particle).

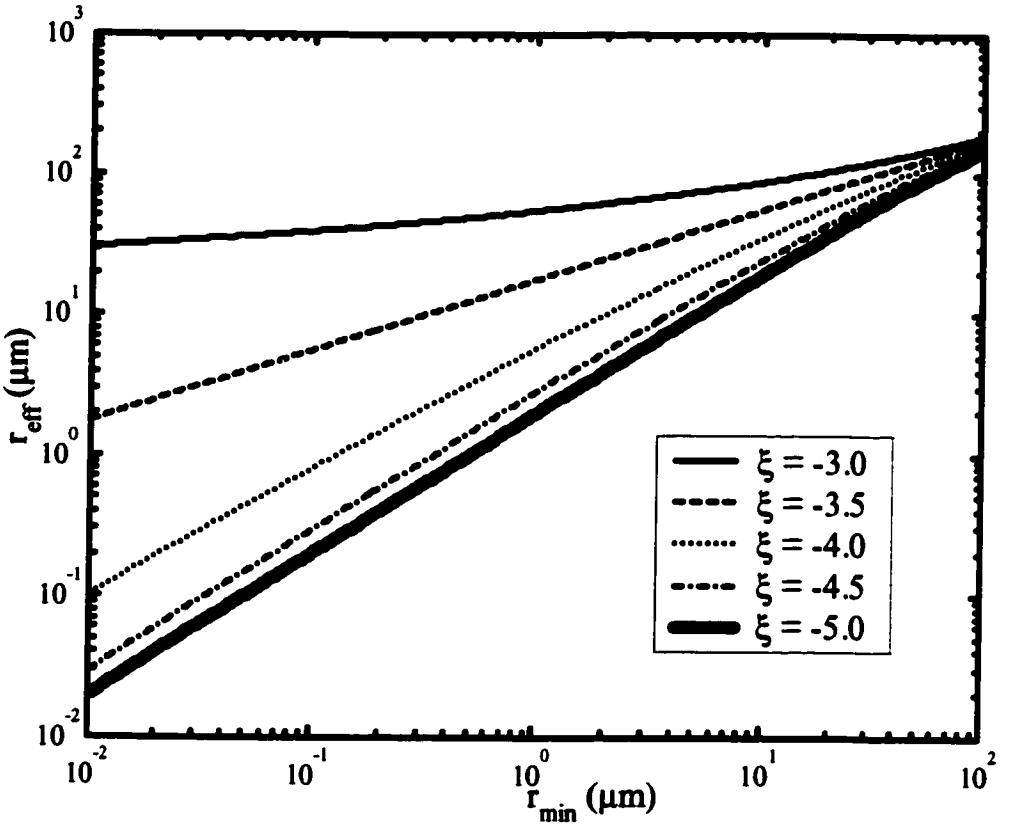

Figure 2.10 Effective radius as a function of particle size distribution, which is simulated by truncated Junge distribution.

Chapter 3 Influence of an underwater bubble layer on the spectral reflectance

3.1 Introduction

Bubbles are known to be created in the upper ocean through a variety of mechanisms, including rain drops [*Pumphrey and Elmore*, 1990], melting snow [*Blanchard and Woodcock*, 1957], biological processes [*Medwin*, 1970], outgassing of sediments [*Mulhearn*, 1981], or growth from stable cavitation nuclei due to gas supersaturation [*Johnson and Cooke*, 1981] or supersonic pressure [*Messinó et al.*, 1963]. Under moderate wind conditions, however, most bubbles near the ocean surface are generated by breaking waves [*Blanchard and Woodcock*, 1957; *Kolovayev*, 1976; *Koga*, 1982]. Natural bubble populations have been shown to be involved in a number of physical processes, including ambient noise production [*Urick*, 1986; *Medwin and Breitz*, 1989], interaction with sound waves [*Medwin*, 1970; *Medwin*, 1977], air-sea gas transport [*Thorpe*, 1982; *Farmer et al.*, 1993], formation of marine sea-salt aerosols [*Monahan*, 1986; *Blanchard and Syzdek*, 1988], and participation in oceanic carbon flux [*Monahan and Dam*, 2001].

In the presence of breaking waves, it has been recognized that the solar reflectivity of the upper ocean will be augmented, conspicuously, by whitecaps or foam (i.e., bubbles on the sea surface) [e.g. *Koepke*, 1986; *Stabeno and Monahan*, 1986], even though bubbles inside the ocean would persist much longer than on the surface [e.g. *Monahan and Lu*, 1990]. The spectral reflectance of whitecaps has been measured both

in the laboratory [*Whitlock et al.*, 1982; *Koepke*, 1984] and in the field [*Frouin et al.*, 1996; *Moore et al.*, 2000]. The presence of whitecaps has also been shown to affect the atmospheric correction of ocean color sensors [*Gordon and Wang*, 1994b].

There has been increased interest in studying the optical effects of submerged bubble populations during the past several years. Stramski [1994] initialized the study of optical scattering by underwater bubble populations. Zhang *et al.* [1998] further developed the theory and found that organic coatings on bubbles will significantly enhance the backscattering. They proposed that bubbles could be the strongest contributor to the light coming out of ocean. Recently, Terril *et al.* [2001] illustrated the temporal variation of light field caused by bubble injection under a wave breaking event (wind speed = 15 m s^{-1}) recorded by acoustic backscattering in offshore water of California, and found variations in scattering over 5 order of magnitude over time periods of O(10) minutes.

While concentrations of bubble populations vary significantly at a specific location under breaking waves, a more or less continuous bubble stratus layer will form as a background over large scales at high wind speeds [e.g. *Thorpe*, 1982; *Monahan and Lu*, 1990; *Zedel and Farmer*, 1991]. The purpose of this study is to examine the influence of this underwater bubble layer on the water-leaving reflectance in both visible and infrared wavelengths in a spatially averaged manner. The effects are further evaluated within an instantaneous field of view of an ocean color sensor in association with whitecaps, which always coexist with submerged bubble populations [e.g. *Wu*, 1992]. We will analyze the result within the context of ocean color remote sensing in

terms of the impacts on atmospheric correction and subsequent derivatives of geophysical products.

In the following, we will first give a review of the field experiments on both underwater bubble clouds and whitecaps, and introduce a model that links the number density and penetration depth of the bubble layer to wind speed. The bubble-induced variations in water-leaving reflectance will be investigated using a radiative transfer model, HydroLight, for waters with various trophic levels under different incident light environment. We conclude with a discussion of potential impacts on ocean color remote sensing.

3.2 Background and theoretical bases

3.2.1 Bubbles under breaking waves

Under the continuous influence of wind stress at the sea surface, waves grow, become unstable locally, and finally break. Breaking waves generate whitecaps at the sea surface and entrain air to produce bubbles in the water. These bubbles are clustered initially under the breakers and distributed subsequently to form an almost horizontally uniform layer immediately below the sea surface [*Monahan and Lu*, 1990; *Wu*, 1994]. The subsurface bubble layers have been observed *in situ* in the Pacific with wind speeds of 10 m s^{-1}, and in the Atlantic with wind speeds of 12 –14 m s^{-1} [*Farmer and Vagle*, 1989]. It has been found that the bubble layer becomes almost continuous when winds are over 7 m s^{-1}, where more intensive and frequent wave breaking can sustain a constant bubble supply [*Thorpe*, 1982; *Thorpe and Hall*, 1983; *Zedel and Farmer*, 1991]. At lower wind speeds the individual bubble clouds remain more distinct [*Thorpe*, 1986a].

The stabilization of bubbles by organic surface coatings or adsorption on to particles also contributes to the formation of this bubble layer [*Johnson and Cooke*, 1981; *Johnson*, 1986]. After the waves cease breaking, the bubbles within the stratus layer will be further diluted by dissolution and rising, and gradually evolve into the background bubble population that can persist hours or even days [*Johnson*, 1986].

Observations have revealed that the lower boundary of the bubble layer is very irregular, corresponding to the bubble plumes injected by breaking waves or carried by Langmuir circulation [*Thorpe*, 1986b; *Zedel and Farmer*, 1991]. The bubble concentration within the subsurface layer varies horizontally, but with a magnitude much less than in the vertical. Therefore, the density of bubbles is normally assumed to be horizontally homogeneous [*Monahan and Lu*, 1990].

Numerous field experiments have found that within the wind-generated bubble layer, the number density of bubbles follows a power law with wind speed but decreases exponentially with depth as described in Eq. 3.1 [*Thorpe*, 1982; *Crawford and Farmer*, 1987; *Walsh and Mulhearn*, 1987; *Wu*, 1988],

$$N(z) = N_0 \exp(-z / z_0), \qquad 3.1$$

where z is depth (m) and N (m^{-3})is the number density. Both z_0 and N_0 are functions of wind speed. By definition, N_0 is the number density of bubbles at the surface, and

$$N_0 = A U_{10}^{\alpha}, \qquad 3.2$$

where U_{10} in m s^{-1} is the wind speed at 10 m above the sea-surface. The value of the exponent α has been estimated to be 3.3 [*Crawford and Farmer*, 1987; *Leeuw and Cohen*, 1995], 3.5 [*Walsh and Mulhearn*, 1987; *Wu*, 1988], 4.3 [*Su et al.*, 1988], 4.5 [*Wu*,

1981], and 4.7 [*Wu*, 1992]. The mean value of α is about 4. Taking this average, and fitting Eq. 3.2 to the data by Johnson and Cooke [1979], the most cited work regarding bubble measurement, we estimate the value of A 66.

The depth of the subsurface bubble layer has also been found to vary with wind speed [*Thorpe*, 1982; *Crawford and Farmer*, 1987; *Farmer and Vagle*, 1989]. The mean e-folding depth, z_0, of the bubble layer can be calculated from data of Thorpe [1982; 1986a] and Crawford and Farmer [1987], and results in

$$z_0 = 0.16(U_{10} - 2.5). \qquad 3.3$$

Eq. 3.3 also agrees well with the measurements by Johnson and Cooke [1979] and by Kolovayev [1976].

3.2.2 Reflectance at a wind-roughened sea

Within the instantaneous field of view (IFOV) of a radiometer observing the ocean surface from an aircraft or space-based platform, the spectral remote sensing reflectance of a wind-roughened sea can be computed as:

$$\begin{aligned} \rho(\lambda,\theta,\theta_0,\varphi) &= W\rho_f(\lambda) + (1-W)\rho_b(\lambda,\theta,\theta_0,\varphi) \\ &= W\,\Delta\rho(\lambda,\theta,\theta_0,\varphi) + \rho_b(\lambda,\theta,\theta_0,\varphi) \end{aligned}, \qquad 3.4$$

where W is the fractional area covered by whitecaps, and ρ_f and ρ_b ($\Delta\rho = \rho_f - \rho_b$) are reflectances of foam-covered and foam-free (background) waters, respectively. The remote sensing reflectance (sr^{-1}) is defined as $\rho(\lambda,\theta,\theta_0,\varphi) = L_w(\lambda,\theta,\theta_0,\varphi)/E_d(0^+,\lambda)$, where $L_w(\lambda,\theta,\theta_0,\varphi)$ is the water-leaving radiance above the surface with zenith angle θ (defined with respect to vertical), and azimuth angle φ relative to the Sun, whose incident

angle is θ_0 (with respect to vertical), and $E_d(0^+,\lambda)$ is the downward irradiance defined just above the sea surface. $L_w(\lambda,\theta,\theta_0,\varphi)$ includes contributions from both specularly scattered radiance by foam (contributing to ρ_f) and radiance backscattered from ocean interior (contributing to ρ_b). The accurate retrieval of spectral ρ_b (say, within 5% for SeaWiFS) from remote observations of ocean surfaces is the goal (as well as a challenge) for the atmospheric correction of satellite remote sensing of ocean color.

Whitlock *et al.* [1982] measured ρ_f of ~0.50 sr^{-1} in the laboratory for the visible and slightly lower values for the longer wavelengths. Taking into account the decay of the reflectance as whitecaps diminish, Koepke [1984] estimated the effective reflectance of whitecaps being of ~0.22 sr^{-1} from 500 nm to 700 nm and about 0.2 at 1 μm.

Frouin *et al.* [1996] measured the spectral variation of ρ_f in the visible and near infrared in a surf zone. The foam reflectance was found to be spectrally constant between 450 nm and 650 nm with an average value of 0.40 sr^{-1}, and decreased to about 0.25 sr^{-1} at 850 nm. Moore *et al.* [2000] measured both ρ_f and ρ_b through equatorial waters of the Pacific Ocean. Their remote sensing augmented reflectances, equivalent to $W\Delta\rho$ of Eq. 3.4 with zero zenith angle, are almost the same for the entire visible band and varied with wind speed as,

$$W\Delta\rho(visible) = 1.08\times10^{-6}\,U_{10}^{2.55}. \qquad 3.5\text{-a}$$

The reflectances in the infrared are observed to be lower, consistent with previous measurements,

$$W\Delta\rho(860) = 0.8\,W\Delta\rho(visible) = 0.87\times10^{-6}U_{10}^{2.55}. \qquad 3.5\text{-b}$$

Previous studies addressing the effect of whitecaps on the atmospheric correction of ocean color remote sensing [*Gordon and Wang*, 1994a; *Frouin et al.*, 1996; *Gordon*, 1997] had assumed that the ρ_b of Eq. 3.4, the reflectance for whitecap-free waters, was the same as when no bubbles were injected. The optical influence of these underwater bubble populations has been shown to be important [*Stramski*, 1994; *Zhang et al.*, 1998], and therefore must be taken into account to correctly model the optical effect of breaking waves within a satellite pixel.

3.3 Method

We used HydroLight [*Mobley*, 1994] to simulate the spectral reflectance with and without wind-generated bubble layers for waters containing varying concentrations of the optically active chlorophyll pigment. The profile of the phytoplankton pigment concentration is assumed to follow a normal distribution superimposed over a background with a constant chlorophyll concentration [*Lewis et al.*, 1983]. For oligotrophic waters, we assume a background chlorophyll concentration of 0.03 mg m^{-3}, and the deep chlorophyll maximum of 0.5 mg m^{-3} is located at 20 m. For mesotrophic waters, the background is assumed to be 0.5 mg m^{-3}, and the chlorophyll maximum is 1.5 mg m^{-3} again at 20 m. Raman scattering, Colored Dissolved Organic Matter (CDOM) fluorescence, and phytoplankton fluorescence are included. The solar incident angle (θ_0 in Eq. 3.4) is 10° and 30°, for oligotrophic and mesotrophic environments, respectively. Wind speed varies from 7 m s^{-1} to 20 m s^{-1}. The penetration depth of the bubble layer, and number density of bubbles at each individual depth is determined by the wind speed through Eqs. 3.1, 3.2 and 3.3. Since we are only concerned with the net effect of

subsurface bubble layers, the exact values regarding the phytoplankton distribution are not very critical, although there are differences in the computed reflectances between oligotrophic and mesotrophic waters.

In order to run HydroLight, we also require phase functions, and the total scattering coefficient for subsurface bubble populations. The minimum radius of a bubble population observed in the ocean is about 10 μm [*O'Hern et al.*, 1988; *Su et al.*, 1988; *Farmer and Vagle*, 1989; *Vagle and Farmer*, 1992]. There are no data on bubble size distributions below 10 μm; the limit, we believe, is imposed by the resolution of the instruments or techniques being deployed. Within the size range of bubbles that have been observed, and based on the theoretical grounds, Zhang *et al.* [2001] found that the volume scattering function (or phase function) of bubbles does not depend strongly on the nature of the size distribution of bubble populations. The mean phase function, as shown in Figure 3.1 and to be used in the following analysis, agrees very well with laboratory measurements [*Zhang et al.*, 2001], as observed by a newly designed volume scattering meter [*Lee and Lewis*, 2001]. In addition to the bubbles strong backscattering, especially when coated [*Zhang et al.*, 1998], a salient feature of bubble scattering is its elevated scattering for angles between 60° and 80°, which is due to the total reflectance of light at the water-bubble interface [*Davis*, 1955; *Marston*, 1979]. The magnitude of the critical angle scattering by bubbles is at least one order of magnitude higher than particles of the same size [*Zhang et al.*, 2001].

The total scattering coefficient by a bubble population is determined as,

$$b = N(z)\overline{Q_b s} = N(z)\overline{\sigma_b}, \qquad 3.6$$

where $\overline{\sigma_b}$ is the mean scattering cross section area, which is in turn determined by the mean cross-sectional area, $\bar{s}$, and mean scattering efficiency, $\overline{Q_b}$. For bubbles of size ranges that have been recorded *in situ*, the mean scattering efficiency $\overline{Q_b}$ is 2 [*Zhang et al.*, 1998], and the values of $\bar{s}$ and $\overline{\sigma_b}$ estimated for different experiments are listed in Table 3.1. The mean value for the observed $\overline{\sigma_b}$ is 3.6×10^{-8} m^2, which will be used for the following analysis. Note that for bubbles of the same number density, $N(z)$, $\overline{\sigma_b}$ will vary with the size distribution. However, given the uncertainty in the relationship between $N(z)$ and wind speed (Eq. 3.2), a constant value of $\overline{\sigma_b}$ (3.6×10^{-8} m^2) is adopted for various wind speeds.

3.4 Results

3.4.1 Angular distribution of the background reflectance

The angular distributions of the background reflectance (ρ_b) at 555 nm in 2 vertical planes (azimuth angles are 45° and 90° respectively) are shown in Figure 3.2-a for both calm ($U_{10} = 0$ m s^{-1}) and rough ($U_{10} = 15$ m s^{-1}) seas with moderate chlorophyll concentration. For calm sea, ρ_b is almost constant with zenith angle up to about 60° and then decreases towards larger zenith angles (the reduction is about 60% for solar angle = 30° and about 30% for solar angle = 10°). The bubble layer created under rough seas will increase the background reflectance over the entire upper hemisphere. The angular shape of the background reflectance also changes toward a more diffusing upwelling radiance field. In contrast to the case for the calm sea, ρ_b increases slightly for zenith angles >

60°; the larger the solar angle, the higher the increment (about 30% when solar angle = 30°).

The enhancement of ρ_b, defined as $\rho_{bubble} = \rho_b(windy) - \rho_b(no\ wind)$, is shown in Fig.3.2-b. For zenith angles (θ) less than 70°, the increased ρ_b due to bubbles is almost the same, regardless of the ambient solar radiance distribution (e.g., Sun incident angles or azimuth angles). Significant enhancement can be found for larger zenith angles (> 70°), and especially for large solar angles. The satellite-detectable increase of remote sensing reflectance ($\theta < 60°$) under windy conditions however, will be uniform within the observational angular range and not dependent on solar angles. Similar results are found for the other wavelengths (results not shown).

3.4.2 Spectral distribution of the background reflectance

The spectral distribution of background reflectances with zero zenith angle (i.e., ρ_b for $\theta = 0°$) under various wind conditions are shown in Figure 3.3 for both oligotrophic and mesotrophic waters. The solar angle is assumed to be 10°. As expected, an underwater bubble layer elevates ρ_b over both visible and infrared bands.

Similar to Fig. 3.2-b, the increased background reflectance, ρ_{bubble} for $\theta = 0°$ is shown in Figure 3.4. In general, more increase in the reflectance is found at shorter wavelengths than at longer wavelength, an effect due to increased absorption by water with wavelength. Note that the enhanced reflectance increases slightly from 750 nm to 800 nm, which is due to the small decrease of water absorption in this spectral range. The enhanced ρ_b shows a broader blue-green peak (Fig. 3.4) in comparison to the

background reflectance spectra (Fig. 3.3), noticeably under strong windy condition. This explains why when a large amount of bubbles are injected, the color of water becomes brighter and greener (in this case), whereas when the injection of bubbles is weak, the color is not strongly affected because the magnitude of the change in reflectance is too small to be perceived.

A visual comparison of the enhanced background reflectances for oligotrophic (Fig. 3.4-a) and mesotrophic (Fig. 3.4-b) waters indicates that the enhanced reflectances for the green and blue bands depend on the bubble population as well as on the trophic level of waters, whereas in the longer wavelengths (the insets of Figs. 3.4-a and b) they seem to be determined by wind speed only. This is because contributions to the water-leaving radiance by multiple scattering between phytoplankton cells and bubbles is more important in the shorter wavelengths; whereas the strong absorption by liquid water in the red and infrared significantly reduces the numbers of photons that have been multiply scattered, and the water-leaving radiance is mainly contributed by single scattered photons. Therefore, it is expected that in the longer wavelengths, the stratus bubble layer alone could account for the elevated background reflectance under windy conditions. We found,

$$\rho_{bubble} = jU_{10}{}^{l}, \qquad 3.7$$

The values of j and l are shown in Figure 3.5 for the red and infrared wavelengths. The exponent l gradually decreases from 4.8 at 600 nm to about 4.1 at 740 nm and then remains almost a constant up to 800 nm. A comparison of the value of l with the exponent α of Eq. 3.2 (assumed to be 4) suggests that the number density of bubbles plays a primary role in enhancing the water-leaving reflectance. The higher value of l

over α, reflects the secondary contribution due to the increasing penetration depth of bubbles as the wind speed increases (Eq. 3.3). It should be kept in mind, however, that Eq. 3.7 is only valid for longer wavelengths and does not dependent on the chlorophyll concentration. It applies only to mean conditions that are prescribed by Eqs. 3.2 and 3.3; it might change for a particular bubble generating event.

3.5 Discussion

3.5.1 Remote sensing reflectance

The formation of an underwater bubble layer by breaking waves (wind speed > 7 m s^{-1}) elevates the spectral reflectance over the entire upper hemisphere. The strong backward scattering efficiency, especially when bubbles are coated with organic film (which happens in seconds), contributes to the enhancement of the background reflectance. Even though bubbles, with a spectrally neutral scattering spectrum [*Zhang et al.*, 1998], enhance the scattering process equally within the entire visible and infrared, the strong absorption by liquid water in the longer wavelengths considerably reduces the amount of light that is reflected out of ocean in these bands (Fig. 3.3).

The calculated background reflectance for calm, oligotrophic seas (Fig. 3.3) compared very well with our TSRB measurements in the Equatorial Pacific Ocean during the past several years (results not shown). There have been, however, very few field experiments designed to measure the background reflectance in high seas. At wind speeds between 10 and 12 m s^{-1}, Moore *et al.* [2000] found the background reflectance at 410 nm in the absence of whitecaps is about 0.02 sr^{-1} in the tropical Pacific Ocean. This value is much higher than the background reflectance estimated under the bubble-free

situation (solid lines of Fig. 3.3-a) and is close to our estimate of ρ_b with wind speed of 20 m s^{-1} for oligotrophic water. The difference might be because Eq. 3.2 underestimates the bubble concentration, given a large scatter in the relationship between wind speed and bubble concentration.

By the first approximation of single scattering, the volume scattering between about 50° and 180° would be responsible for backscattering downwelling irradiance upward [*Gordon*, 1989]. As shown in Fig. 3.1, bubbles also exhibit strong scattering for angles between 60° and 80° due to critical angle scattering at the water-bubble interface. It is interesting to investigate how this critical angle scattering alters the angular distribution of the background reflectance.

This is examined by replacing a bubble layer with a particle layer, with everything identical except that the phase function for particles has a different shape, but with the same backscattering ratios ($\equiv \frac{b_b}{b}$). The particle phase function, shown in Fig. 3.1 as a dotted line, was calculated with the analytic formula proposed by Fournier and Forand [*Fournier and Forand*, 1994]. Obviously, the major difference between the two phase functions is the critical angle scattering exhibited solely by bubbles. The comparisons of the background reflectances at 555 nm normalized by the total background reflectance integrated over the entire spectrum are shown in Figure 3.6 for a solar angle of 30°. Relatively speaking, while a particle layer will produce a more uniform upward light field, the critical angle scattering by an underwater bubble layer will reflect more light out of the ocean at angles larger than 20°.

Assuming single scattering prevails, the incident sunlight at 30° will be reflected out of the ocean by the volume scattering from 60° to 180°, whereas the water-leaving background radiance for the solar angle of 10° is mainly due to the volume scattering between 80° and 180°. Therefore, the gradually increased reflectance over the large angles due to the critical angle scattering is more significant for larger solar incident angles (Fig. 3.2). For small Sun zenith angles (< 10°), the optical effect on the surface reflectance by bubbles is almost the same as for particles of similar integral scattering properties over the backward directions.

3.5.2 Implication for remote sensing

The presence of whitecaps affects the atmospheric correction of an ocean color sensor in two ways [*Gordon and Wang*, 1994a; *Gordon*, 1997]. First, the assumption that the remote sensing radiance is negligible in the NIR is invalid because of added reflectance, ρ_f, due to whitecaps (Eq. 3.4). Second, the contribution by whitecaps to the remote sensing radiance in the visible domain has to be corrected in order to get ρ_b (Eq. 3.4), which was regarded as the "true" background radiance. In this study, we have shown that ρ_b also changes due to the existence of an underwater bubble layer, which coexists with but lasts longer than the whitecaps under strong windy conditions.

The variation of ρ_b for oligotrophic water at 765 nm, corresponding to band 7 of SeaWiFS, is plotted in Figure 3.7-a as a function of wind speeds. Comparing to the digital noise count level for the SeaWiFS band 7 [*Barnes et al.*, 1994], it is clear that the black pixel assumption for the infrared no longer holds as wind speed exceeds 9 m s^{-1}, even considering the underwater bubbles alone. Siegel *et al.*[2000] have suggested that

when chlorophyll concentration is greater than 2 mg m^{-3}, the reflectance in the infrared bands is much higher than those expected for pure seawater, resulting in an overcorrection of atmospheric effects for retrievals of water-leaving reflectance in the shorter wavelengths. Fig. 3.7-a suggests that high winds would also render this assumption invalid even in clear ocean environments with low chlorophyll concentration. Without considering the contribution from whitecaps, the digital count that would be recorded by SeaWiFS band 7 for the oligotrophic water simulated for solar angle of 10° is about 13 (~ 0.03 $\mu W\ cm^{-2}\ nm^{-1}\ sr^{-1}$) when the wind speed reaches 20 $m\ s^{-1}$.

The measured $W\Delta\rho$ (Eq. 3.5) at 765 nm (assumed to be the same as their estimates at 860 nm, Eq. 3.5-b)) [*Moore et al.*, 2000] is also shown in Fig. 3.7-a for comparison. Because of the strong absorption by water, the reflectance due to whitecaps at the sea surface dominates over that due to submerged bubbles in the infrared. The contribution to the total remote sensing reflectance ρ (solid line in Fig. 3.7-a) by bubbles is at most 10%; whitecaps, by virtue of their high reflectance, are a major contributor to the reflectance in the infrared once they are present.

In the visible domain, the situation is reversed however, as demonstrated in Fig. 3.7-b. Even within whitecap patches, about 90% of the total water-leaving reflectance (at 445 nm) is due to the background reflectance, which has been amplified by the submerged bubble layer. In high wind situations, the whitecap correction procedures proposed for the atmospheric correction scheme are still valid in the infrared, because the underwater bubble layer contributes less than 10% of the total reflectance. For the visible wavelengths however, the proposed procedure is inadequate, because of predominance of background bubble reflectance over the whitecap reflectance.

The elevated background reflectances due to submerged bubbles in the visible, if left uncorrected, will affect the geophysical products derived using the color ratio algorithm. For example, the chlorophyll concentrations are normally estimated using the ratio of ρ_b at blue (e.g. 445 nm) to green (e.g., 555 nm) wavelengths [e.g. *O'Reilly et al.*, 1998]. The change of this color ratio (CR) is shown in Figure 3.8 as a function of wind speed. The color ratio is reduced due to bubble injections, and as a result the water appears greener. The color ratio reduction, which increases with the wind speed, will result in an overestimate of the chlorophyll concentration. Finally, the color ratio bias, and consequently the error in chlorophyll concentration, will be more severe in clear waters than in more productive waters.

3.6 Conclusions

As an extension to our previous study [*Zhang et al.*, 1998], we analyzed the influence of the underwater bubble populations on the hyperspectral remote sensing reflectance. While it has been recognized that bubbles are primarily generated by breaking waves, many field observations have suggested that a large number of bubbles could exist when there was no wind [*Medwin*, 1977; *O'Hern et al.*, 1988]. Interestingly, the most abundant bubble population so far reported is under calm sea condition [*O'Hern et al.*, 1988]; the number density was found to be 2×10^7 m^{-3}, which, according our model, would correspond to a bubble layer at wind speed of about 23 m s^{-1}. Even though we have only focused on the wind-generated bubbles, the results of this study could be equally applied to those bubbles found in quiescent seas.

The dependence of the number density (Eq. 3.2) and the penetration depth (Eq. 3.3) of a bubble layer on wind speeds were derived from reported *in situ* measurements in the ocean. The largest uncertainty involved in this parameterization process is the exponent α we adopted for Eq. 3.2; it is the average of the reported values, which in turn were statistically derived from field measurements. The existence of a ubiquitous relationship between wind speed and bubble concentration remains to be demonstrated. The comparison with *in situ* reflectance data in the equatorial Pacific [*Moore et al.*, 2000] suggests that the influence of bubbles might be underestimated. This study is aimed at an analysis of possible influences on reflectances by an underwater bubble layer; errors associated with the predictions of concentrations and penetration depths of bubble populations will only shift the magnitude of our analysis, but the major conclusions should remain valid.

The simulated hyperspectral background reflectance using HydroLight 4.0 indicated that the presence of the underwater bubble layer will produce an elevated but more diffuse upward radiance field. Because of the contribution by multiple scattering between bubbles and phytoplankton, the enhanced background reflectance cannot be related to the wind speed alone in the shorter wavelengths. However, such a relationship could be established in the red and infrared (Eq. 3.6), where the absorption by liquid water is very high such that only photons that are scattered once could escape. The number density of bubbles is found to play a major role in enhancing the water-leaving reflectance.

Whitecaps and underwater bubble layer always coexist under windy conditions [*Thorpe and Humphries*, 1980; *Monahan and Lu*, 1990; *Wu*, 1992]; however the

residence times for submerged bubbles (> 1000 s) is much longer than that of whitecaps (several seconds) as long as the wind speed is high enough (> 7 ms^{-1}) to maintain the continuous generation of bubbles. For the application of ocean color remote sensing, the influences of both whitecaps and the underwater bubble layer have to be considered simultaneously. While in the infrared, the whitecaps account for most of the enhanced remote sensing reflectance (Fig. 3.7-a), the effect of the bubble layer plays a major role in the visible domain. If only the effect by whitecaps is corrected [*Gordon and Wang*, 1994a; *Frouin et al.*, 1996; *Gordon*, 1997], the chlorophyll concentration would be overestimated (Fig. 3.8) due to the color shift, which increases with wind speed and is more drastic for waters with low chlorophyll concentration. While it has been realized that applying ocean color remote sensing in Case 2 waters [*Morel and Prieur*, 1977] could be problematic [e.g., *Sathyendranath*, 2000], the presence of bubbles impose a more serious problem in Case 1 waters, where both atmospheric and bio-optical algorithms are assumed to be largely well constrained.

Investigators	U_{10} (ms^{-1})	$\bar{r}$ (μm)	$\bar{s}$ (m^2)	$\overline{\sigma_b}$ (m^2)
Kolovayev, 1976	11-13	79	2.4×10^{-8}	4.8×10^{-8}
Johnson & Cooke, 1979	11-13	52	1.1×10^{-8}	2.2×10^{-8}
Crawford & Farmer, 1987	11	52	1.1×10^{-8}	2.2×10^{-8}
Walsh & Mulhearn, 1987	14	110	4.6×10^{-8}	9.2×10^{-8}
Su et al., 1988	10	27	3.1×10^{-9}	6.2×10^{-9}
Medwin & Breitz, 1989	12-15	56	1.4×10^{-8}	2.8×10^{-8}
Mean values		53.71	1.8×10^{-8}	3.6×10^{-8}

Table 3.1 Field experiments and derived mean radius and optical properties for oceanic bubble populations.

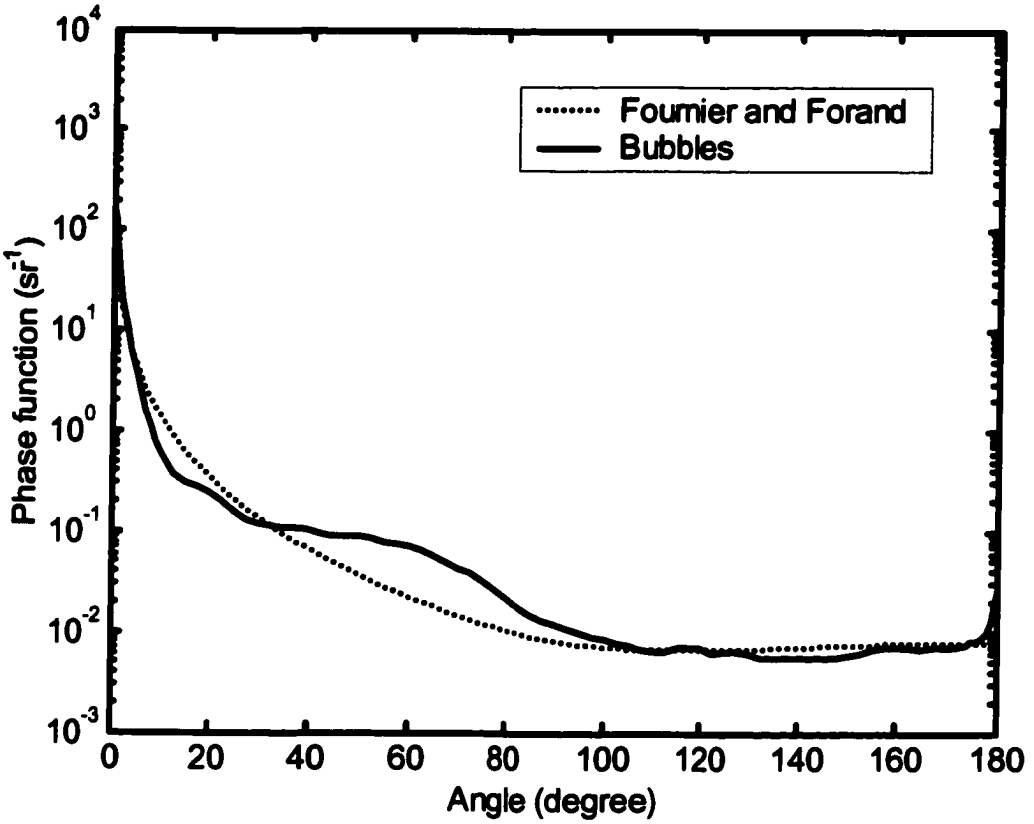

Figure 3.1. The phase function calculated for bubble populations that have been observed in the ocean. The dotted line is the phase function calculated using the analytic formula by Fournier and Forand [*Fournier and Forand*, 1994] with the same backscattering ratio as the bubbles.

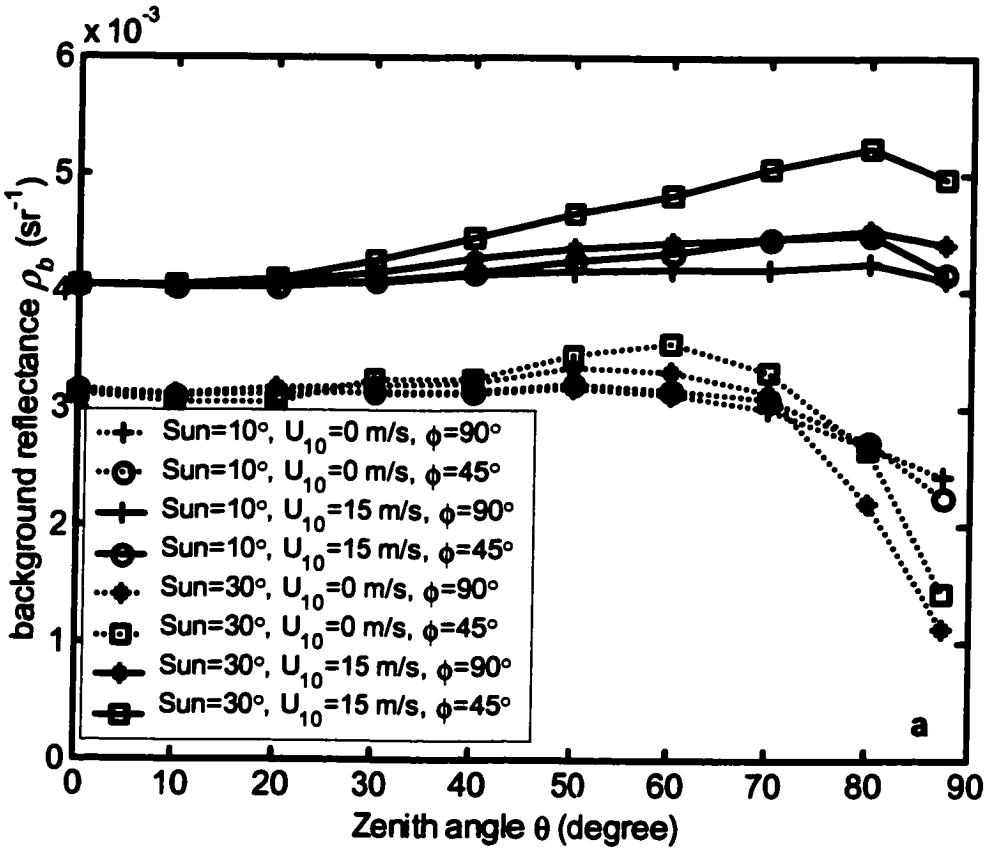

Figure 3.2-a The angular distribution of the background reflectance ρ_b at 555 nm as a function of exiting zenith angle for the mesotrophic water under various ambient geometric and wind conditions.

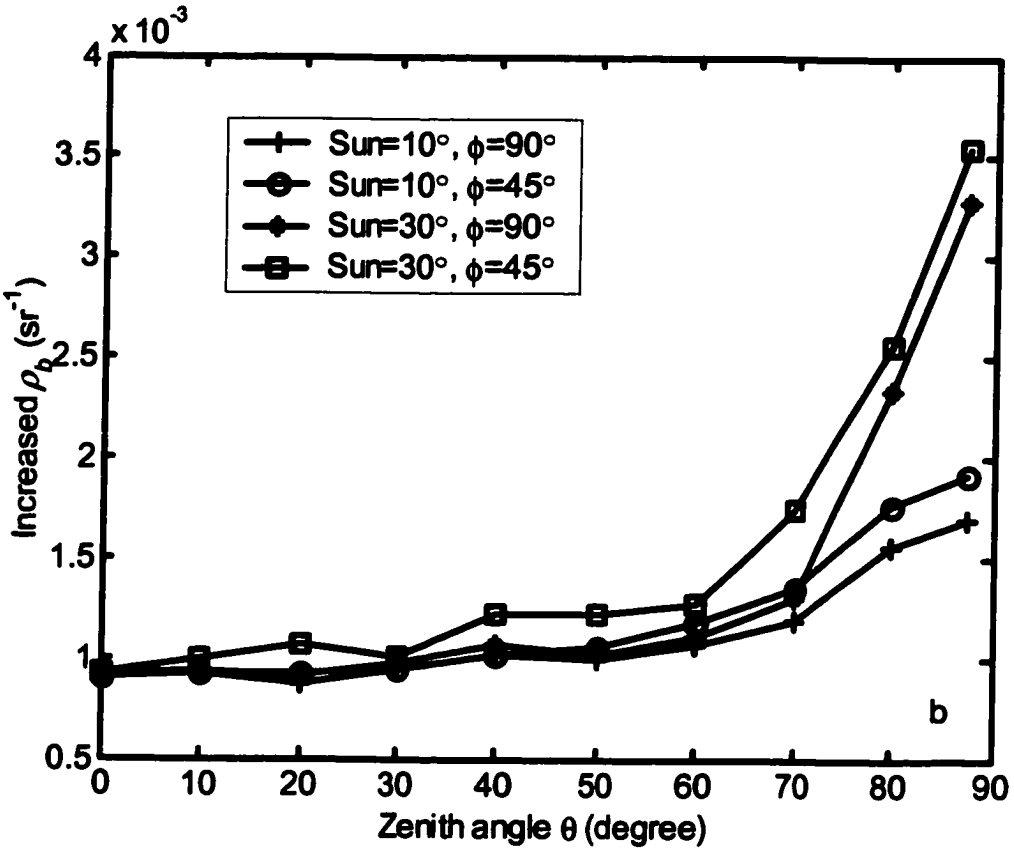

Figure 3.2-b The increased background reflectance ρ_b at 555 nm as a function of exiting zenith angle simulated for the mesotrophic water for 4 different configurations of incident solar radiance.

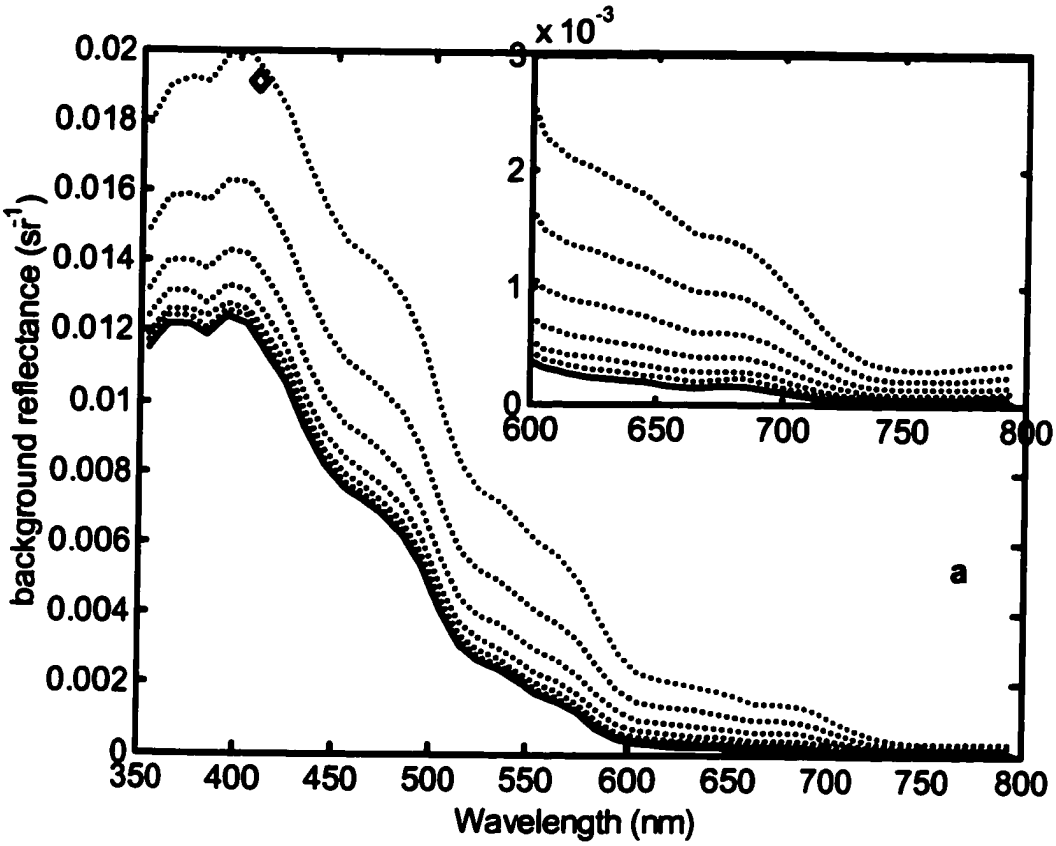

Figure 3.3-a The background reflectance ρ_b with zero zenith angle as a function of wavelength from 350 nm to 800 nm for various wind speeds for oligotrophic waters. The solar angle is 10°. The inset in the figure is the enlarged plot for the red and infrared wavelengths. The background reflectance at 410 nm measured by Moore *et al.* in equatorial Pacific is shown as a diamond. Solid line is for no wind, and dotted lines, from bottom to top, are for wind speeds of 10, 12, 14, 16, 18, and 20 m s^{-1}, respectively.

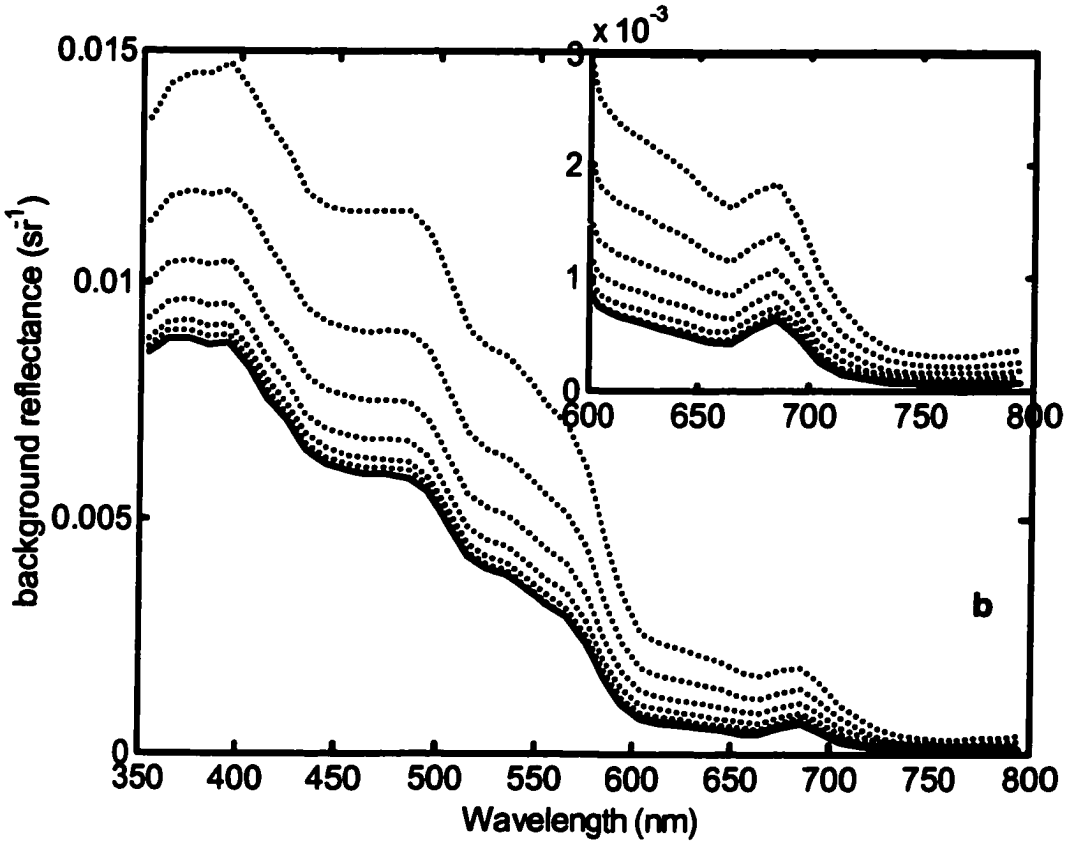

Figure 3.3-b The same as Fig. 3.3-a except for mesotrophic waters.

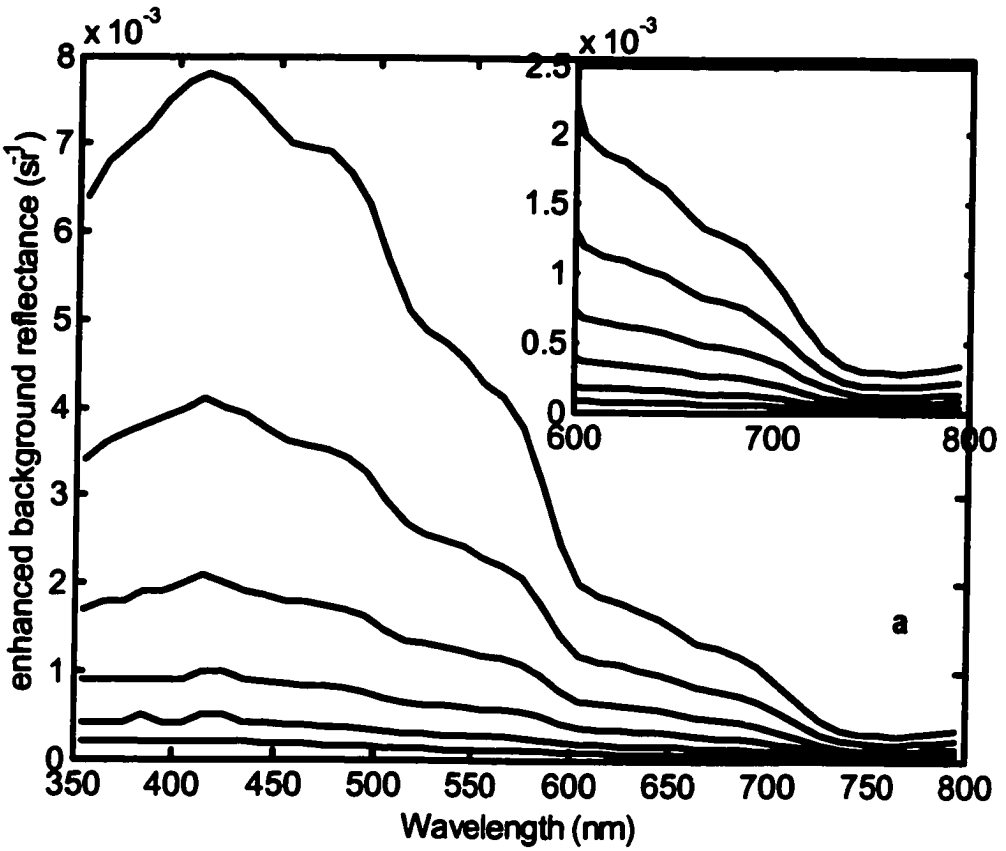

Figure 3.4-a The enhanced background reflectance with zero zenith angle due to the presence of bubbles as a function of wavelength from 350 nm to 800 nm for various wind speeds for oligotrophic waters. The solar angle is 10°. The inset in the figure is the enlarged plot for the red and infrared wavelengths. Solid lines from bottom to top are for wind speeds of 10, 12, 14, 16, 18, and 20 m s^{-1}, respectively.

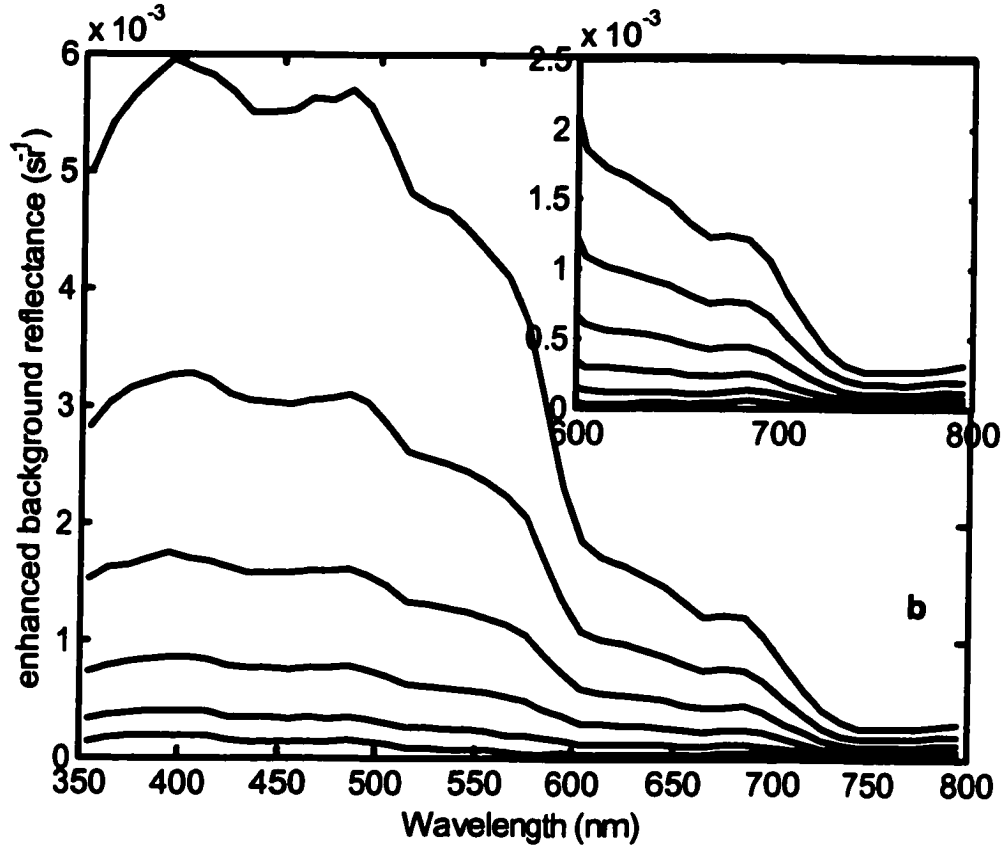

Figure 3.4-b The same as Fig. 3.4-a except for mesotrophic waters.

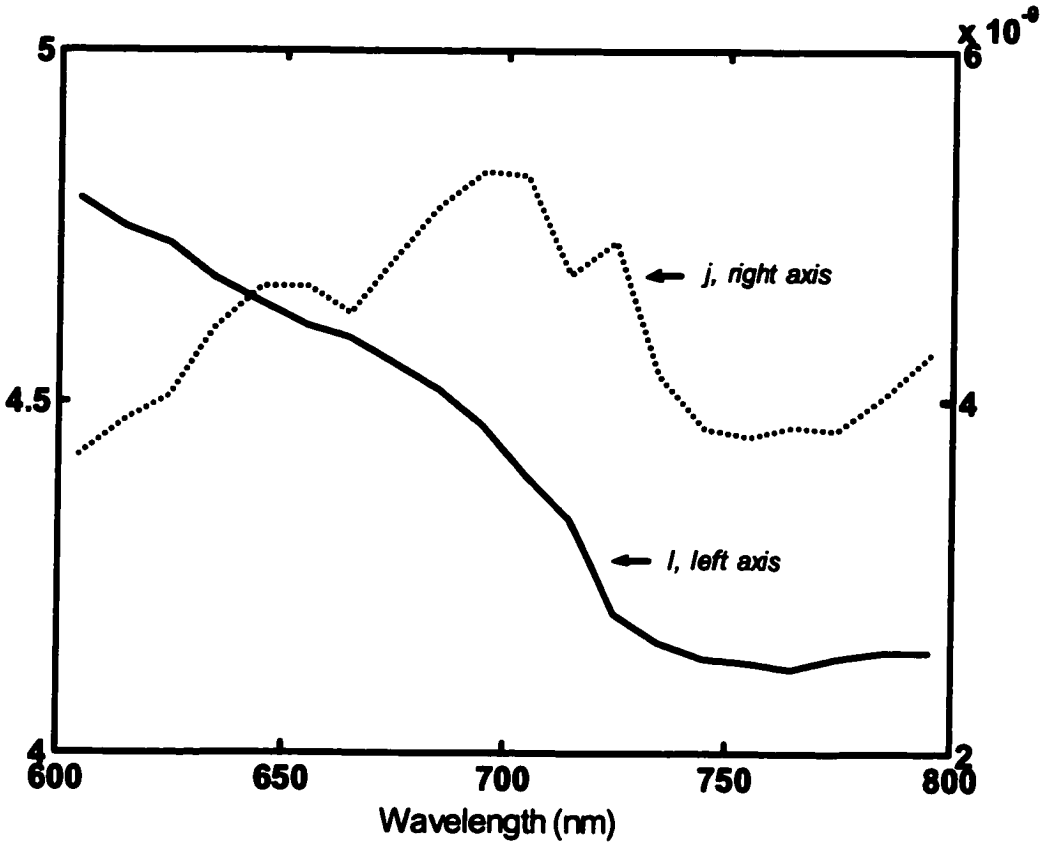

Figure 3.5. The exponent *l* and the coefficient *j* of Eq. 3.7, as statistically regressed from data shown in Fig. 3.4, are plotted as a function of wavelength from 600 nm to 800 nm. The *l* is scaled to the left y-axis and the *j* to the right y-axis.

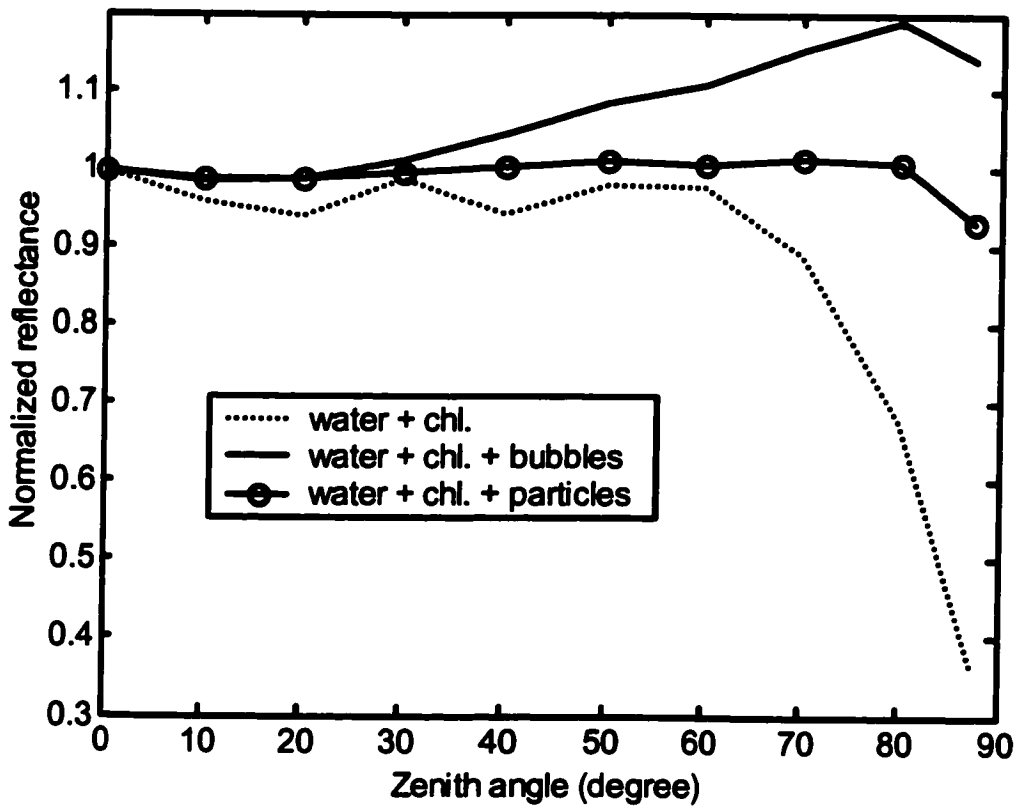

Figure 3.6. The comparison of the angular distribution of the background reflectances ($\varphi = 45°$) calculated for oligotrophic waters containing phytoplankton alone (dotted lines), inclusion of an underwater bubble layer (solid line), and inclusion of a particle layer (solid line with circles). The solar angle is 30°. The vertical distribution profile, the total scattering coefficient and the backscattering ratio are all the same between the bubbles and the particles. The only difference is that bubbles display critical angle scattering while the particles do not.

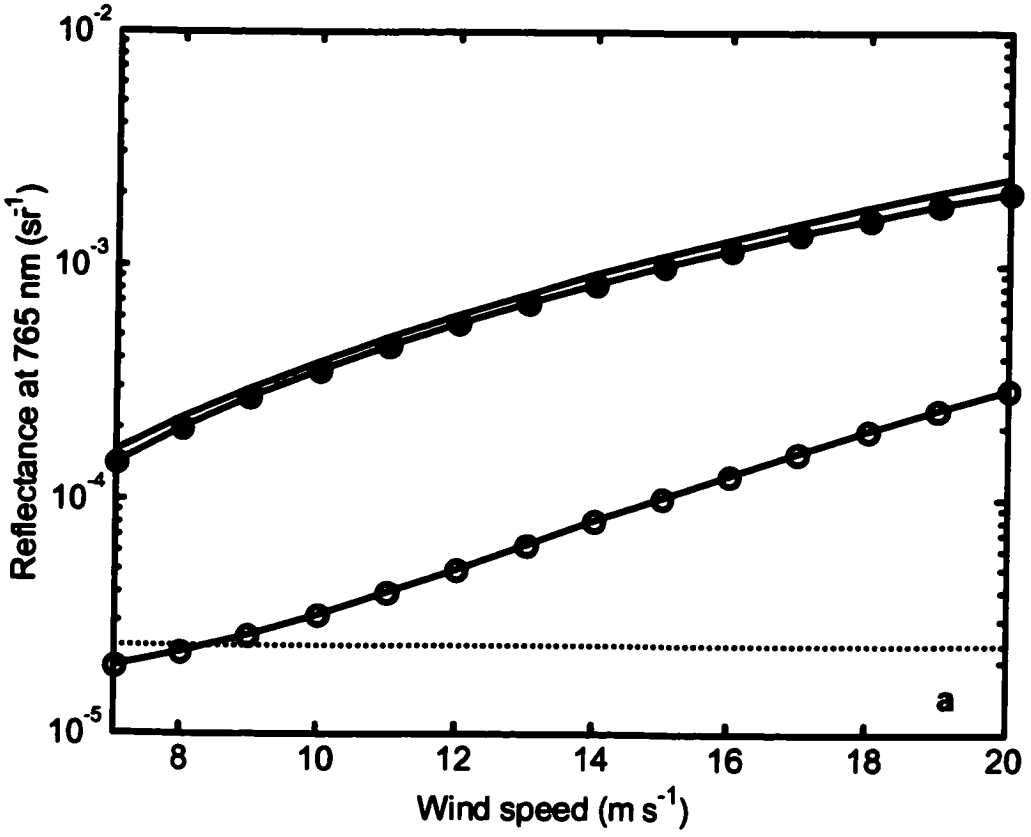

Figure 3.7-a The remote sensing reflectance (solid line) simulated for one remote sensing pixel for oligotrophic waters at 765 nm as a function of wind speed. The remote sensing reflectance is partitioned into (Eq. 3.4) background reflectance for whitecap-free waters, ρ_b, (line with open circles), and augmented reflectance due to whitecaps, $W\Delta\rho$, (line with closed circles). The reflectance corresponding to 1 digital count for SeaWiFS band 5 is plotted as dotted lines.

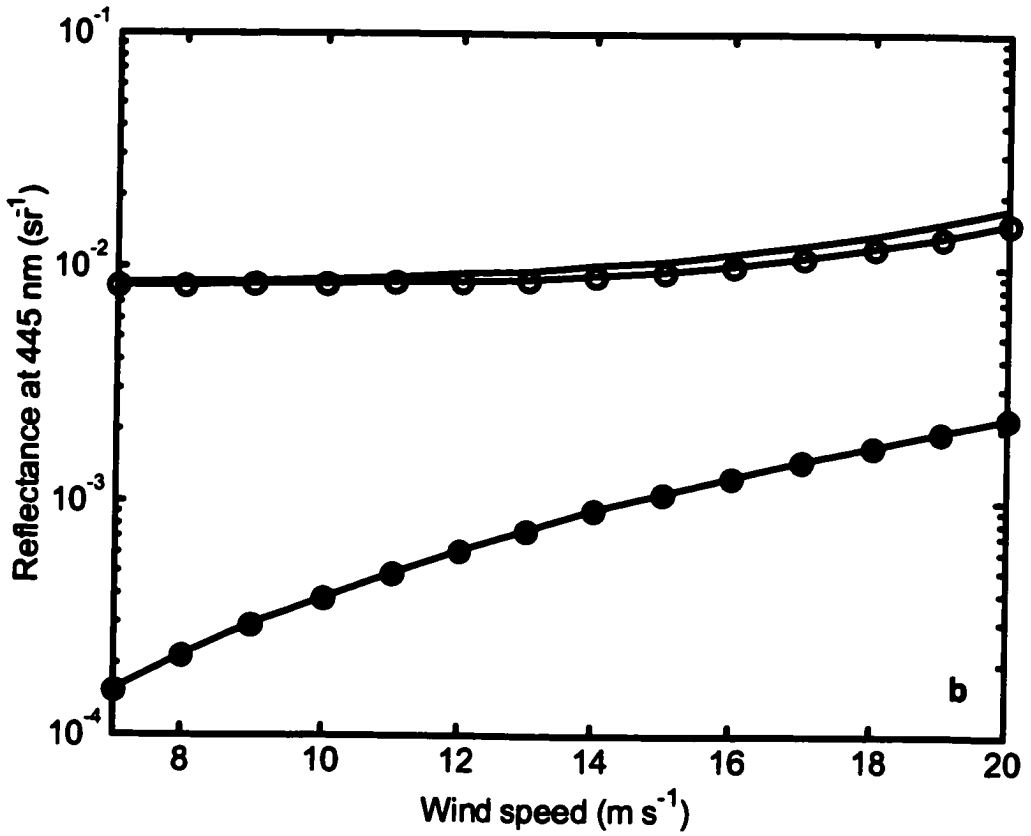

Figure 3.7-b The same as Fig. 3.7-a except for 445 nm. The remote sensing reflectance is partitioned into (Eq. 3.4) background reflectance for whitecap-free waters, ρ_b, (line with open circles), and augmented reflectance due to whitecaps, $W\Delta\rho$, (line with closed circles).

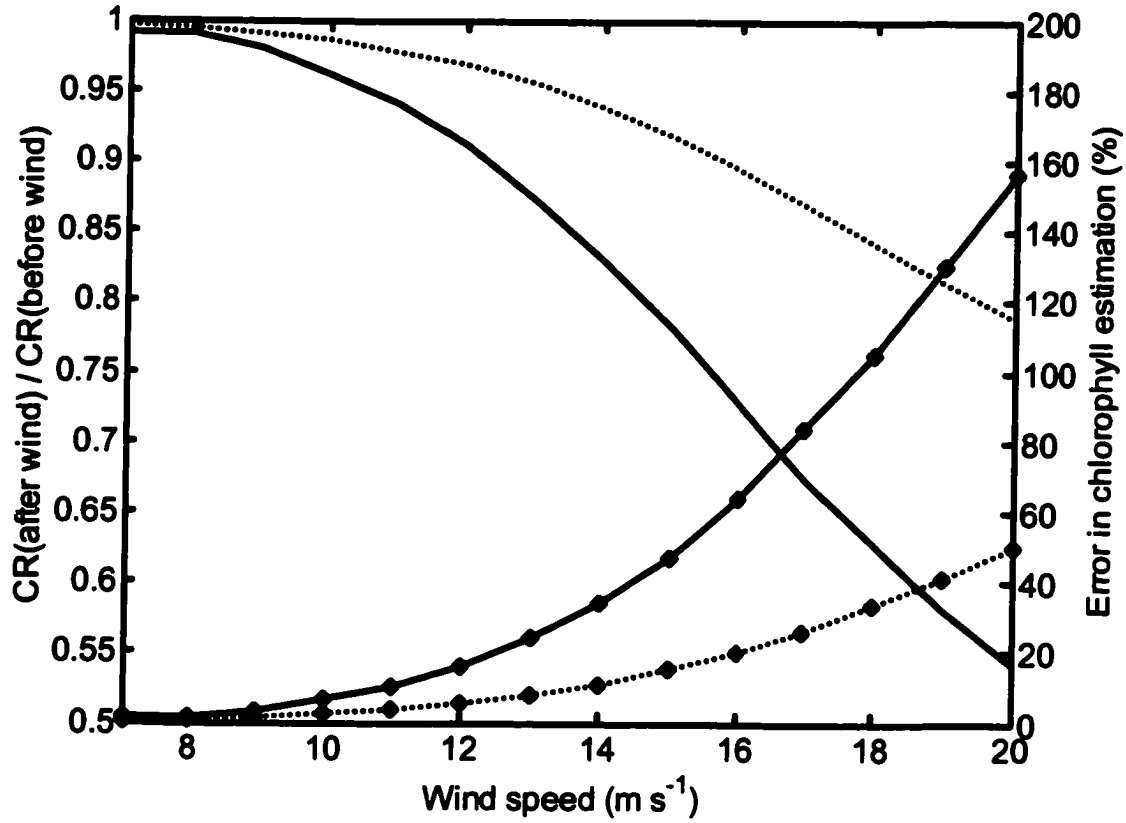

Figure 3.8. The magnitude of the Color Ratio (CR) after wind is compared to CR before wind as a function of wind speed for both oligotrophic (solid line) and mesotrophic (dotted lines) waters. The Color Ratio is defined as the ratio of the reflectance at 445 nm to that at 555 nm. The corresponding errors in chlorophyll estimations (lines with diamonds) are also shown.

Chapter 4 Optical Influence of Ship Wakes

4.1 Introduction

Waves and turbulence generated by a moving vessel result in ship wakes, which appear as a streak of foamy, turbulent water followed by a region of visually smooth water characterized by the absence of small-scale surface roughness. The hydrodynamics of ship wakes, though not fully understood, have been extensively studied [e.g. *Reed et al.*, 1990; *Debnath*, 1994]. For example, Kelvin wakes are formed radiating away from the vessel [*Reed et al.*, 1990], and in the presence of a shallow pycnocline, internal waves are also created [*Lyden et al.*, 1988].

With respect to surface manifestations that could be remotely observed, ship wakes have been found to display a radiant intensity contrast in the thermal infrared [*McGlynn et al.*, 1990]. However, they are most effective in modifying the Bragg scale waves, which enable them to be easily detected by microwave SAR observations [*Lyden et al.*, 1988; *Shedmin*, 1990; *Rey et al.*, 1993; *Shemer et al.*, 1996; *Stapleton*, 1997; *Hennings et al.*, 1999]. Also created below the surface are copious quantities of bubbles, whose acoustic effects have been of great interest for a long time [*Tate and Spitzer*, 1946; *Trevorrow et al.*, 1994; *Dumbrell*, 1997]. Being effectively adsorptive to other particles and organic matter, the bubbles thus produced contribute to the accumulations of surfactant material that have been observed in the centerline wake [*Peltzer et al.*, 1992]. Besides airborne photographs of ship wakes, there have been, however, very few studies on their spectral variability in the visible and near infrared.

Based on theoretical calculations, Zhang *et al.* [1998] concluded that the color change of ship wakes, which appear brighter and greener than the surrounding waters in the open ocean, are due to the presence of bubbles injected by ship wakes. Recently, we have carried out direct hyperspectral measurements within ship wakes in two different water regimes, one in the open Equatorial Pacific Ocean and the other off the coast of New Jersey. Moreover, the bubble size distributions were also measured by both acoustic and photographic methods during the LEO-15 (New Jersey) experiment. Here, we will present and discuss theory and measurements of the optical properties of ship wakes in these areas and analyze their spectral variations in detail.

4.2 Background and theoretical bases

4.2.1 Ship-generated bubbles

Breaking of bow waves and stern waves, both of which belong to the Kelvin wake system, produce bubbles [*Peltzer et al.*, 1992]. Bubbles are also generated along the ship's hull as a result of air entrainment due to the frictional drag forces at the surface of the hull [*Tate and Spitzer*, 1946]. It has been postulated that the most copious source of bubbles in wakes, however, is propeller cavitation at high speed [*Tate and Spitzer*, 1946], a hypothesis that to date has not been confirmed by field observations [*Trevorrow et al.*, 1994].

Unlike the Kelvin wake system, which radiates at a half angle of 19°28' from about one ship length forward of the bow [*Debnath*, 1994], the newly generated bubbles are relatively confined within the centerline wake due to the horizontal converging wake flow behind the ship [*Reed et al.*, 1990; *Peltzer et al.*, 1992; *Debnath*, 1994]. Because of

the strong turbulence created by the motion of the ship's hull, and the action of its propellers, bubbles will display a roughly homogeneous vertical distribution within the first several minutes [*Trevorrow et al.*, 1994] and can reach down to several meters below the depth of the ship's bottom [*Ezerskii et al.*, 1989].

As the local turbulence diminishes as the ship moves away, the bubble clouds become wider (the maximum width/beam ratio observed is 5 to 7) and shallower as a result of buoyant rising and dissolution [*Tate and Spitzer*, 1946; *Trevorrow et al.*, 1994], the latter of which has been identified as a primary mechanism for bubble dissipation [*Ezerskii et al.*, 1989; *Trevorrow et al.*, 1994]. When bubbles rise, they scavenge surfactant material [*Johnson and Wangersky*, 1987], which accumulates quickly at the sea surface after these bubbles break [*Johnson and Cooke*, 1980]. The organic film thus formed in the ship wake will damp the capillary wave motion and produce a clearly defined slick structure [*Peltzer et al.*, 1992]. While the surface-active film wakes have been observed to persist for tens of kilometers downstream of a surface ship [*Lyden et al.*, 1988; *Peltzer et al.*, 1992], the wake bubbles have been observed to last as strong acoustic scatterers for approximately 7.5 minutes (about 2 km astern for a ship speed of 10 kn) with a maximum width of 60 m [*Trevorrow et al.*, 1994].

The gas void fraction occupied by bubbles in ship wakes has been found to vary with ship size, and propeller size and rotation speed. Based on the acoustic measurement of wake bubbles by a destroyer at 15 knots [*Tate and Spitzer*, 1946], the estimated concentration of bubbles between 1000 μm and 80 μm is about 6×10^{6} m^{-3}. Taking the smaller bubbles into account, the concentration will be higher. Under the assumption that bubbles are coated with 0.1 μm protein organic film [*Zhang et al.*, 1998], the estimated

total optical scattering and total backscattering coefficients for this bubble population is 0.32 m^{-1} and 0.013 m^{-1}, respectively.

4.2.2 Spectral effects of bubbles on the reflectance

To a first approximation, the color of the ocean, i.e., the spectral variation of the diffuse reflectance $R(\lambda)$ ($=\frac{E_u(0^-,\lambda)}{E_d(0^-,\lambda)}$, where $E_u(0^-,\lambda)$ is the upwelling irradiance, and $E_d(0^-,\lambda)$ is the downwelling irradiance, both defined as being just below the water surface) is proportional to the ratio of the total backscattering coefficient $b_b(\lambda)$ to the total absorption coefficient $a(\lambda)$ [*Gordon et al.*, 1975; *Morel and Prieur*, 1977; *Gordon and Morel*, 1983],

$$R(\lambda) = f\frac{b_b(\lambda)}{a(\lambda)}, \qquad \text{4.1-a}$$

where the parameter f depends on the solar zenith angle, the shape of the underwater volume scattering function, and to a lesser degree, on the single scattering albedo [*Morel and Gentili*, 1991].

For an above-water observation such as from satellite, the spectral water-leaving reflectance, or the remote sensing reflectance $R_{rs}(\lambda)$ ($=\frac{L_u(\lambda)}{E_d(0^+,\lambda)}$, where L_u is the water leaving radiance at zenith, and $E_d(0^+,\lambda)$ is the downwelling irradiance just above the water), is often used to describe the color variation, and

$$R_{rs}(\lambda) = G\frac{f}{Q}\frac{b_b(\lambda)}{a(\lambda)}, \qquad \text{4.1-b}$$

where Q is the ratio of upwelling irradiance to the vertical upwelling radiance (both are defined being just below the surface), and parameter G accounts for cross-interface effects of light entering into and coming out of the ocean. The parameter G does not change with wavelength (to the extent that the refractive index of water is a constant over the visible). Like f, Q also depends on geometrical configuration of the observation and the shape of the volume scattering function in the upper ocean [*Morel and Gentili*, 1993]. Both f and Q slightly change with wavelength; however, the ratio of f to Q is less variant and almost a constant between 440 nm and 560 nm [*Morel and Gentili*, 1993]. Therefore, most of the variability in the color of the ocean observed from above is due to the spectral changes in the scattering and absorption processes in the ocean interior.

Since the absorption by bubbles is negligible [*Zhang et al.*, 1998], the injection of wake bubbles mainly influences the scattering. And as a result, the reflectance is enhanced to,

$$R_{bub}(\lambda) = f_{bub}\frac{b_b(\lambda)+b_{b,bub}}{a(\lambda)}, \qquad 4.2\text{-a}$$

or

$$R_{rs,bub}(\lambda) = G\frac{f_{bub}}{Q_{bub}}\frac{b_b(\lambda)+b_{b,bub}}{a(\lambda)}, \qquad 4.2\text{-b}$$

where $b_{b,bub}$ is the backscattering coefficient for bubbles, which is spectrally flat, and the change of parameters f to f_{bub} and Q to Q_{bub} result from the changes in the volume scattering function due to the introduction of bubbles. The backscattering due to bubbles, $b_{b,bub}$ in Eq. 4.2, accounts for the brighter appearance of bubble wakes at the sea surface.

Because of the strong absorption by water molecules in the red wavelengths, most of the variation in the color of the ocean is restricted to the blue-green part of the spectrum. An approximate estimate of the color can be gauged by forming a reflectance ratio ("blue-green ratio") between the blue (440 nm) and the green (550 nm), defined as

$$\rho_{440-550} = \frac{R(440)}{R(550)} = \frac{R_{rs}(440)}{R_{rs}(550)}$$
$$= \frac{b_b(440)}{b_b(550)} \frac{a(550)}{a(440)} \qquad \textit{before bubble injection,.} \qquad 4.3$$
$$= \frac{b_b(440) + b_{b,bub}}{b_b(550) + b_{b,bub}} \frac{a(550)}{a(440)} \qquad \textit{after bubble injection}$$

It is clear from Eq. 4.3 that the blue-green ratio (or the color of the ocean) changes after bubble injection even though the scattering by bubbles is spectrally nonselective. Water would appear blue if the blue green ratio is greater than one, and green if the ratio less than one. The comparison of the blue-green ratio before and after the bubble injection reflects the variation of the color due to bubbles,

$$\Re = \frac{\rho_{440-550}(after)}{\rho_{440-550}(before)} = \frac{1 + \dfrac{b_{b,bub}}{b_b(440)}}{1 + \dfrac{b_{b,bub}}{b_b(550)}}. \qquad 4.4$$

If the ratio $\Re < 1$, the presence of bubbles would shift the modal spectral reflectance to longer wavelengths, and result in greener water as seen from above. This would normally be the case for clear ocean water, where the backscattering at 440 nm is less than that at 550 nm [*Gordon et al.*, 1988; *Morel*, 1988]. However, in other cases, where $b_b(550) < b_b(440)$, $\Re$ will be greater than 1 and the bubble injection would shift the color toward the blue.

4.3 Methodology

To evaluate these predictions, ship wake experiments were conducted in two vastly different water regimes. One was in the Western Equatorial Pacific Ocean onboard the research vessel, Mirai (JAMSTEC), from December 1998 to January 1999. The concentration of *Chl-a* was < 0.1 mg m^{-3} in the region during that time and the background attenuation coefficient, c ($\equiv a + b$) at 490 nm was ~0.03 m^{-1}. The other experiment took place in coastal waters off New Jersey [*LEO-15*, 2001]. Due to strong runoff from wetlands, the water here is very turbid (c (490) > 2 m^{-1}). We will refer to the experiment in the Equatorial Pacific as Clear Wake and that at the LEO-15 as Turbid Wake.

Only one instrument, the hyperspectral TSRB (Satlantic Inc.) was used in the Clear Wake experiment. The TSRB measures the upwelling hyperspectral radiance at a depth of 0.6 m, and downwelling irradiance just above the surface, from 400 nm to 800 nm with a spectral resolution of 3.3 nm. The ratio of the upwelling radiance to the downwelling irradiance, both of which propagated to just above the sea surface, forms the remote sensing reflectance ($R_{rs}(\lambda)$). The measurements were first taken under calm seas behind the ship, which had stopped for a long period. The propeller was then run briefly (5 s) at high speed to generate cavitation bubbles. The TSRB was then situated in the resulting bubble cloud, and allowed to stream with the cloud as it advected away from the ship. Each measurement series, for both background control and bubble injection, was taken for 3 minutes (~90 records), and the result used in this study is the median record. The median estimate reduces the potential contaminations from foam and other high

frequency environmental variance. A photograph of the wakes generated in the Clear Wake experiment is shown in Figure 4.1.

In the Turbid Wake experiment at the LEO-15 site, ship wakes were generated by a small motorboat, which was driven across the experiment location. Measurements were taken from an instrumented catamaran, which was towed over the wakes. Measurements were made of upwelling hyperspectral radiance at a depth of 0.6 m, and downwelling irradiance above the surface. An underwater bubble camera provided imagery of the bubble population, and a high-frequency acoustic backscattering instrument measured the sound reflectance by bubbles at various distances. The configuration of the optical sensors is the same as in the TSRB, except that they were attached to the catamaran at the LEO-15 site, and will be referred to as TSRB. At each wake crossover, both the TSRB and the acoustic backscatter were turned on for 5 minutes, and the camera took pictures every 45 seconds.

The camera and the acoustic backscatter device were designed to work in a complementary mode to provide the measurements of number density of bubbles over a large size range. The camera system is an improved version of a previous instrument, and is designed to measure bubble populations [*Johnson and Cooke*, 1979] by using a high-resolution digital camera. The pixel size of the camera is 19 μm and therefore the minimum size of a bubble that could be resolved by the camera is about 40 μm (at least 2 pixels are needed to identify a bubble). The acoustic backscatter device operates at frequencies from 1 MHz to 5 MHz, which theoretically provide estimates of bubbles of size between submicron and less than 10 μm [e.g. *Medwin and Clay*, 1998]. Due to the strong contribution of large bubbles to the high-frequency acoustic signals [*Commander*

and Moritz, 1989], the estimates of the bubble spectra at larger size by the photographic method have to be used to correct for the off-resonant acoustic contributions by these large bubbles.

4.4 Results

4.4.1 Equatorial Pacific Ocean

The reflectances measured at 3 stations for the Clear Wake experiment are shown in Figure 4.2-a. Clearly, the reflectances inside the wake are elevated over the whole visible spectrum, in agreement with the prediction of Eq. 4.2. The increased reflectance, albeit slightly, was also observed in the near infrared. While the reflectances for the wake-free waters are almost the same, they varied inside the wakes for different stations, probably due to variations in the concentration of bubbles generated by the wake.

An example of the spectral change due to the bubbles can be examined in Figure 4.2-b, where the reflectances measured at 170.2° W on the equator are normalized to the integrated reflectance over the whole spectrum. Because of the non-discriminative and strong backscattering by bubbles, relatively more light in the longer wavelengths was reflected out of the ocean before water molecules could otherwise absorb them. Consequently, these clear waters, which are dominated by blue reflectance in the background state, appeared greener than before. The blue-green ratio, $\rho_{440\text{-}550}$, decreased after bubble injection (Fig. 4.2-a) for all stations. The color shift ratio, $\mathcal{R}$'s, were 0.86, 0.74 and 0.57 for the stations 163.6° E, 176.3° W and 170.2° W, respectively.

4.4.2 LEO-15

The reflectances measured outside and inside wakes at LEO-15 during one wake crossing on July 28, 2000 are shown in Figure 4.3-a. The magnitude of the background reflectances, in general, is smaller than those measured during Clear Wake experiment, due to the presence of high concentrations of absorbing materials, like phytoplankton and silts. The water-leaving spectral radiance was dominated by green-yellow signals (550 – 600 nm) and a shoulder between 600 nm and 650 nm is likely related to brownish particulates suspended in the coastal water. The chlorophyll fluorescence peak at about 680 nm is clearly visible. Despite the difference in the spectral signature between the LEO-15 site and Pacific Ocean, the general effect on the reflectance from the ship wakes is the same, i.e., the reflectances are elevated over the whole spectrum.

However, contrary to the observation of a decrease in the blue-green ratio in the Clear Wake experiment, $\rho_{440\text{-}550}$ increased slightly from 0.338 outside of the wakes to 0.380 inside the wakes. Relatively speaking, there is a slight increase of reflectance in the blue part of the reflectance spectrum (Figure 4.3-b). The spectral variations in the turbid wakes is not as large as that found in the clear wakes. The color shift $\mathcal{R}$ is about 1.12.

Three size spectra of ship wake bubbles with a time lag of 90 seconds, derived from the underwater camera measurements during the same crossing, are shown in Figure 4.4. The size range of bubbles that have been identified is between 40 μm and 400 μm. In general, the total number of bubbles within this size range decays with time, from about 1×10^{6} m^{-3} initially to 3×10^{5} m^{-3} after 3 minutes. The inferred total backscattering

coefficients due to these ship wake bubbles are 0.0027 m^{-1}, 0.0014 m^{-1}, and 0.0007 m^{-1}, respectively.

4.5 Discussion

The observations of reflectances in both clear open ocean and turbid coastal waters demonstrate that the presence of bubbles elevates the reflectance across the entire visible and near infrared portion of the spectrum. The general increase in the magnitude of the reflectance is due to the additional backscattering by bubbles, which is almost spectrally flat on theoretical grounds [*Zhang et al.*, 1998]. These colorless bubbles, however, alter the color of the water (Figs. 4.2-b and 4.3-b) by relatively increasing the scattering in the presence of absorbing material. The Clear Wake experiment indicates a color change towards the green, while the Turbid Wake experiment shows no or very slight blue shift in the color. To a first approximation, the effect of this color change depends on the spectral shape of the backscattering coefficient of waters prior to bubble injection (Eq. 4.4). In fact, the measurements of the variation of the reflectance caused by the injection of bubbles provides a unique way to study the backscattering coefficient of natural waters, which can only be measured correctly by a volume scattering meter.

From Eqs. 4.1 and 4.2, we have

$$\frac{b_b(\lambda)}{b_{b,bub}} \approx \frac{R_{rs}(\lambda, before)}{R_{rs}(\lambda, after) - R_{rs}(\lambda, before)}. \qquad 4.5$$

Because the backscattering by bubbles, $b_{b,bub}$, is spectrally flat, any spectral variation in the total backscattering coefficient, $b_b(\lambda)$, is reflected in the R.H.S. of Eq. 4.5, which can

be easily formulated from Figs. 4.2-a and 4.3-a. Furthermore, if either the total backscattering coefficient $b_b(\lambda)$ or the backscattering coefficient for bubbles $b_{b,bub}$ is known, we can estimate the other. The accuracy of the prediction by Eq. 4.5, however, depends on the precision of the measurements of the reflectance in the presence of bubbles. Before we explore the applications of Eq. 4.5, we evaluate the performance of the algorithm used to propagate radiance at a given depth near the surface to and through the surface to derive the water-leaving radiance (reflectance) at nadir.

4.5.1 Errors in the TSRB algorithm

Upwelling radiance was measured at a depth of about 0.6 meter below the surface and the downwelling irradiance above water. Because of the strong attenuation by water and other substances, the upwelling radiance has to be propagated to the sea surface and across the air-water interface to form the remote sensing reflectance. The propagation method involves the uses of two empirical models. First it uses the measured radiance ratio (under water) between 443 nm and 550 nm to estimate the upwelling radiance attenuation coefficient at 490 nm by means of an empirical algorithm [*Austin and Petzold*, 1981]. Then a spectral model is used to link the diffuse attenuation coefficients and the pigment concentration [*Morel*, 1988]. This model first inversely derives the pigment concentration from the estimated attenuation at 490 nm, and then calculates the attenuation coefficients at other wavelengths with the estimated pigment concentration. Note however, the model is only valid for the visible domain (400 nm – 700 nm). For wavelengths above 700 nm, only the attenuation due to water molecules is corrected for.

We used a numerical radiative transfer model (HydroLight [*Mobley*, 1994]) to test the algorithm performance in bubbly waters. The chlorophyll concentration was assumed to be constant to a depth of 40 m and varied over the range from 0.1 mg m^{-3} to 10 mg m^{-3}. The concentration of bubbles is assumed to decay exponentially with depth [*Thorpe*, 1986a] and was set to be 2×10^{7} m^{-3} at the surface. The solar zenith angle is 10° for all the cases. The upwelling radiance spectra calculated at 0.6 m below the surface were taken to be the TSRB measurements, and were propagated to just below the surface by the TSRB algorithm to compare with the HydroLight computations.

The results, shown in Figure 4.5, suggest that the TSRB algorithm works well for Case 1 waters [*Morel and Prieur*, 1977], except for the spectral band between 650 and 700 nm, where the interference by phytoplankton fluorescence causes overestimates of about 15% in the upwelling radiance just below the surface. On the other hand, the presence of bubbles causes an underestimate of the upwelling radiance because the band ratio algorithm is not very sensitive to scattering by bubbles, which, however, increases the attenuation by increasing backscattering almost equally over the entire spectrum. The error is larger for blue waters (low chlorophyll concentration) than for green water (high chlorophyll concentration). Because of the short propagation distance (0.6 m), the errors are generally less than 20% and less than 10% for blue and green wavelengths, respectively.

4.5.2 The spectral backscattering coefficients

Figure 4.6 shows the spectral variations of $\frac{b_b(\lambda)}{b_{b,bub}}$ (or almost equivalently $b_b(\lambda)$, since $b_{b,bub}(\lambda)$ is spectrally invariant) normalized at 400 nm for both Clear Wake and

Turbid Wake experiments. The spectral shapes derived for the two different types of waters resemble their respective reflectance spectra. The closeness among the three estimates (dotted lines) from different locations of the Equatorial Pacific suggests that the backscattering processes in the open ocean are quite similar in terms of the spectral variation. They agree well, especially for the spectral range from 400 nm to 550 nm, with the modeled backscattering coefficient (also normalized at 400 nm) [Eqs. 11, 12, and 13 of Morel, *Morel and Maritorena*, 2001] for waters with chlorophyll-a concentration of 0.1 mg m^{-3}, an estimate provided by remote observation of SeaWiFS for the region during January of 1999. The difference in the longer wavelengths could be due in part, to the errors introduced by the algorithm to propagate sub-surface radiance to the surface.

At the LEO-15 site, since we have the independent estimate of $b_{b,bub}$, inferred from bubble camera measurements and Mie theory [*Zhang et al.*, 1998], we can compute $b_b(\lambda)$, which is shown in Figure 4.7; the backscattering coefficient for wake bubbles is taken as 0.0027 m^{-1} (calculated for the solid curve of Fig. 4.4). The backscattering by particles, obtained by subtraction of the contribution by water from $b_b(\lambda)$, is also shown in Fig. 4.7. Backscattering by particles increases from about 0.002 m^{-1} at 400 nm to 0.012 m^{-1} at 550 nm, and then drops off slowly to 0.01 m^{-1} at 700 nm. Suspended sand or sediments might be responsible for this spectral backscattering. Because of the increased scattering from blue to green, the wake water appears bluer, at least in theory (Eq. 4.4) but not necessarily visually, because the colour shift is not very significant ($\Re$ = 1.12, Fig. 4.3).

4.5.3 Estimation of the backscattering coefficients for bubbles

As shown in Fig. 4.6, the backscattering for bubble-free waters in the Clear Wake experiment can be well represented by existing models [*Morel and Maritorena*, 2001] for a chlorophyll concentration of 0.1 mg m^{-3}. If we use this model prediction for $b_b(\lambda)$ in Eq. 4.5, we can estimate $b_{b,bub}$ for the three Equatorial Pacific stations. The obtained backscattering coefficients for bubbles are expected to be constant over the whole spectrum, at least for the blue and green wavelengths by virtue of relatively better performance of the propagation algorithm in this spectral range (Fig. 4.5). The backscattering coefficients of bubbles from 400 nm and 550 nm, as shown in Figure 4.8, do not change very much. The mean bubble backscattering coefficient is 0.0004 m^{-1}, 0.001 m^{-1} and 0.004 m^{-1}, for stations 163.6° E, 176.3° W, and 170.2° W, respectively. These values are comparable with the estimates made at the Turbid Wake experiment (from 0.0007 to 0.0027 m^{-1}). Note the number density of ship wake bubbles is not necessarily proportional to the ship size [*Tate and Spitzer*, 1946]. The backscattering coefficients estimated for both wake experiments are in the upper range or greater than the estimated backscattering coefficients for background bubble populations measured in the ocean [Fig. 6b of *Zhang et al.*, 1998], suggesting that bubbles produced by the ship wake are more copious than bubbles generated under normal marine conditions.

4.5.4 Effect of turbulence-induced scattering

In this study, we have assumed that all the variability in the ship wake reflectance is due to bubbles generated. In addition to bubbles, ship wakes also produce turbulence, which in turn will cause small disturbance of the refractive index at the microscale.

These small-scale variations in the refractive index will increase the scattering magnitude, however, the effect is largely limited to the near forward angles (< 0.1 °) [*Bogucki et al.*, 1998]. Gordon [1993] showed that irradiance reflectance R (Eq. 4.1-a) and remote sensing reflectance R_{rs} (Eq. 4.1-b) could be estimated with an error less than 5% if the uncertainty in the small-angle scattering is limited to within 15°. Therefore, the wake turbulence-induced scattering has a negligible influence on the measured reflectance within the ship wakes, and we concluded that bubbles are responsible for essentially all of the observed variability in the observed reflectance.

4.6 Conclusions

Hyperspectral measurements of reflectances for both wake-free and wake waters confirm that bubbles enhance the reflectance and change its spectral signature, by increasing the backscattering coefficient. Since bubbles (unlike algal cells) are colorless by nature, variations in the color of water will only be modified based on the color prior to bubble injections. Blue waters demonstrate a shift to the green, while green waters show a blue-shift. The analysis, which has been designed for bubbles generated by ship wakes, equally applies to bubbles that are naturally created, e.g., by breaking waves.

We have also demonstrated that by simultaneously measuring reflectance and the number-size distribution of bubbles, the spectral backscattering coefficient, a parameter that is pivotal to ocean color remote sensing but difficult to measure properly, could be derived indirectly. The results shown are comparable to model predictions at least for the wavelengths below 550 nm.

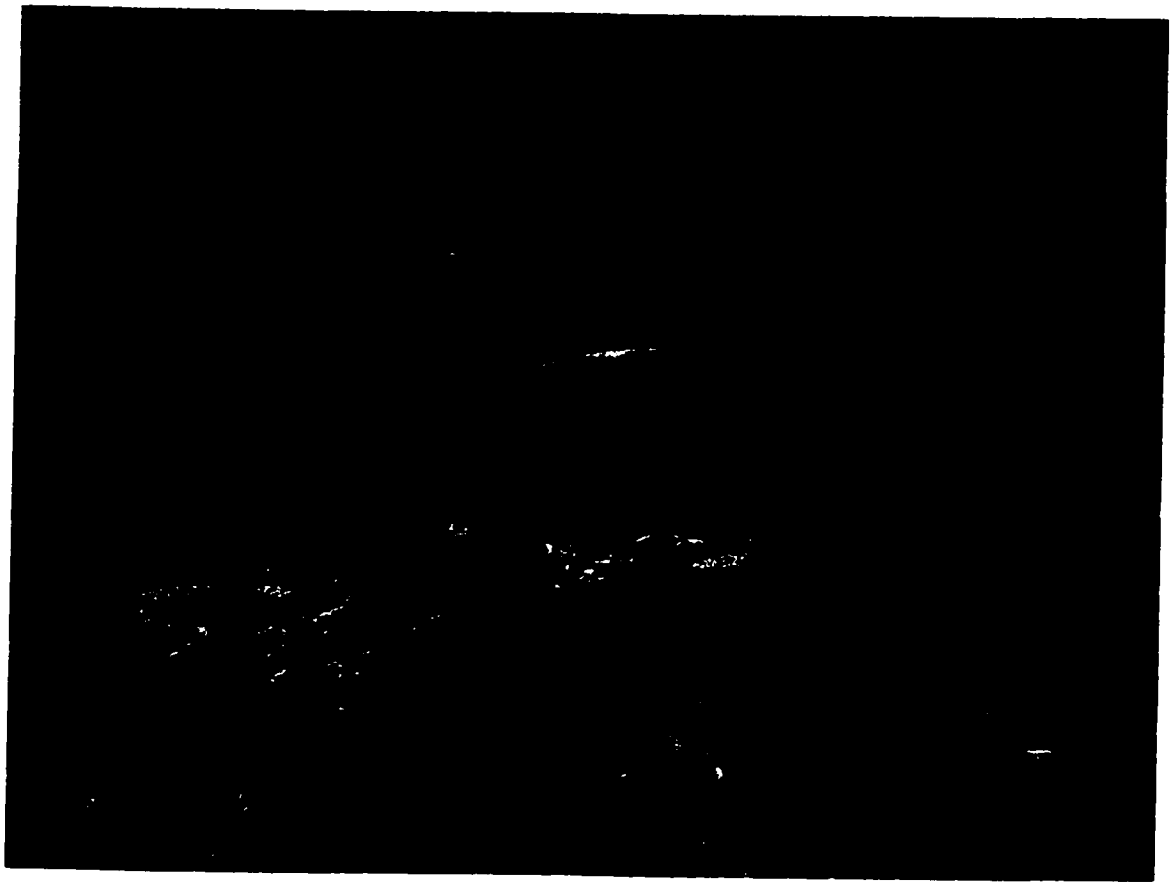

Figure 4.1 Wakes generated by R/V Mirai at the Equatorial Pacific Ocean.

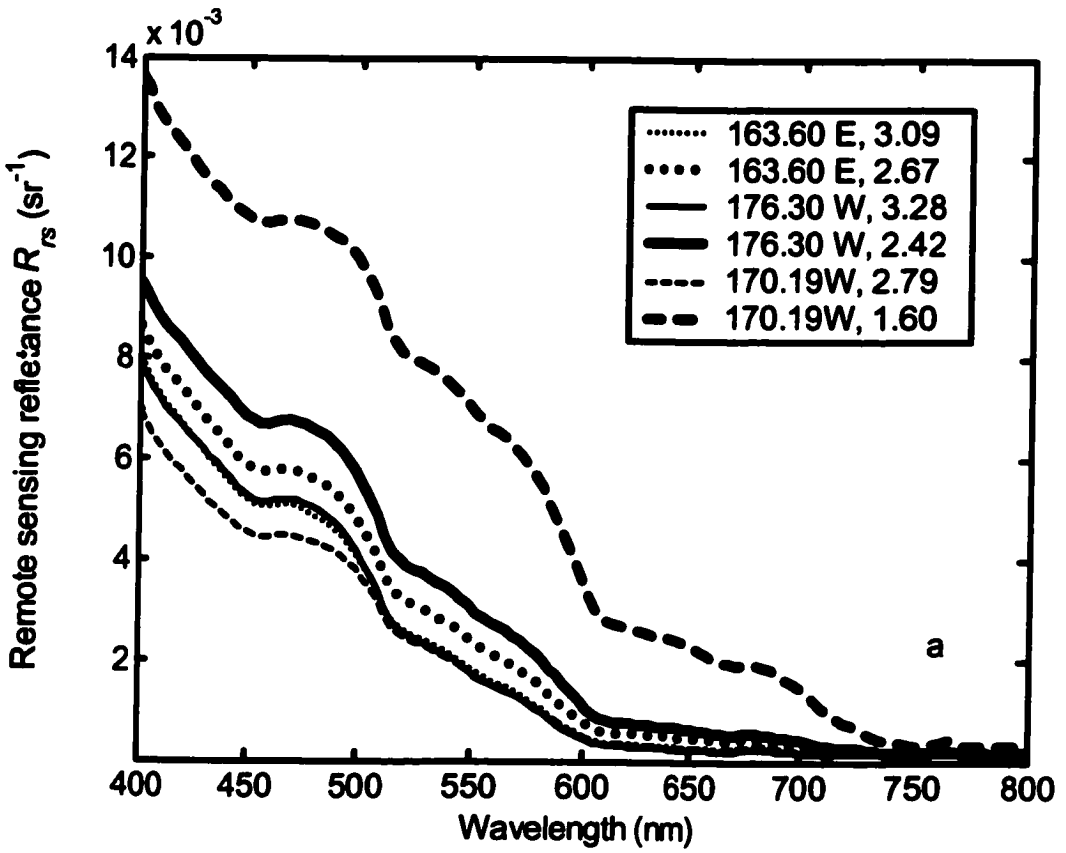

Figure 4.2-a The measured mean reflectances inside (thick lines) and outside ship wakes (thin lines) for Clear Wake experiment. The values shown in the legend are the longitudes and calculated blue-green ratios $\rho_{440\text{-}550}$ for each curve. All the measurements were on the Equator.

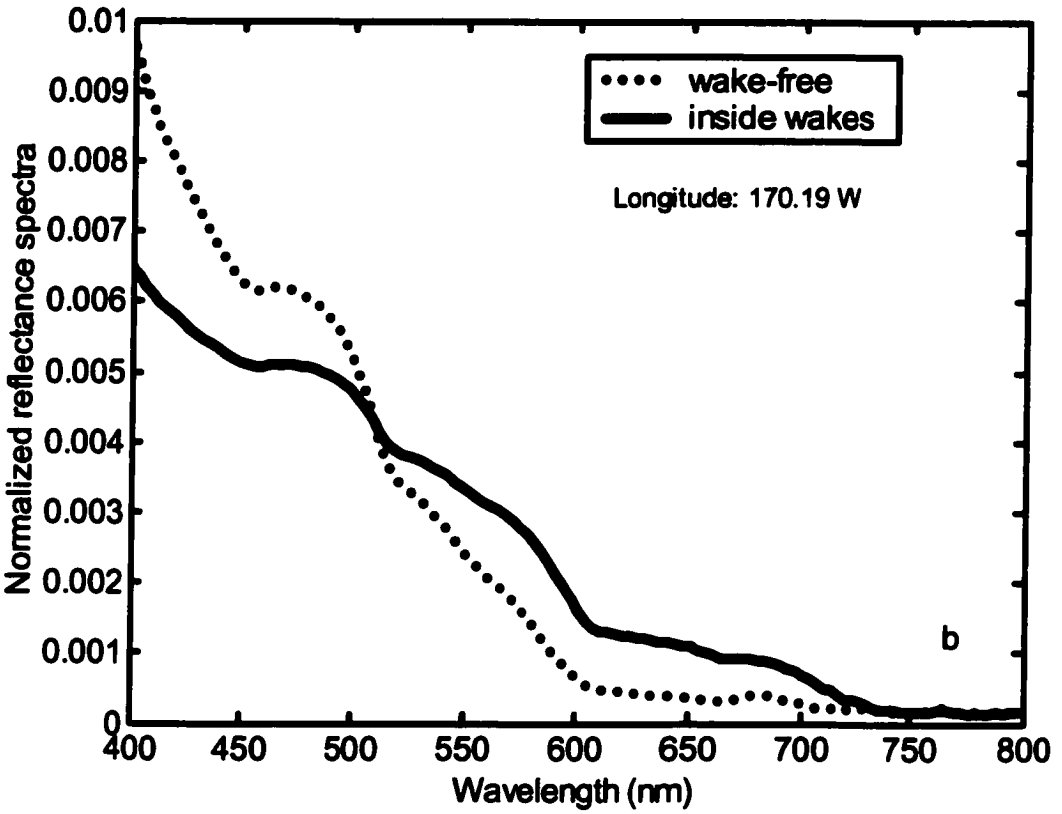

Figure 4.2-b The reflectance spectra normalized by the total reflectance over the entire spectrum for the station 170.19 W. The spectra are normalized by the integral over the waveband 400-800 nm.

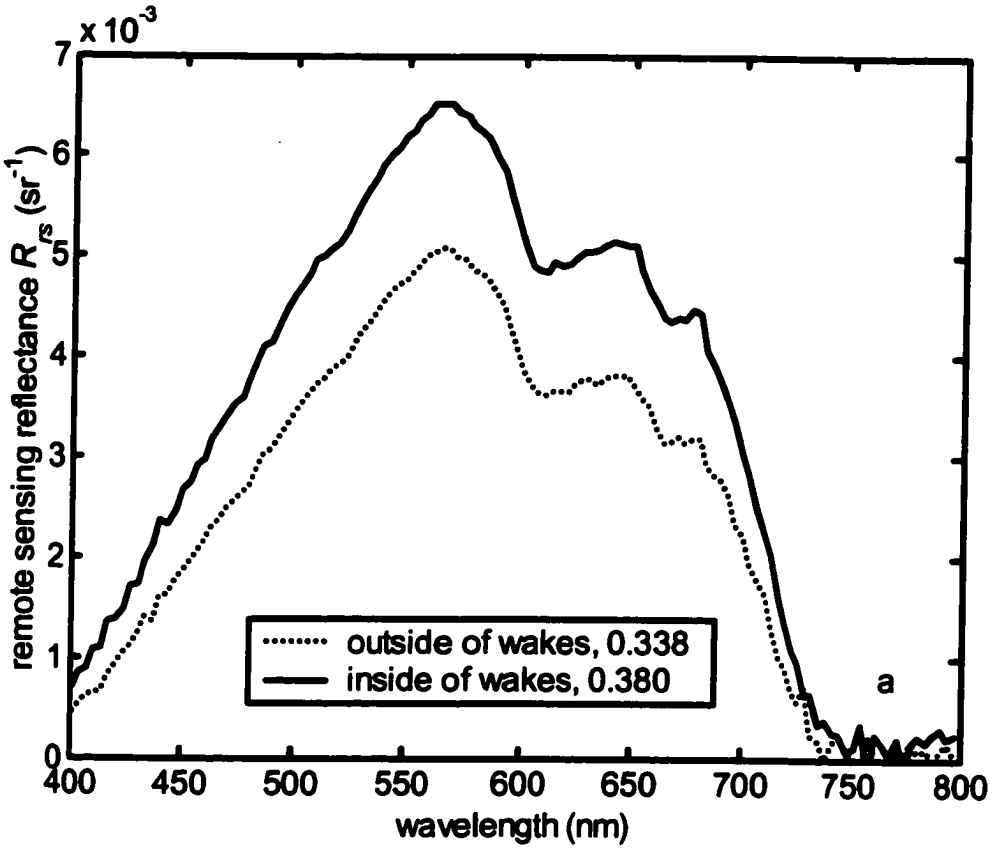

Figure 4.3-a The same as Fig 4.2-a except for Turbid Wake experiment.

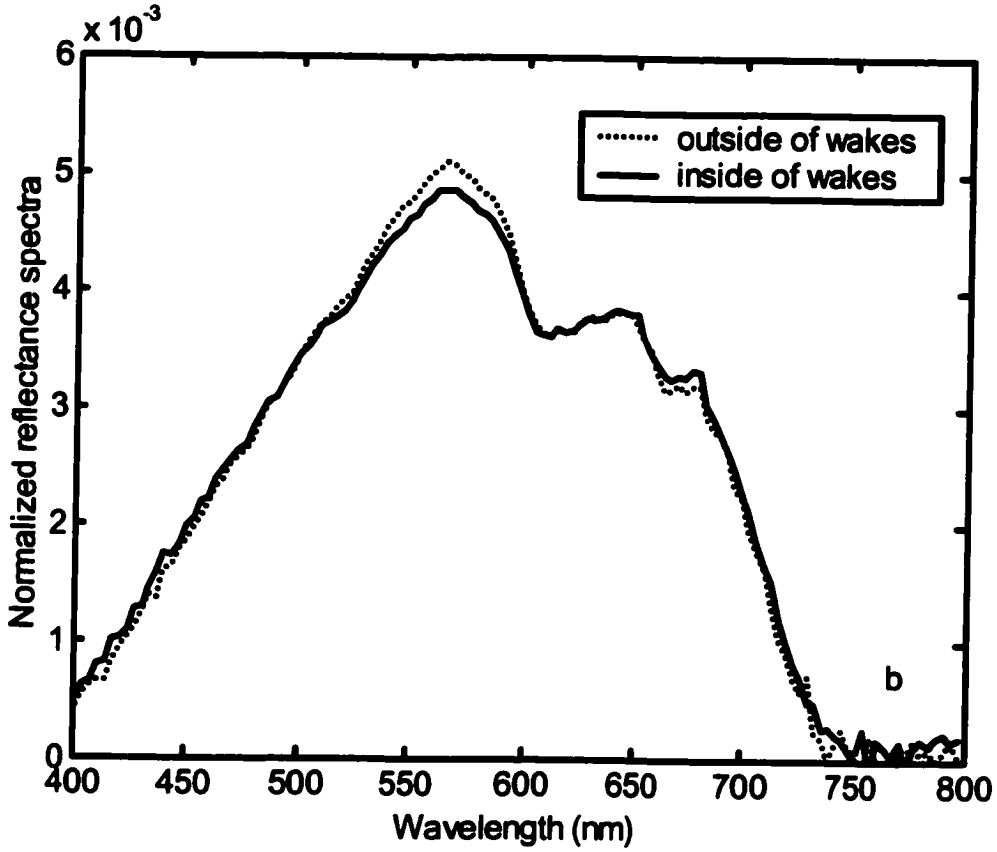

Figure 4.3-b The same as Fig 4.2-b except for Turbid Wake experiment.

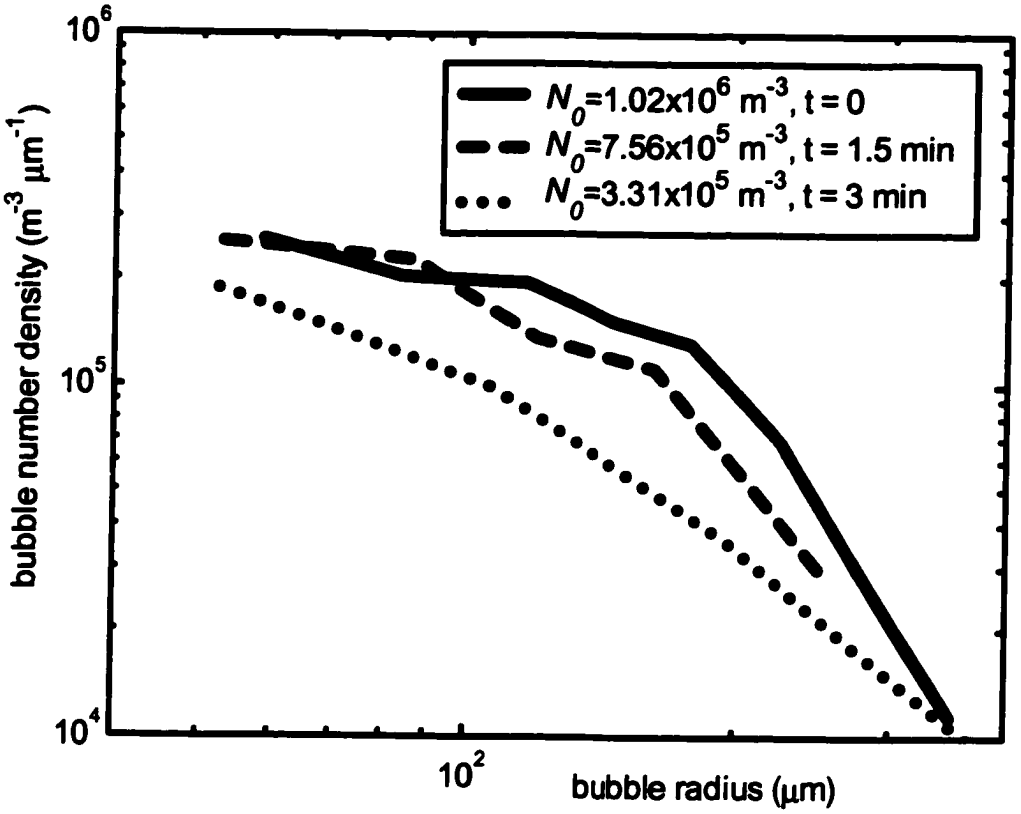

Figure 4.4 The size distributions of the ship wake bubbles determined by underwater camera observation at the Turbid Wake experiment, and their variation with time. N_0 in the legend denotes the total number density of bubbles that could be resolved by the camera.

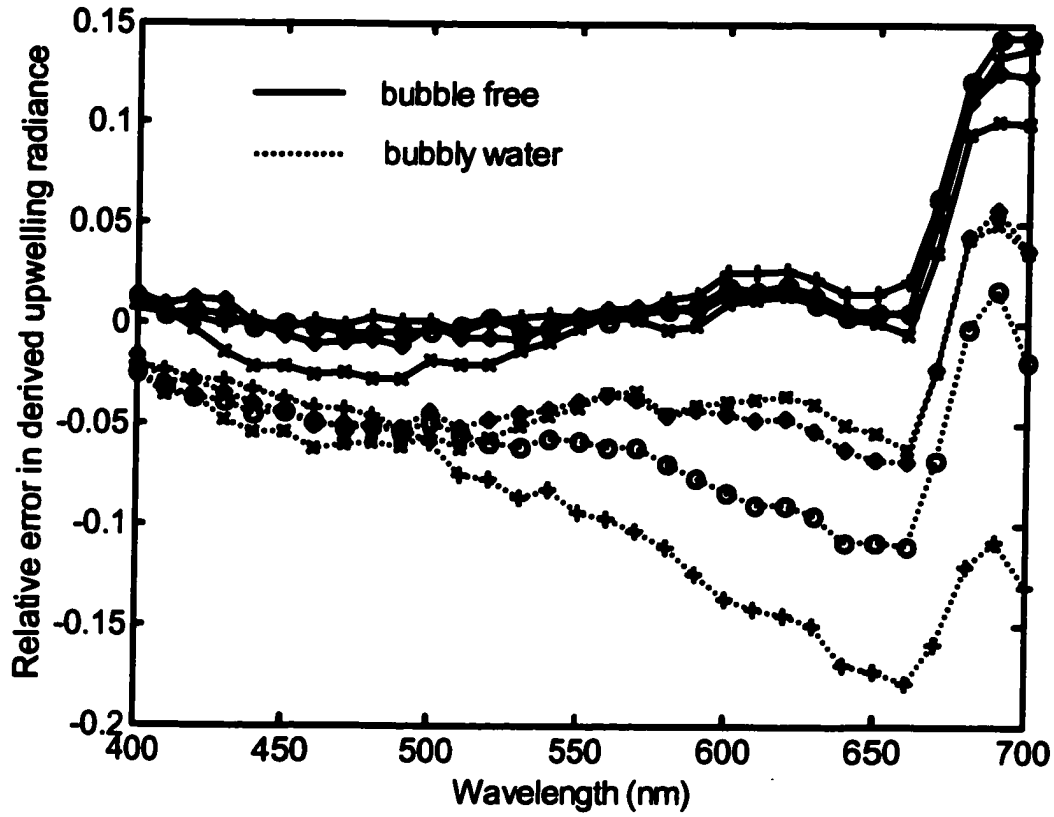

Figure 4.5 The relative error in the derived upwelling radiance just below the surface based on measurements taken at 0.6 m below the surface. The '+' is for [*Chl*] = 0.1 mg m^{-3}, the 'o' for [*Chl*] = 1.0 mg m^{-3}, the '◊' for [*Chl*] = 5.0 mg m^{-3}, the 'x' is for [*Chl*] = 10.0 mg m^{-3}.

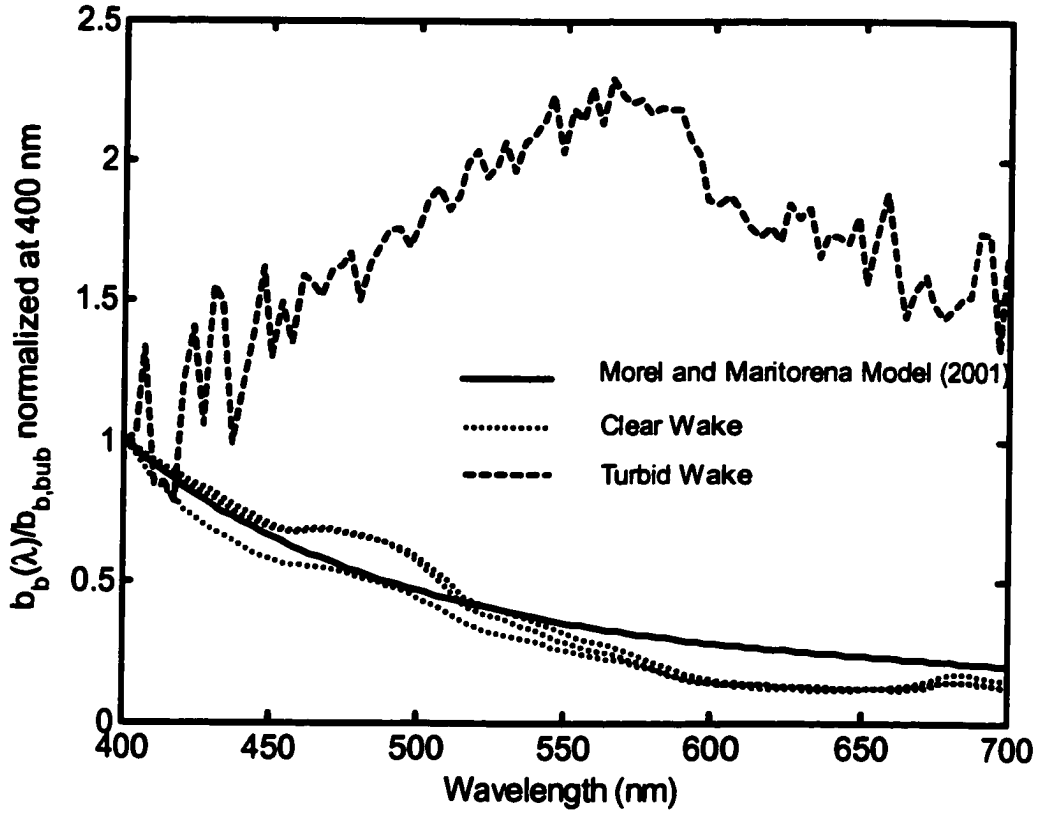

Figure 4.6 Spectral variations of $b_b(\lambda)$ normalized at 400 nm for both Clear Wake (dotted lines) and Turbid Wake (dashed lines) experiments. The modeled is $b_b(\lambda)$ also shown (solid line) for comparison.

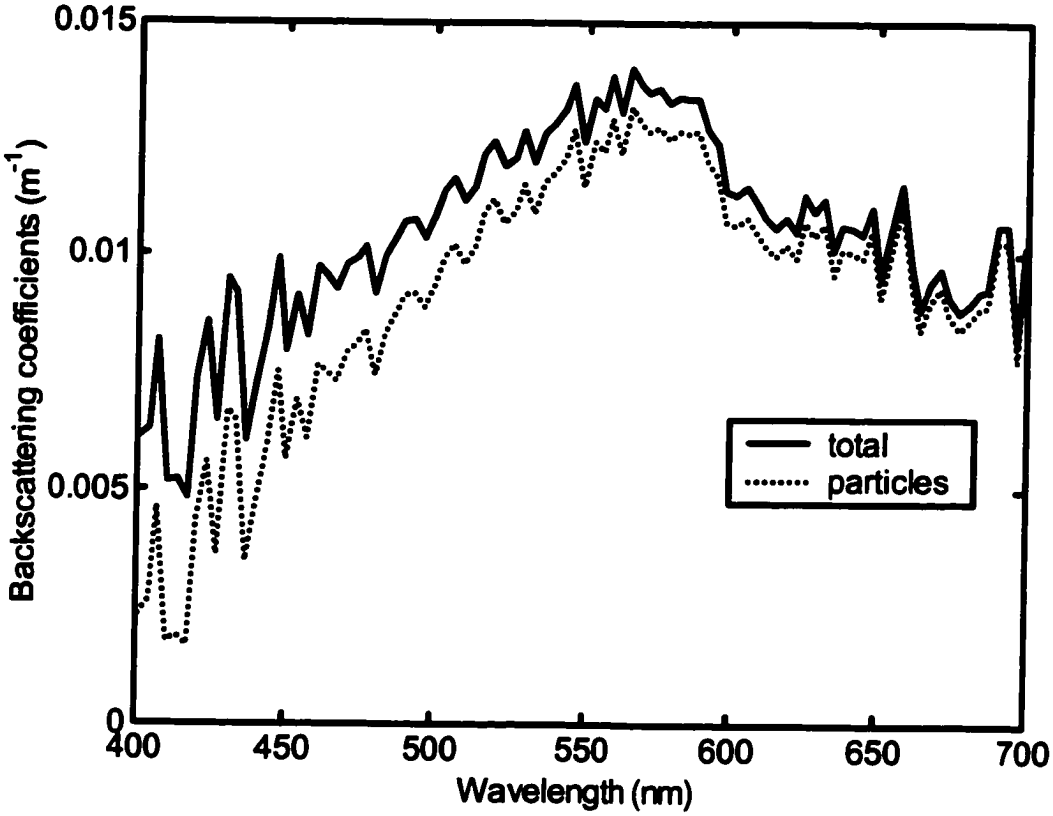

Figure 4.7 The spectral total backscattering coefficient (solid curve) for waters outside of the wakes estimated from Eq. 4.6. Also shown is the backscattering coefficient for particles (dotted curve), derived by subtraction of the theoretical backscattering coefficient of water molecules.

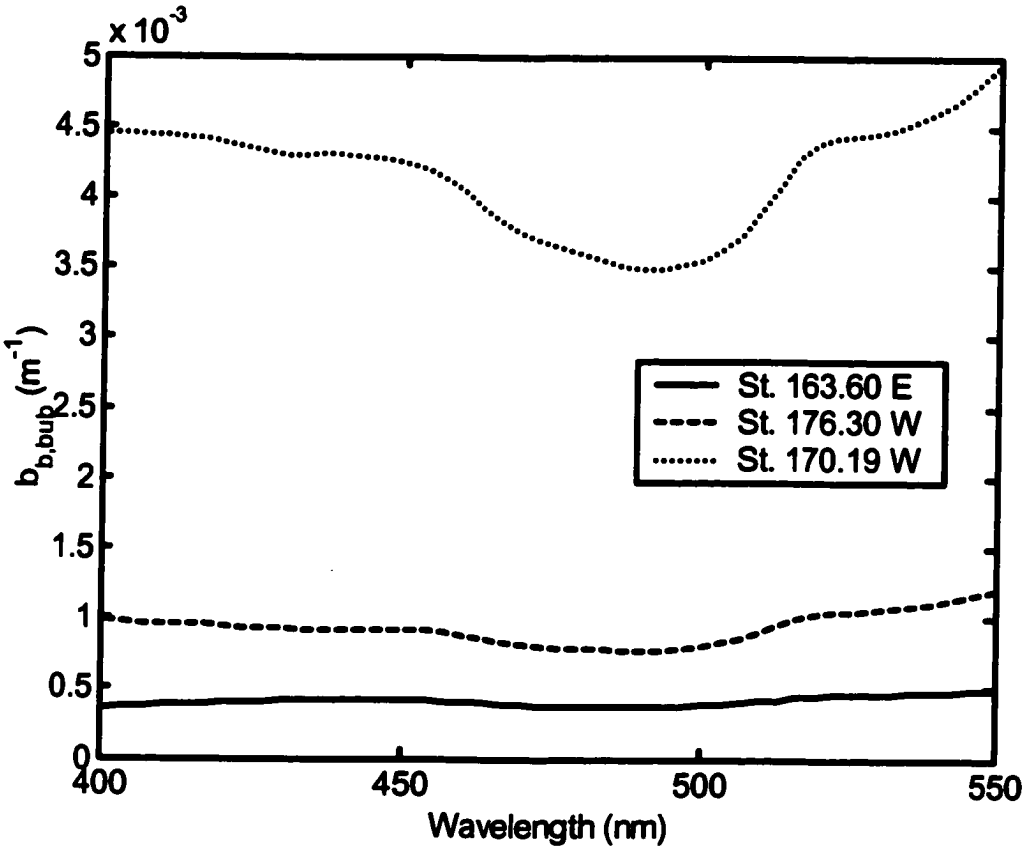

Figure 4.8 The estimated backscattering coefficients by wake bubbles from the measurements of the remote sensing reflectances of the ship wakes in the Clear Wake experiment.

General Conclusions

In this thesis, the scattering characteristics of bubbles have been systematically studied. The optical properties of natural bubble populations are fully determined by their volume scattering function, which has been derived from both Mie theory and laboratory observations. Classified as optically hard particles, namely, $|m-1| = 0.25$, where m is the relative refractive index of bubbles in the ocean, air bubbles display a strong efficiency in backward scattering as expected. A more salient feature, however, is the elevated scattering in the angular range of 60° and 80° owing to the total reflection at the local water-bubble interface when incident rays are at angles greater than the critical angle (48°). The enhancement is at least an order of magnitude higher than for other particles of the same size.

Consequently, the presence of bubbles, as injected by breaking waves or ship wakes, will alter the angular distribution of the underwater light field and increase the amount of light that leaves ocean. In response, the color of the ocean will also change; for example, ship wakes produced in open oceans are often observed to appear greener than the surrounding waters. The color shift, however, is not necessarily towards green. Unlike pigment-containing phytoplankton, which selectively absorb light, natural bubbles increase the backscattering of each wavelength by almost an equal amount, and as a result, the proportion of the various color components changes. The net effect in the color shift is determined by the backscattering spectrum prior to bubble injection. Blue dominant water becomes greener, while waters that backscatter more in the green than

blue will exhibit a blue shift. This has been verified by our ship wake experiments, where the reflectances at the sea surface were measured before and after bubble injections.

Within the context of satellite ocean color applications, the injected bubbles, especially through intense wave breaking events, will bias the derived geophysical products, such as chlorophyll concentration, because the presence of bubbles changes the color ratio. This problem is more serious in Case 1 clear waters [*Morel and Prieur*, 1977], for which both atmospheric correction schemes and bio-optical algorithms are believed to be well constrained. Without correction, the remote observation of ocean color, which only applies to cloud (water in air) free skies, will have to be further restricted to bubble (air in water) free waters.

The initiative of this study is to determine if natural bubble populations account for the missing backscattering in the upper ocean [*Morel and Bricaud*, 1981; *Morel and Ahn*, 1991; *Stramski and Kiefer*, 1991; *Zhang et al.*, 1998]. The question, however, remains open, because 1) the ubiquitous existence and observed concentration of background bubble populations in the global ocean needs to be further confirmed in both windy and quiescent conditions, and 2) the number and size distributions of natural bubbles less than 10 μm, a limit imposed by currently available *in situ* bubble sizing instruments, have yet to be determined.

Based on the published measurements on size and abundance of natural bubble populations, we have proven that bubbles could explain the unaccounted backscattering in the upper ocean. Therefore the emphasis of argument 1 is on the universal presence of natural bubble populations in the global oceans. Only if we fail on argument 1, then we

will proceed to argument 2 to investigate the importance of small bubbles that have yet been detected.

To continue the present study, the future work may be directed into two categories. The first will be to further prove the importance of natural bubble populations in the backscattering process in the upper ocean by carrying out extensive field experiments measuring the number-size distribution of bubbles and optical properties of water body. Along this direction, one may also want to investigate the role played by small bubbles, which involves the use of new instrumentations. The high-frequency acoustic backscattering system that we have used in the LEO-15 field experiment could possibly provide such information (by the time of my writing the thesis, the data was not yet available). The other promising technique involves the use of holographic microscope, which could provide the number density and size distribution of particles at micron sizes. A prototype was available at the Department of Physics, Dalhousie University [*Xu et al.*, 2001].

The second category is concerned with applications. An immediate application is to examine how the natural bubble injecting events, such as hurricanes, affect the satellite retrieval of global phytoplankton concentration. Also of interest is to develop an atmospheric correction scheme for the retrieval of true background reflectance of the upper ocean where bubble layers are present due to intensive wave breakings. However, this application needs a reliable model to link the size-number properties of natural bubbles to wind speeds.

Appendix A Radiometric quantities and optical properties

The radiative transfer and the definitions of optical properties for the ocean or the atmosphere are based on the Geometrical Radiometry. According to Preisendorfer [1976a], radiometry is the science of the measurement of radiant energy. Geometrical radiometry is the union of Euclidean geometry and radiometry: it measures and describes the flow of radiant energy of given frequency through volumes, across surfaces, along lines, and at points in space.

Almost all radiometric quantities and optical properties in ocean optics are wavelength dependent for the spectral range from ultraviolet to infrared. Sometimes the wavelength dependency is suppressed for the sake of simplicity.

A.1 Radiometric quantities

The fundamental radiometric quantity is spectral radiance. Assuming a horizontally homogeneous and plane-parallel water body, the radiance $L(z, \theta, \varphi, \lambda)$ is defined as radiant flux Φ at depth z in a given direction (θ, φ) per unit solid angle (Ω) per unit projected area (A), i.e.,

$$L(z,\theta,\varphi,\lambda) = \frac{d^2\Phi(z,\lambda)}{dA\cos(\theta)d\Omega}. \quad (\mathrm{W\ m^{-2}\ sr^{-1}}) \qquad \text{A1}$$

where θ denotes zenith angle and φ azimuth angle of the travelling direction of photons, and $d\Omega = \sin(\theta)d\theta d\varphi$. The other radiometric quantities, intensity and irradiance, could

be derived from radiance distribution. The intensity $I(\theta, \varphi)$, which often related to a point source, is defined as radiant flux Φ per solid angle at direction (θ, φ).

$$I(z,\theta,\varphi) = \frac{d\Phi}{d\Omega} = \int_A L(z,\theta,\varphi)dA \qquad (\mathrm{W\ sr^{-1}}) \qquad \text{A2}$$

The irradiance E is defined as radiant flux Φ incident on an element of a surface containing the point under consideration divided by the area of the element, i.e.,

$$E(z,\theta,\varphi) = \frac{d\Phi}{dA} = \int_\Omega L(z,\theta,\varphi)d\Omega \qquad (\mathrm{W\ m^{-2}})$$

Of particular interests in practice are the upwelling irradiance $E_u(z)$ and downwelling irradiance $E_d(z)$ (W m^{-2}), which are defined as,

$$E_u(z) = -\int_{\varphi=0}^{2\pi}\int_{\theta=\frac{\pi}{2}}^{\pi} L(z,\theta,\varphi)\cos(\theta)\sin(\theta)d\theta d\varphi\,, \text{ and} \qquad \text{A3}$$

$$E_d(z) = \int_{\varphi=0}^{2\pi}\int_{\theta=0}^{\frac{\pi}{2}} L(z,\theta,\varphi)\cos(\theta)\sin(\theta)d\theta d\varphi\,. \qquad \text{A4}$$

Note the positive direction of the vertical axis is downward. The minus sign of Eq. A3 is due to that $\cos(\theta)$, and therefore the integration, are negative from $\pi/2$ to π. The vector irradiance is defined as,

$$\vec{E}(z) = \int_{\varphi=0}^{2\pi}\int_{\theta=0}^{\pi} L(z,\theta,\varphi)\cos(\theta)\sin(\theta)d\theta d\varphi = E_d(z) - E_u(z)\,. \qquad \text{A5}$$

The vector irradiance gives the direction and the magnitude of the irradiance field. The upwelling scalar irradiance and downwelling scalar irradiance are defined as,

$$E_{ou}(z) = \int_{\varphi=0}^{2\pi} \int_{\theta=\frac{\pi}{2}}^{\pi} L(z,\theta,\varphi)\sin(\theta)d\theta d\varphi, \text{ and} \qquad \text{A6}$$

$$E_{od}(z) = \int_{\varphi=0}^{2\pi} \int_{\theta=0}^{\frac{\pi}{2}} L(z,\theta,\varphi)\sin(\theta)d\theta d\varphi. \qquad \text{A7}$$

The total scalar irradiance is defined as,

$$E_o(z) = \int_{\varphi=0}^{2\pi} \int_{\theta=0}^{\pi} L(z,\theta,\varphi)\sin(\theta)d\theta d\varphi, \qquad \text{A8}$$

which, divided by light speed, gives a measure of the total radiant energy per unit volume. Gershun's law establishes the connection between the vector irradiance and the scalar irradiance in a source free medium, i.e.,

$$\frac{d\vec{E}(z)}{dz} = -aE_o(z). \qquad \text{A9}$$

where a is volume absorption coefficient, which will be defined later.

A.2 Optical properties

The optical properties of a water body can be divided into 2 categories, Inherent Optical Properties (IOP's) and Apparent Optical Properties (AOP's) [*Preisendorfer*, 1976b]. The IOP's of a medium depend only on the substances comprising the medium, while the AOP's are determined by IOP's as well as geometric structure of light fields.

A.2.1 Macroscopic IOP's

The fundamental IOP's are the volume attenuation coefficient c and the volume scattering function β. The volume attenuation coefficient gives the lost beam radiant flux

($d\Phi$) per unit path length (dl) per unit incident beam radiant flux (Φ), i.e., $c = \frac{d\Phi}{\Phi\, dl}$.

Similarly, the volume scattering function gives the scattered radiant flux ($d\Phi$) per unit incident path length (dl) per solid angle ($d\Omega$) at direction (θ, φ), i.e.,

$$\beta(\theta', \varphi' \rightarrow \theta, \varphi) = \beta(\psi) = \frac{d\Phi}{\Phi\, dl\, d\Omega} = \frac{\frac{d\Phi}{d\Omega}}{\frac{\Phi}{dA'} dA'\, dl} = \frac{I(\psi)}{E\, dV}, \text{ or}$$

$$\frac{d\Phi}{\Phi\, dl\, d\Omega} = \frac{\frac{d\Phi}{d\Omega\, dA}}{\frac{\Phi}{dA'}\frac{dA'\, dl}{dA}} = \frac{L(\psi)}{E\, dr} \qquad \text{A10}$$

Refer to Figure A1 for definition of those symbols used in Eq. A10. The physical interpretation of the volume scattering function is the scattered intensity per unit incident irradiance per unit volume of water. The scattering angle, ψ, is computed as,

$$\cos(\psi) = \cos(\theta)\cos(\theta') + \sin(\theta)\sin(\theta')\cos(\varphi - \varphi'). \qquad \text{A11}$$

The other IOP's that can be derived from the volume attenuation coefficient and the volume scattering function are the volume absorption coefficient, $a(\text{m}^{-1})$, the volume scattering coefficient, $b(\text{m}^{-1})$, the volume backscattering coefficient, b_b (m^{-1}) and the normalized volume scattering function (or phase function) $\overline{\beta}$.

$$b = 2\pi \int_{\psi=0}^{\pi} \beta(\psi)\sin(\psi)d\psi. \qquad \text{A12}$$

$$b_b = 2\pi \int_{\psi=\frac{\pi}{2}}^{\pi} \beta(\psi)\sin(\psi)d\psi. \qquad \text{A13}$$

$$a = c - b. \qquad \text{A14}$$

$$\overline{\beta}(\psi) = \frac{\beta(\psi)}{b}. \qquad \text{A15}$$

By definition, $2\pi \int_{\psi=0}^{\pi} \overline{\beta}(\psi)\sin(\psi)d\psi = 1$. Another useful IOP is the backscattering ratio,

$$\overline{b_b} = \frac{b_b}{b} = 2\pi \int_{\psi=\frac{\pi}{2}}^{\pi} \overline{\beta}(\psi)\sin(\psi)d\psi. \qquad \text{A16}$$

The IOP's also satisfy the additivity law, which states that the total coefficient could be partitioned into the contribution from each component that comprises the medium. For instance, the IOP's of an ocean water body could be divided into summations of those due to pure water, phytoplankton, bacteria, dissolved organic matter, particles and bubbles.

A.2.2 Microscopic IOP's

Interaction of electromagnetic waves by any system is related to the heterogeneity of that system: heterogeneity on the molecular scale or on the scale of aggregations of many molecules. Regardless of the type of heterogeneity, the underlying physics of scattering is the same for all systems. Matter is composed of discrete electric charges: electrons and protons. If an obstacle, which could be a single electron, an atom or molecule, a solid or liquid particle, is illuminated by an electromagnetic wave, electric charges in the obstacle are set into oscillatory motion by the electric field of the incident wave. Accelerated electric charges radiate electromagnetic energy in all directions: it is this secondary radiation that is called the radiation scattered by the obstacles.

In addition to reradiating electromagnetic energy, the excited elementary charges may transform part of the incident electromagnetic energy into other forms (thermal energy, for example), a process called absorption.

Everything except a vacuum is heterogeneous in some sense, and therefore, all media, including pure gases, liquids, or solids, scatter light. However, solids, liquids, and many gases are optically dense: the molecular separation is much less than the wavelength of the incident light. In solids and liquids the molecular separation is about 2-3 Å, whereas for gases at standard temperature and pressure the average separation is about 30 Å. Thus, each molecule is acted on not only by the incident field but also by the resultant of the secondary fields of all the other molecules, and inside the medium the secondary waves superpose on each other and on the incident wave. The net effect of the solution to this problem leads to, for example, diffuse reflection by rough surface, or diffraction by edges, or specular reflection and refraction at optically smooth interface. The exact patterns of light scattering for optically dense medium, such as refractive angle or reflectance, are determined by the refractive index of the medium, which, in turn, depends on the number of molecules per unit volume and the polarizability of a single molecule.

The IOP's of such pure medium, such as pure water or seawater, are assumed to be known *a priori*, and do not change very much, to the extend that the refractive index is constant. Pure seawater scatter about 30% more than pure water because the ions resulting from dissolved salts introduce added heterogeneity [*Morel*, 1973]. For oceans, remain to be defined are the IOP's for anything else other than pure water molecules and ions, for which we collectively call them particles. Note, practically particles tend to be

classified into dissolved (a practical definition is to pass through filters with pore size of 0.2 μm) and particulate (retained by the filter). Here we make no difference between them as far as their optical properties are concerned. For example, it is normally assumed that the coloured dissolved organic matter (CDOM) do not scatter, an argument might be due to the absorption by CDOM dominates over the scattering, which hence is negligible. But the underlying physics of scattering as we just introduced above dictates that CDOM must scatter, no matter how small is the scattering magnitude, which remains to be determined.

The IOP's of a population of particles could be estimated as,

$$j = \int_{r_{min}}^{r_{max}} Q_j \pi r^2 N(r) dr = N_0 \overline{Q_j s}, \qquad \text{A17}$$

where j denotes a, b, b_b, c or β, and Q_j is the corresponding efficiency factor that for spherical particles can be calculated using Mie theory [*Bohren and Huffman*, 1983] and is determined by the particle size, incident light wavelength, medium refractive index and particle refractive index. $N(r)$ is particle number density per unit volume per unit radius interval, and r_{min} and r_{max} are the minimum and maximum radius of particles. N_0 ($= \int_{r_{min}}^{r_{max}} N(r) dr$) is the total number density of particles, $\overline{Q_j}$ ($= \frac{\int_{r_{min}}^{r_{max}} Q_j \pi r^2 N(r) dr}{\int_{r_{min}}^{r_{max}} \pi r^2 N(r) dr}$) is the

mean efficiency factor, and $\bar{s}\left(=\frac{\int_{r_{min}}^{r_{max}} \pi r^2 N(r)dr}{\int_{r_{min}}^{r_{max}} N(r)dr}\right)$ is the mean geometrical cross-section area.

Particles in a collection are electromagnetically coupled: each particle is excited by the external field and the resultant field scattered by all the other particles; but the field scattered by a particle depends on the total field to which it is exposed. An implicit assumption of Eq. A17 is that the number of particles is sufficiently small and their separation sufficiently large that, in the neighbourhood of any particle, the total field scattered by all the particles is small compared with the external field. With this assumption the total scattered field is just the sum of the fields scattered by the individual particles, each of which is acted on by the external field in isolation from the other particles.

In order to be consistent with their definition, the solutions containing particles, whose IOP's are to be measured, should be dilute enough that single scattering among particles prevails.

A.2.3 AOP's

Most of the AOP's are defined through irradiance. The average cosines are the ratio of the vector irradiances to the scalar irradiances, i.e.,

$$\bar{\mu}(z)=\frac{\vec{E}(z)}{E_o(z)};\quad \bar{\mu}_d(z)=\frac{E_d(z)}{E_{od}(z)};\quad \bar{\mu}_u(z)=\frac{E_u(z)}{E_{ou}(z)}. \qquad \text{A18}$$

The average cosines describe the shape of the radiance distribution, e.g., for a uniform radiance distribution, the average cosine would be 0.5 and for a collimated beam of zenith angle θ, the average cosine would be $\cos(\theta)$. Correspondingly, the reverse of the average cosine gives the mean distance the irradiance field travel per unit depth. The vertical attenuation coefficient for a radiometric quantity is given by,

$$K_X(z) = -\frac{1}{X(z)}\frac{dX(z)}{dz}, \qquad \text{A19}$$

where X could be any of the radiance or irradiance just defined above. The irradiance ratio is defined as,

$$R(z) = \frac{E_u(z)}{E_d(z)}. \qquad \text{A20}$$

The most useful irradiance ratio within the remote sensing context is $R(0^-)$, which is defined just beneath the air-water interface. The μ's, K's and R are AOP's.

Note the AOP's are measures of the optical properties in reality with varying incident light field and particle concentrations. Also contributing to the AOP's is the multiple scattering, which has been assumed to be negligible in defining the IOP's. The radiative transfer equation, which will be introduced immediately, takes into account all these factors.

A.3 Radiative transfer equation

The radiative transfer equation provides the connection between the AOP's and the IOP's. For a plane-parallel water body, the radiative transfer equation can be expressed as:

$$\cos(\theta)\frac{dL(\lambda,z,\theta,\varphi)}{dz} = -c(\lambda,z)L(\lambda,z,\theta,\varphi) + \int_0^{2\pi}\int_0^{\pi} L(\lambda,z,\theta',\varphi')\beta(\lambda,z,\psi)d\theta' d\varphi', \quad \text{A21}$$

where c is the volume attenuation coefficient (m^{-1}), β is the volume scattering function (m^{-1} sr^{-1}), and L is the radiance (W m^{-2} sr^{-1}). The position and direction of the radiance is determined by its depth z (m) and its zenith (θ) and azimuth (φ) angles. The ψ is the scattering angle between the incident radiance $L(\lambda,z,\theta',\varphi')$ and the scattered radiance $L(\lambda,z,\theta,\varphi)$.

The change of the radiance along the path $dz/cos(\theta)$ is due to 1) the removed radiance (the first term of RHS of Eq. A21), and 2) the added radiance by scattering (the second term of RHS of Eq. A21). This second term accounts for the multiple scattering. Integration of Eq. A21 over the entire space (4π) will lead to Eq. A9.

A.3.1 Optical models

Even though Eq. A21 provide the ultimate solution in deriving radiance field from IOP's, the differential-integral form of the equation is difficult to solve. Some optical models therefore have been established, starting from Eq. 21 and with certain assumptions, to link the AOP's, which are relatively easier to measure but more variable (e.g. varying with incident light field), with the IOP's, which are difficult to measure but invariant with ambient light field and amenable to theoretical interpretation. Most of the optical models aim to provide an analytical solution of AOP's for given IOP's, but inevitably introducing other parameters, either explicitly or implicitly describing the

spatial distribution of light field. For example, for infinitely deep ocean, the irradiance ratio at the surface can related to the absorption coefficient through,

$$R(0^-) = \frac{K_d - \underline{\underline{a}}\,\frac{\bar{\mu}}{\mu_d}}{K_u + \underline{\underline{a}}\,\frac{1}{\mu_u}} = \frac{\underline{\underline{a}}\,\frac{\bar{\mu}}{\mu_u} - 1}{1 - \underline{\underline{a}}\,\frac{\bar{\mu}}{\mu_d}}. \qquad \text{A22}$$

Also a very useful inequality can be derived constraining the attenuation coefficient for downwelling irradiance [see e.g. *Mobley*, 1994],

$$a \le K_d \overline{\mu_d} \le c. \qquad \text{A23}$$

When a is much greater than b_b, Eq. A22 can be further simplified into [*Gordon et al.*, 1975; *Morel and Prieur*, 1977; *Kirk*, 1981],

$$R(0^-) = f\frac{b_b}{a}, \qquad \text{A24}$$

where f is a parameter (an AOP) that depends on the illumination conditions (e.g. solar zenith angle) and the water optical properties (e.g., single scattering albedo, shape of the volume scattering function, and ratio of molecular backscattering to that due to particles) [*Kirk*, 1984; *Gordon*, 1989; *Morel and Gentili*, 1991].

Taking into account the air-water interface effect explicitly, the water-leaving radiance $L_w(\theta,\varphi)$ is connected to the irradiance ratio just beneath the surface through,

$$L_w(\theta,\varphi) = \frac{t(\theta' \to \theta)T(0^+ \to 0^-)}{n_w^2(1 - R(0^-)r(0^-))}\frac{1}{Q(0^-,\theta')}R(0^-), \qquad \text{A25}$$

where $t(\theta' \rightarrow \theta)$ is the beam transmittance from water to air, $T(0^+ \rightarrow 0^-)$ is the downwelling irradiance transmittance from air to water, n_w is the water refractive index, $r(0^-)$ is the upwelling irradiance reflectance just beneath the interface. The Q factor is introduced as,

$$Q(0^-,\theta',\varphi) = \frac{E_u(0^-)}{L(0^-,\theta',\varphi)}, \qquad \text{A26}$$

which would be π for a Lambertian upwelling light field. Figure A.2 shows the geometrical angular configuration of these quantities.

By Eqs. A24 and A25, a simple analytic model can be established between spectral water-leaving radiance and inherent optical properties of water, however at the expenses of introducing 2 new parameters Q and f. The f varies from 0.29 to 0.48, primarily depending on the solar angle, and the Q varies from 0.3 to 6.5; however the ratio f/Q within the angular range of remote sensing, varies in a quite limited range from 0.07 to 0.18 [*Morel and Gentili*, 1996].

Another approximation shows that [*Zaneveld*, 1995],

$$\frac{L(0^-,\theta,\varphi)}{E_{od}(0^-)} \approx \frac{\beta(\theta_m,\varphi_m \rightarrow \theta,\varphi)}{a(0^-)(1+m(0^-))}, \qquad \text{A27}$$

where the denominator indicates the volume scattering function from the direction (θ_m,φ_m) of the downwelling radiance maximum to the direction (θ,φ), and m is a function of b/c. The biggest assumption of Eq. A27 is that the upwelling light can be modeled as being due to single scattering from light at the maximum of the radiance distribution. Note the use of downwelling scalar irradiance instead of the planar irradiance in the equation, which comes naturally from the radiative transfer equation.

These optical models link the water-leaving radiance with the IOP's, which are assumed to be able to be represented by uniform, mean values. Gordon [1992] found that the nonuniform and incoherent distribution of a and b_b could lead to substantial error (~20% or greater) in Eq. A24. In such cases or when the prediction of the magnitude and the angular distribution of the water-leaving radiance is desired, the exact solution of the radiative transfer equation will be necessary.

A.4 Bio-optical models

The combination of additive law for IOP's and an optical model result in a bio-optical model. For example, in case I waters, where phytoplankton predominantly determines the optical properties of ocean, the IOP's could be parameterized as:

$$\begin{aligned} a(\lambda) &= a_w(\lambda) + a_p(\lambda) + a_{CDOM}(\lambda) \\ b(\lambda) &= b_w(\lambda) + b_p(\lambda) \\ b_b(\lambda) &= 0.5 b_w(\lambda) + \overline{b_{b,p}}(\lambda) b_p(\lambda) \end{aligned} \qquad \text{A28}$$

where the subscripts w, p, $CDOM$, denote water, particles, and coloured dissolved organic matter, respectively. The absorption and scattering coefficients of particles are empirically related to the phytoplankton concentration [chl] (mg m^{-3}), through, e.g. [*Bricaud et al.*, 1998; *Loisel and Morel*, 1998],

$$\begin{aligned} a_p(\lambda) &= A_p(\lambda)[chl]^{E_p(\lambda)} \\ b_p(\lambda) &= \frac{660}{\lambda} 0.347 [chl]^{0.766} \\ c_p(\lambda) &= b_p(\lambda) + a_p(\lambda) \end{aligned} \qquad \text{A29}$$

where $A_p(\lambda)$ and $E_p(\lambda)$ are empirical coefficients. The scattering and absorption coefficients for water are known [*Morel*, 1974; *Smith and Baker*, 1981; *Pope and Fry*, 1997]. The absorption due to CDOM is modelled as [e.g. *Bricaud et al.*, 1981]:

$$a_{CDOM}(\lambda) = a_{CDOM}(440)e^{-0.014(\lambda-440)}. \qquad \text{A30}$$

The biggest uncertainty in the current bio-optical models is the backscattering ratio for particles, because there have been very few *in situ* measurements. The laboratory observations found the backscattering ratio by phytoplankton species between 0.0002 and 0.004 [*Ahn et al.*, 1992]. The backscattering ratio derived from Petzold's volume scattering function measurements [*Petzold*, 1972] is 0.04 for deep ocean water, 0.014 for California coastal water and 0.02 for San Diego harbour water. The previously proposed model for backscattering is [*Gordon et al.*, 1988; *Morel*, 1988],

$$\overline{b_{b,p}}(\lambda) = 0.002 + 0.02(0.5 - 0.25\log([chl]))\frac{550}{\lambda}. \qquad \text{A31}$$

However, arguing that the maximum backscattering ratio of 0.02 when [Chl] = 0.01 mg m-3 was set too high for biogenic Case 1 waters, Morel and Maritorena [2001] modified Eq. A29,

$$\begin{aligned} &\overline{b_{b,p}}(\lambda) = 0.002 + 0.01(0.5 - 0.25\log([Chl]))(\frac{550}{\lambda})^{\upsilon}, \\ &\upsilon = 0.5(\log([Chl]) - 0.3) \qquad 0.02 < [Chl] < 2\ mg\,m^{-3} \\ &\upsilon = 0 \qquad\qquad\qquad\qquad 2\ mg\,m^{-3} < [Chl] \end{aligned} \qquad \text{A32}$$

It should be emphasized that while the models for particle absorption and scattering coefficients are derived from large global data sets, the model for particle backscattering is largely based on assumptions due to the lack of *in situ* data.

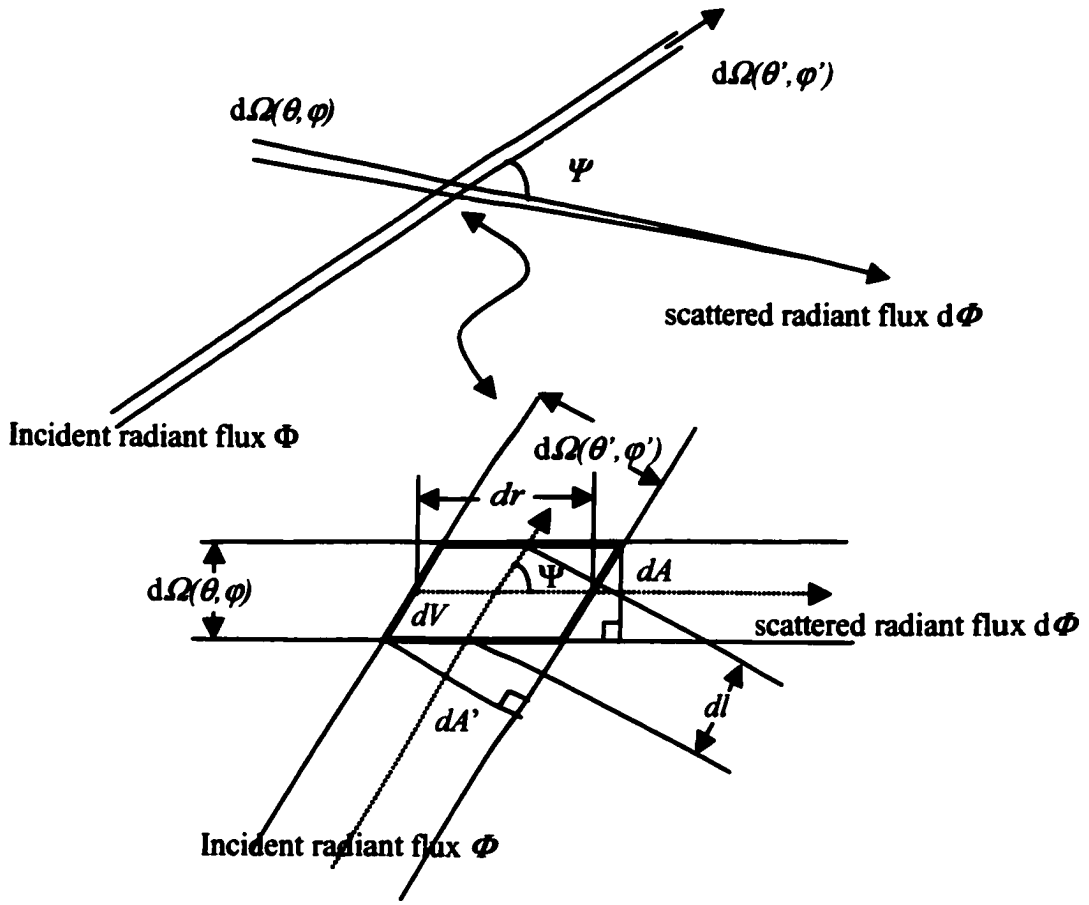

Figure A.1 Geometry used in defining volume scattering functions.

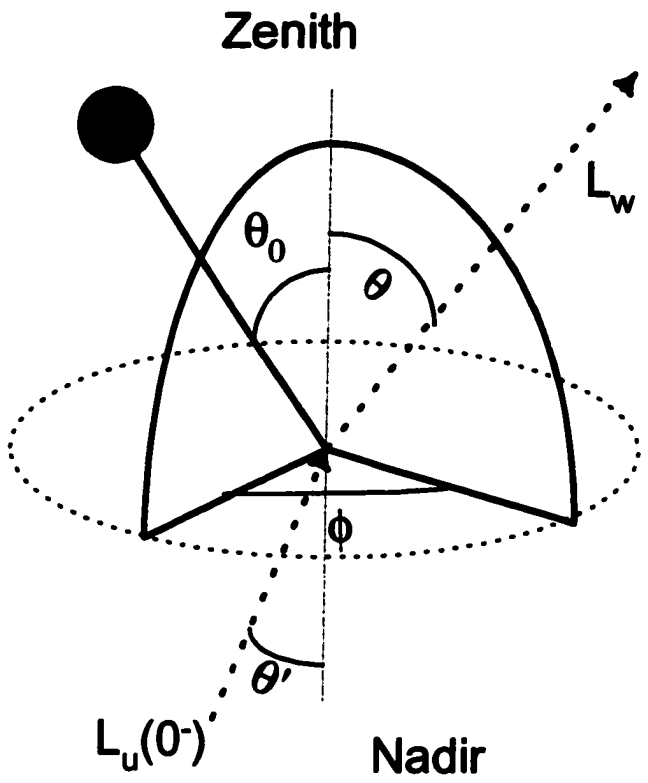

Figure A.2 Schematic views of the geometry of the angular configurations related to in-water and above-water quantities. The zenith angles correspond to the direction of photon travel and are measured from the local zenith for water-leaving radiance (θ) and zenith sun angle (θ_0), or from nadir when dealing with the in-water upwelling radiance (θ'). The azimuth angle φ is 0 and π for the sun and the antisolar directions, respectively.

Appendix B Natural bubbles

B.1 Mechanics and dynamics of individual bubbles

For a free bubble of radius r in static equilibrium with water, its internal pressure p_i is balanced by the atmospheric pressure p_{atm}, hydrostatic pressure p_h and LaPlace pressure p_γ, i.e.,

$$\begin{aligned} &p_i = p_{atm} + p_h + p_\gamma, where \\ &p_i = p_g + p_v \\ &p_h(z) = \rho_w g z \\ &p_\gamma(r) = \frac{2\gamma}{r} \end{aligned} \qquad \text{B1}$$

where ρ_w is the water density, g is acceleration due to gravity and z is the depth of the bubble in the ocean. The internal pressure is contributed by gas pressure (p_g) and vapour pressure (p_v), the latter of which is often assumed to be negligible. The LaPlace pressure results from surface tension γ (N m^{-1}). Inversely proportional to bubble size, the LaPlace pressure is important for small bubbles. For example, the LaPlace pressure for a bubble with radius of 1 μm is about 0.7 atm, and is 7 atms for bubbles with radii of 0.1 μm. The gas pressure inside a bubble is assumed to follow the perfect gas law

$$p_g V = n_g R T, \qquad \text{B2}$$

where V ($= 4/3\pi r^3$) is the volume of bubble, n_g is the total number of moles of gas inside the bubble, R is the gas constant, and T is the absolute temperature (Kelvin).

For low Reynolds number Re ($Re = \frac{r w_b}{\nu}$ and $Re \approx 1$ for air bubbles of 100 μm in diameter), Stokes law determines the terminal velocity (w_b) of a rising bubble,

$$w_b \approx \frac{2}{9}\frac{r^2 g}{\nu}, \qquad \text{B3a}$$

where ν is the kinematic viscosity. Eq. B3a tends to overestimate the rising speed for large Reynolds number, for which there is no analytical solution for Stokes equation however. Detsch [1991] measured and best-fitted the rise velocities for bubbles between 10 and 500 μm in radius,

$$w_b = -4.17\times10^{-3} + 2.24\times10^{-4} r + 5.68\times10^{-8} r^2 \qquad \text{B3b}$$

where w_b is in m s^{-1} and r in μm. The rising speeds are smaller for dirty bubbles (i.e., with organic coatings) than for clean bubbles of the same size, and bubbles tend to rise faster in fresh water than in seawater. However, these effects are only significant for bubbles greater than 250 μm [*Detsch*, 1991].

The Weber number ($= \frac{2\rho_w w_b^2 r}{\gamma}$), describing the departure from a spherical shape, is only about 0.04 for a bubble of radius 400 μm rising in water. Therefore, for bubbles smaller than 500 μm, the spherical shape does not change very much as a result of rising.

Under equilibrium gas transfer, the gas pressure inside a bubble is equal to the partial pressure of dissolved gas in the ocean, i.e.,

$$p_g = x p_{atm}, \qquad \text{B4}$$

where x is the fractional value of the saturation. Inserting Eq. B1 into Eq. B4 and neglecting vapour pressure, we have

$$x = 1 + \frac{\frac{2\gamma}{r} + \rho_w g z}{p_{atm}}. \qquad \text{B5}$$

Obviously, water has to be supersaturated for a bubble to stay in equilibrium. Normally, the LaPlace and hydrostatic pressure are in excess of supersaturation, a bubble at depth will tend to dissolve. This bubble dissolution results in most surface ocean waters being somewhat supersaturated with nitrogen, argon, and other inert gases [*Blanchard and Woodcock*, 1957].

It is normally assumed that dissolved gas concentration at the bubble wall is in equilibrium with gas inside the bubble (Henry's Law), therefore the diffusion takes place across a layer between the bubble surface and a distant layer,

$$\frac{dn_g}{dt} = -\frac{D_g H_g 4\pi r^2}{\tau}(p_g - x p_{atm}) \qquad \text{B6}$$

where D_g is the molecular diffusion coefficient of the gas and H_g is Henry's Law constant. The thickness of this imaginary layer, τ, varies for clean or dirty bubbles and for different bubble speed [*Levich*, 1962],

$$\tau = \frac{r}{1 + 0.64\, Pe^{\frac{1}{3}}} \qquad \textit{for clean bubbles}$$

$$\tau = \frac{r}{0.46 Pe^{\frac{1}{2}}} \qquad \textit{for coated bubbles, and}. \qquad \text{B7}$$

$$Pe = \frac{r w_b}{D_g}$$

The rate of bubble size change is derived as

$$\frac{dr}{dt} = \frac{\frac{3D_g H_g RT}{\tau}(p_g - xp_{atm}) - r\rho_w g w_b}{3p_g - \frac{2\gamma}{r}} \qquad \text{B8}$$

In the numerator, the first term relates to diffusive processes and the second term relates to changes as a result of vertical advection. Except close to the surface, the rate of bubble size change is largely controlled by diffusive processes [*Thorpe*, 1982]. Since LaPlace pressure is negligible for large bubbles, the dissolution rate is almost constant for large bubbles (> 50 μm).

When the partial pressure of the dissolved gas is less than required by Eq. B5, there will be a gas pressure gradient across the bubble interface, and as a result, the bubble will dissolve. However, as the bubble size decreases, LaPlace pressure increases, so the excess gas partial pressure inside bubble becomes greater. As a consequence, bubbles of 10 μm radius in gas-saturated pure water dissolve completely in about 10 seconds even in the absence of hydrostatic pressure.

B.2 Stable bubbles

As analyzed above, the equilibrium state for bubbles is unstable; any deviation would further accelerate the process. Normally a bubble would either rise to the surface under buoyancy force or dissolve away due to surface tension and hydrostatic pressure. Residence times for such free bubbles are short, typically of the order of seconds or minutes [*Johnson*, 1986].

Water can be cavitated (i.e., formation of bubbles) with stress or pressure fluctuations of around one atmosphere, which is about a thousand times less than the theoretical tensile strength of water; this anomalously low threshold has long been known to be due to bubble nuclei that are present in nearly all liquids [e.g. *Leighton*, 1997].

B.2.1 Observations

Numerous measurements confirm the existence of stable bubbles in natural water [*Turner*, 1961; *Gavrilov*, 1969; *Medwin*, 1970; *Medwin*, 1977; *O'Hern et al.*, 1988]. Gavrilov [1969] found microbubbles of radius from 4 μm to 34 μm with concentration of 10^5 m^{-3} in tap waters left standing over 5 hours. Yount *et al.* [*Yount et al.*, 1984] estimated the density of microbubbles less than 1 μm in distilled water to be on the order of 10^{10} m^{-3}. However, he also suggested that the slope of the distribution is too steep to permit an appreciable number of nuclei with radii greater than 10 μm. Johnson and Cooke [1981] observed bubbles in the laboratory resisting further dissolution and remaining stable for periods sometimes as long as hours or days. Medwin [1970; 1977] measured bubbles between about 15 μm and 300 μm down to 30 m when there were no breaking waves. O'Hern [1988] observed the density of bubbles between 10 μm and 15 μm about 15×10^6 m^{-3} at 3 m and 8×10^6 m^{-3} at 30 m in California coastal waters which had been quiet for several days.

Clearly, bubbles appear to persist longer than would be predicted on theoretical grounds. For a bubble to stay in water, it has to be neutrally buoyant and inhibitive to gas transfer. Therefore, it has to rely on other materials to change the buoyancy, and to stall dissolution. Natural water contains impurities, such as dissolved organic matter and

suspended particles. It is estimated that a clean bubble will adsorb these surfactant materials in seconds [*Detwiler and Blanchard*, 1978; *Yount*, 1979; *Thorpe*, 1982]. It may be that such impurities are responsible for the enhanced persistence of natural bubbles.

B.2.2 Skin model

A variably permeable skin model was proposed such that as a bubble dissolves, an elastic organic surface-active skin which, though initially permeable to gas, became impermeable as the concentration of organic molecules increases on the contracting bubble wall, thus stabilizing the bubble against dissolution [*Yount*, 1979; *Yount*, 1982; *Yount et al.*, 1984]. Bubbles thus stabilized have radii on the order of several microns [*Johnson and Cooke*, 1981].

The thickness of the organic coating for oceanic bubbles ranges from 0.01 μm for lipids such as fatty esters, fatty acids, and fatty alcohols, to 1 μm for proteins such as glycoproteins and proteoglycans [*Glazman*, 1983]. The origin of part of the surfactant complex was identified as a derivative from the chlorophyll a/b protein [*D'Arrigo et al.*, 1984].

Detwiler and Blanchard [1978] found that bubbles with a size as large as 800 μm could be covered by surface-active material in just 12 seconds. It is expected that smaller bubbles will take less time to get a complete coating. Yount [1979] suggested that the time scale for a monolayer to spread across a nucleus of ~ 1 μm in gelatine is of the order of 10^{-7} seconds. In nature, only for a small part of their lifetime may bubbles be considered as clean [*Thorpe*, 1982].

B.2.3 Crevice model

The crevice model [e.g. *Atchley and Prosperetti*, 1989] suggests that if a bubble is contained within small-angled crevices in hydrophobic solid particles, the air-water interface can assume a shape that is concave outward, providing a LaPlace pressure (p_γ changing sign in Eq. B1) that opposes bubble collapse. The radius of curvature will adjust to pressure changes to provide bubble stability.

B.2.4 Particle model

Guided by the observation that bubbles rising in natural seawater quickly become coated with particulate materials, Johnson and Wangersky [1987; see also *Turner*, 1961] developed a model in which microbubble stability is imparted by a monolayer of adsorbed hydrophobic particles. Further dissolution is resisted by compression of the particle layer. However, gas continues to diffuse through inter-particle spaces, causing deformation of each inter-particle air-water interface. Dissolution continues until the mean curvature of each interface produces a LaPlace pressure that opposes further bubble collapse. In their study, silanized quartz particles of 2-3 μm in size were used and bubbles as large as 150 μm were found to be stabilized for periods as long as a week.

B.3 Natural bubble size distributions

The parameters of natural bubble size distributions that are important for examining optical effects are the minimum (r_{min}) and maximum (r_{max}) bubble sizes within which the bubble counts are significant, shape of size distribution, and number density

(N_0). Table B.1 lists these parameters along with other relevant information of the *in situ* bubble measurements using various techniques over the past 40 years.

B.3.1 Minimum and maximum sizes

The minimum size of a bubble population observed in the ocean is about 10 μm given all the available techniques being used (Table B.1, Column 6). This minimum, however, should be interpreted as a resolution limit of the instruments. The holographic technique that was used cannot distinguish a bubble from a particle below 10 μm [*O'Hern et al.*, 1988]. The calibration curve used for the optical reflection method [*Su et al.*, 1988] is valid only for bubbles larger than 10 μm [*Ling and Pao*, 1988]. The acoustic resonance frequency for a 10 μm bubble is about 325 kHz at the surface and will increase with depth (Eq. B14). As listed in Table B.1, the highest frequency that has been used is 200 kHz except in Vagle and Farmer's experiment [*Vagle and Farmer*, 1992], during which one frequency at 400 kHz equivalent to an 8 μm bubble at resonance was used. However, they also suggested that off-resonant contributions from larger bubbles are very large at this frequency (see section B.5 below).

There have been no *in situ* observations for smaller bubbles. As mentioned above, stable bubbles between 1 and 10 μm have been observed in both fresh and sea water, but under laboratory conditions [*Gavrilov*, 1969; *Johnson and Cooke*, 1981]. Yount [1984] estimated about 4×10^{10} m^{-3} cavitation nuclei exist with radii from 0.1 to 1 μm in distilled water. It is expected that seawater will host more bubbles than fresh water [*Cartmill and Su*, 1993; *Haines and Johnson*, 1995].

Immediately after wave breaking, entrained bubbles can be over 1 mm in size [*Deane*, 1997; *Deane*, 1999]. These large bubbles quickly rise to the surface leaving behind a diffuse cloud of microbubbles [*Lamarre and Melville*, 1991]. The measured maximum bubble size for the resident bubble population with some persistence is about several hundred microns (Table 2.1, Column 6).

B.3.2 Shape of bubble size distributions (PDF)

Early bubble measurements using photographic methods [*Kolovayev*, 1976; *Johnson and Cooke*, 1979] suggested a modal distribution with reported peak radii varying between 40 μm and 100 μm (Table B.1 Column 7). This contradicted the acoustical measurements [*Medwin*, 1970; *Medwin*, 1977; *Medwin and Breitz*, 1989] that showed that the bubble density continued to increase as radius decreased from 60 μm to about 30 μm. Walsh and Mulhearn [1987] suggested the photographic observations lack the resolution to count smaller bubbles. But Su *et al.* [1988], using an optical device based on the dark-field specular reflection, confirmed a peak located at about 20 μm. By means of an acoustical-backscatter technique, Farmer and Vagle [1989] measured bubbles between 8 and 130 μm and found peaks between 18 and 22 μm.

However, for the larger part of the modal or entire monotonic distribution, the bubble PDF, $p(r)$, varies following a power law in general, i.e.,

$$p(r) \propto r^{\xi}. \qquad \text{B9}$$

Reported values for the exponent ξ have been between –2 and –7 (Table B.1). The value of ξ was also found to change for small and large portions of the bubble spectrum; the pattern of the variation however, is different for bubbles of different origins.

For wind-generated bubbles, Garrett *et al.* [2000] suggested, based on dimensional analysis, that the initial bubble size spectra has $\xi = -\frac{10}{3}$; dissolution and buoyant ascent will modify the spectra such that the slope is ξ+1 ($\approx$ -2) for bubbles less than 100 μm and is ξ-2 ($\approx$ -5) for larger bubbles. This prediction is consistent with the result observed by Su *et al.* [1988] and Terrill *et al.* [*Terrill et al.*, 1998] under windy conditions. But it disagrees with the data of Medwin and Breitz [1989], which showed values of ξ equal to –4 for bubbles less than 50 μm and –2.6 for large bubbles. Wu [1994] suggested that their data, especially for large bubbles, actually represented newly generated bubbles.

It was also suggested that bubbles from other sources have different size dependencies. The cavitation nuclei (< 60 μm) observed in relatively calm seas [*Medwin*, 1977; *O'Hern et al.*, 1988] have ξ of –4 [*Mulhearn*, 1981]. The bubbles (> 60 μm) formed from biological activities or outgassing from decayed sediment have a slope of –2 [*Medwin*, 1970; *Medwin*, 1977; *Mulhearn*, 1981].

Woolf and Thorpe [1991] found that –4 fit most of the results reasonably well and it was also in agreement with their model simulations.

B.3.3 Number density N_0

The number density of natural bubbles at sea has been found to vary over 4 orders of magnitude from about 10^4 to 10^8 m^{-3}. Immediately beneath breaking waves, values as high as 1.2×10^8 m^{-3} for bubble concentration are recorded [*Deane*, 1997; *Deane*, 1999]. Sustained by continuous injection of bubbles by breaking waves and modified by dissolution and rising, a background bubble population will form [*Johnson*, 1986]. The concentration for the wind-generated background bubble population is observed to vary between 10^5 and 10^7 m^{-3} (Table B.1, column 5).

The number density for wind-generated bubbles depends on wind speed U_{10}, measured at 10 m height, through

$$N_0 \propto U_{10}^{\alpha}. \qquad \text{B10}$$

The exponent α (Table B.1, column 5) was determined to be 3.3 by Crawford and Farmer [1987], and by Leeuw and Cohen [1995], respectively, 3.5 by Walsh and Mulhearn [1987], and 4.5 by Su *et al* [1988]. Wu [1981] found 4.5 best fit the data measured by Johnson and Cooke [1979], and by Kolovayev [1976]. Wu [1988] later suggested a value of 3.5 for the data measured by Thorpe [1982]. The mean value of α is about 4.

High concentrations of bubbles (1.4×10^6 to 1.5×10^7 m^{-3}) were also recorded in calm seas down to 30 m [*Medwin*, 1977; *O'Hern et al.*, 1988]. Interestingly, not only did these bubbles extend to a greater depth, they were also more abundant in general, than wind-generated background bubbles.

B.4 Spatial distribution of bubbles

Small-scale processes (up to tens of meters) in the upper ocean boundary layer [*Thorpe*, 1985] determine the spatial distribution of bubbles after their genesis. While bubbles tend to rise under buoyancy force, natural turbulence distributes the bubbles horizontally or even further downward. Monahan and Lu [1990] gave a descriptive model for the spatial distribution of wind-generated bubbles.

B.4.1 Horizontal distribution

Several observations by Thorpe [1982] and Thorpe and Hall [1983] in coastal waters of northwest Scotland, and by Zedel and Farmer [1991] in the North Pacific, found that when wind speed is higher than about 7 m s^{-1}, bubbles formed an almost continuous layer (also called stratus layer) below the sea surface because intensive and frequent wave breaking can sustain a constant bubble supply. Farmer and Vagle [1989] also observed subsurface bubble layers in the Pacific with wind speed of 10 m s^{-1}, and in the Atlantic with wind speeds of 12-14 m s^{-1}. Wu [1994] suggested the wind-induced shear flow is largely responsible for the formation of a bubble layer, within which bubbles are suspended and dispersed by the longitudinal shear field. The stabilization of bubbles by organic surface coating or adsorption to particles also contributes to the formation of this bubble layer [*Johnson and Cooke*, 1981; *Johnson*, 1986]. The persistent bubble layer can last hours after waves cease breaking and might later evolve into a background bubble population [*Johnson*, 1986; *Monahan and Lu*, 1990].

The lower boundary of the bubble layer is very irregular, corresponding to the bubble plumes injected by breaking waves or carried by Langmuir circulation [*Thorpe*, 1986b; *Zedel and Farmer*, 1991].

The bubble concentration within the subsurface layer varies horizontally, but with a magnitude much less than the vertical variability. Therefore it is sometimes assumed to be horizontally homogeneous [*Monahan and Lu*, 1990].

At low or no wind situations, the frequency of wave breaking is too low to maintain a continuous bubble source; or for bubbles of biological origin, the turbulence is not strong enough to disperse bubbles horizontally. It is expected that bubbles will be concentrated near their respective sources in these situations.

B.4.2 Vertical distribution

Obviously, the deepest depth at which bubbles can be found is related to the position of the bubble source. O'Hern [1988] found a strong correlation between bubble and organism concentration, particularly below the thermocline, which was located at about 30 m. Medwin [1970; 1977] also suggested that bubbles found at depth (> 30 m) were produced by organisms.

When the wind speed is over about 3 m s^{-1}, waves start to break, providing the dominant source of bubbles [*Thorpe*, 1992]. The penetration depth of bubble plumes depends on the wind speed and the concentration of bubbles decreases exponentially with depth [*Wu*, 1981; *Thorpe*, 1982; *Thorpe*, 1986b; *Crawford and Farmer*, 1987]. Once generated, bubbles can be carried further down by Langmuir circulation, forming regularly spaced bubble plumes [*Thorpe*, 1984; *Zedel and Farmer*, 1991].

The mean depth of the bubble layer, or stratus layer, is reported to be 2-4 m for U_{10} = 12-14 m s^{-1} in the Atlantic but 4-5 m for U_{10} = 10 m s^{-1} in the Pacific [*Farmer and Vagle*, 1989], and 1 m for U_{10} = 5.4 m s^{-1} [*Osborn et al.*, 1993].

Bubble plumes superimposed over bubble stratus layers are formed either by new bubble clouds injected by breaking waves or by Langmuir circulation. The maximum depth reported for bubble plumes was quite different, e.g. at the same wind speed of 13 m s^{-1}, it was measured ~12 m by Zedel and Farmer [1991], compared to 20 m by Thorpe [1986b]. Generally, the penetration depth of bubbles is comparable to that of 2.5 –3 times the significant wave height [*Thorpe*, 1986b]. Bubble clouds were seldom observed to penetrate to the depth of the main thermocline [e.g. *Crawford and Farmer*, 1987], which is about the deepest depth that Langmuir circulations reach [*Langmuir*, 1938].

Having analyzed several hundred hours of data, Thorpe [1986a] concluded that the mean depth, d_m (m) at which bubble plumes can be detected increases with wind speed U_{10}, and air-water temperature difference ΔT (K) ($0 \le |\Delta T| < 4$), approximately as

$$d_m = 0.31(1 - 0.1|\Delta T|)(U_{10} - 2.5) \qquad \text{B11}$$

with a standard deviation of 0.5 m. In unstable conditions ($\Delta T < 0$), the bubble clouds tend to have a vertical 'finger-like' structure, reminiscent of thermal plumes, whereas in stable conditions ($\Delta T > 0$) a more 'billow-like' structure is dominant. He also suggested that at wind speeds exceeding 10 m s^{-1}, a non-linear, higher power dependence of d_m on U_{10} may be appropriate and that at large fetch the coefficient may increase from 0.31 to about 0.4.

The bubble concentration decays with depth exponentially, i.e.,

$$N(z) = N_0 \exp(-\frac{z}{z_b}), \qquad \text{B12}$$

where z_b is the decay depth or e-folding depth, which also varies with wind speed. Analyzing bubble data obtained both optically by Johnson and Cooke [1979] and by Kolovayev [1976], and acoustically by Thorpe [1982], Wu [1988] found that z_b could be represented by

$$\begin{aligned} z_b &= 0.4 \quad U_{10} < 7 m s^{-1} \\ z_b &= 0.4 + 0.12(U_{10} - 7) \quad U_{10} \geq 7 m s^{-1} \end{aligned} \qquad \text{B13}$$

The dividing wind velocity coincides with the wind speed at which subsurface bubble layers form. This formula, however, underestimates the value reported by Crawford and Farmer [1987], who found z_b was between 1.0 and 1.5 m for U_{10} = 10 m s^{-1}. A further examination of their data suggests that the higher value is more appropriate for bubble plumes, while Eq. B13 applies to the stratus bubble layer.

B.5 Effect of bubbles on the acoustic properties of the ocean

B.5.1 Resonance frequency

Because of a large difference in the density between water and air, air bubbles in water pulsate under acoustic pressure, and will resemble, for $kr \ll 1$ (where k is the sound wave number), mechanical systems of a mass on a spring with a resonance frequency [*Medwin and Clay*, 1998].

The resonance frequency of a bubble in water depends only on its size and depth through [*Clay and Medwin*, 1977],

$$f_R = \frac{1}{2\pi r}\sqrt{\frac{3\eta(p_{atm} + \rho_w gz)}{\rho_w}} \approx \frac{3.25\sqrt{1+0.1z}}{r}, \qquad \text{B14}$$

where η is the ratio of the heat capacity of the gas at constant pressure to the heat capacity at constant volume. The approximation is derived for $\rho_w = 1.03\times10^3$ kg m^{-3}, $p_{atm} = 10^5$ Pa, and $\eta = 1.4$. Eq. B14 assumes the LaPlace pressure is negligible and the gas vibrates adiabatically; for small bubbles, the LaPlace pressure is important and the oscillation is more nearly isothermal. The two corrections, however, are complicated and to some extent mutually counteracting. It is estimated that the error introduced in Eq. B14 will be more than 10% only for bubbles smaller than 5 μm in radius [*Medwin and Clay*, 1998]. The resonance frequency estimated for bubbles increases with depth. Alternatively, for an acoustic instrument whose frequencies are fixed, the size of bubbles that resonate increases with depth. The resonance frequency will be underestimated if bubbles are organically coated, near the surface, or nonspherical [*Medwin and Clay*, 1998]. The resonance frequency will also change if bubbles are in crevices.

B.5.2 Speed of sound

The speed of sound is determined by

$$c = \frac{Z}{\rho} = \sqrt{\frac{1}{K\rho}}, \qquad \text{B15}$$

where Z (kg m^{-2} s^{-1}) is acoustic impedance, a property of the medium, $K\left(=-\frac{1}{V}\frac{dV}{dp}\ \text{Pa}^{-1}\right)$ is the compressibility of the medium, and ρ is the density of the medium. The values of Z are 400 for air and 1.5×10^6 for water, giving a sound speed of 330 m s^{-1} in air and 1480 m

s^{-1} in water [*Leighton*, 1997]. The compressibility for air is about 17,000 times that of water.

In bubbly water, the density is not expected to change very much. The compressibility K, however, will change, following

$$K = vK_a + (1-v)K_w, \qquad \text{B16}$$

where $v = \int_0^\infty \frac{4}{3}\pi r^3 n(r)dr$ is the void fraction, K_w is the compressibility for bubble-free water, and K_a is the compressibility for air.

Bubbly water is dispersive for sound propagation [*Medwin and Clay*, 1998]. The speed of sound at frequencies above the predominant bubble resonance frequencies is greater than in bubble-free water, while the converse is true for sound at lower frequencies. At frequencies much less than the resonant frequency, the sound speed approaches $\sqrt{\frac{1}{K\rho_w}}$. By measuring sound speed at $f << f_R$, the void fraction can be inferred. For example, at void fraction of $v \sim O(10^{-4})$, the sound speed is roughly halved. At the frequency $f >> f_R$, the sound speed approaches bubble-free sound speed; bubbles do not affect the sound speed if the frequency is high enough.

B.5.3 Acoustic cross sections

The acoustic scattering cross-section for a small bubble ($kr < 1$) of radius r for an insonification of frequency f is

$$\sigma_s = \frac{4\pi r^2}{[(f_R/f)^2 - 1]^2 + \delta^2(f)}, \qquad \text{B17}$$

where f_R is the resonant frequency for bubbles with radius r and δ is the total damping constant, which depends on bubble size (r) and frequency (f), and consists of three components: the re-radiation δ_r, the thermal damping δ_t, and the viscous damping δ_v. At resonance,

$$\delta \approx 0.0025 f^{1/3}. \qquad \text{B18}$$

For example, a 30 μm bubble has a resonance frequency of about 100 KHz (Eq. B14), and its damping constant δ is about 0.1 (Eq. B18), and therefore its total scattering cross section is 400 times larger than its geometrical cross section. Mie theory of light scattering predicts that a rigid spherical particle would have an optical scattering cross section at most 2 times larger than its geometrical cross section. The acoustic absorption and attenuation cross sections are

$$\sigma_a = \sigma_s \frac{\delta_t + \delta_v}{\delta_r}, \quad \sigma_e = \sigma_s \frac{\delta}{\delta_r}. \qquad \text{B19}$$

When $kr << 0.1$, the scattering is almost isotropic, so another useful parameter is the backscattering cross-section (at 180° only, different from backscattering cross-section defined in ocean optics), which is simply the scattering cross section divided by 4π.

For a bubble population, the acoustic scattering cross-section per unit volume (i.e., the scattering coefficient) S_s at the incident acoustic frequency f is

$$S_s(f) = \int_0^\infty \sigma_s(f, r) n(r) dr. \qquad \text{B20}$$

Note the calculations for attenuation or absorption cross sections are similar. The number density of bubbles at the resonant size for the incident frequency is deduced by assuming that contributions by non-resonant bubbles are negligible [*Tate and Spitzer*, 1946],

$$n(r_0) = \frac{S_s(f)\delta(f)}{2\pi^2 r_0^3}. \qquad \text{B21}$$

where r_0 is the resonant size of bubbles for the acoustic frequency f. This, however, will overestimate the bubble density because of excess attenuation or scattering by off-resonant bubbles. The errors thus introduced depend on the actual shape of the bubble size distribution.

Theoretically, the bubble size distribution should be known *a priori* in order to interpret the acoustic measurements of bubbles. Some new methods have been proposed [e.g. *Commander and McDonald*, 1991; *Vagle and Farmer*, 1992], however, each with attached assumptions regarding the bubble size distribution.

The acoustic scattering measurement cannot distinguish a free bubble from bubbles in crevices. The coating on bubbles will also change the resonant frequency. The advantages with acoustic bubble measurement are: 1) large observation volume ~ 1 m^3 [*Medwin*, 1977]; 2) internal check of derived results by simultaneously measuring, say, sound speed and attenuation [*Vagle and Farmer*, 1992; *Terrill and Melville*, 2000].

Year	Investigator	Method	Wind (m/s)	N_0 (m^{-3}), α	r_{min}, r_{max} (μm)	PDF & slope ξ	Depth (m)
1957	Blanchard & Woodcock	Visual count	Breaking waves	$> 2\times10^6$	50, 250	$\xi = -4.7$	Surface
1970	Medwin	Acoustic attenuation, 20 – 200 kHz	< 3-4	$< 6\times10^4$	18, 180	ξ=-4 for r<60 μm, ξ =-2 for r>60μm	< 15
1975	Kolovayev	Photograph	6-13	$< 4\times10^4$	15, 350	Peak at 50 – 100 μm	1.5, 4, 8
1977	Medwin	Acoustic attenuation, 5-160 kHz	< 4	$< 1.4\times10^6$	15, 300	ξ=-4 r<60 μm, ξ=-2 r>60μm	3 - 36
1979	Johnson & Cooke	Photograph	8-10, 11-13	1.6×10^4 – 4.8×10^5	17, 300	Peak at 50 μm, $\xi = -4.5$	0.7- 4
1987	Crawford & Farmer	Acoustic attenuation, 119 kHz	3, 7, 11	2×10^3 – 2×10^5, 3.3	17, 300	Assumed Peak at 50 μm, $\xi = -4$	< 10
1987	Walsh & Mulhearn	Photograph	6 - 14	2×10^3 - 10^5, 3.5	50, 300	ξ= -3.3 - -6 r>100 μm	0.5 – 2
1988	O'Hern *et al.*	Holograph	0 for days	2×10^6 – 1.5×10^7	10, 60	ξ=-4	3 - 30
1988	Su *et al.*	Optical reflection at 125°	9 - 17	10^6 - 10^7, 4.5	10, 200	Peak 20 μm, ξ=-3 20 <r <100, ξ =-5 or –6 r>100 μm.	2 – 21
1989	Farmer & Vagle	Sound speed, 4 freq. 28 - 200 kHz	10 – 14	6×10^3 – 6×10^6	*10, 300*	Peak at 18 – 22 μm, ξ = -4 to –6	< 13
1989	Medwin & Breitz	Acoustic resonator,	12-15, breaking waves	$< 3\times10^6$	30, 270	Overall ξ=-2.7, ξ=-4 r< 50 μm, ξ=-2.6 r> 60 μm	0.25
1992	Vagle & Farmer	Acoustic backscatter, 28, 50, 88, 120, 200, 400 kHz	11	1.6×10^4 – 1.6×10^7	8, 130	Peak at 25 μm, $\xi = -4$ at surface to –7 at depth	< 8
1994	Su & Cartmill	Acoustic resonator, 3 – 99 kHz	11	$< 2\times10^5$	30, 1200	ξ=-4 r< 100 μm, ξ=-3 else	0.25, 3.30
1995	Leeuw & Cohen	CCD camera	6 - 14	$< 1.3\times10^6$, 3.3	30, 1000	Peak at 50 – 70 μm, ξ=-2 to -4	1.5

Year	Investigator	Method	Wind (m/s)	N_0 (m^{-3}), α	r_{min}, r_{max} (μm)	PDF & slope ξ	Depth (m)
1997	Deane	Photograph	Breaking waves	1.2×10^{8}	100, 7500	ξ =-2.5 r< 1000 μm ξ =-4.5 r > 1000 μm	Surf zone
1997	Phelps *et al.*	Acoustic combination frequency, 28 – 88 kHz	11, breaking waves	4×10^{7}	20, 100	ξ=-2	Surf zone
1998	Phelps & Leighton	Acousitc combination frequency, 17 – 200 kHz	10 – 16, breaking waves	2×10^{6}	16, 200	ξ=-4	Surf zone
1998	Terril *et al.*	Sound speed, 4 – 100 kHz	15	7.5×10^{4} – 7.5×10^{6}	30, 800	ξ= -3 r < 100 μm, ξ= -5.7 else	0.7

Table B.1 Historical *in situ* bubble measurements in the global ocean and the summaries of measured bubble size and vertical distributions, total number density, and wind speeds.

References

Ahn, Y.-H., A. Bricaud, and A. Morel, Light backscattering efficiency and related properties of some phytoplankters, *Deep-Sea Res.*, 39 (11/12), 1835-1855, 1992.

Antoine, D., J.-M. André, and A. Morel, Oceanic primary production 2. Estimation at global scale from satellite (coastal zone color scanner) chlorophyll, *Global Biogeochem. Cycles*, 10 (1), 57-69, 1996.

Antoine, D., A. Morel, and J.-M. André, Algal pigment distribution and primary production in the eastern Mediterranean as derived from coastal zone color scanner observations, *J. Geophys. Res.*, 100 (8), 16193-16209, 1995.

Atchley, A.A., and A. Prosperetti, The crevice model of bubble nucleation, *J. Acoust. Soc. Am.*, 86 (3), 1065-1084, 1989.

Austin, R.W., and T.L. Petzold, The determination of the diffuse attenuation coefficient of sea water using the Coastal Zone Color Scanner, in *Oceanography from Space*, edited by J.F.R. Gower, pp. 239-256, Plenum Press, New York, 1981.

Balch, W.M., M.R. Abbott, and R.W. Eppley, Remote sensing of primary production. I. A comparison of empirical and semi-analytical algorithms, *Deep-Sea Res.*, 36 (2), 281-295, 1988.

Balch, W.M., R. Evans, J. Brown, G. Feldman, C.R. McClain, and W.E. Esaias, The remote sensing of ocean primary productivity: Use of a new data compilation to test satellite algorithms, *J. Geophys. Res.*, 97 (2), 2279-2293, 1992.

Balch, W.M., J. Vaughn, J. Novotny, D.T. Drapeau, R. Vaillancourt, J. Lapierre, and A. Ashe, Light scattering by viral suspensions, *Limnol. Oceanogr.*, 45 (2), 492-498, 2000.

Barnard, A.H., W.S. Pegau, and J.R.V. Zaneveld, Global relationship of the inherent optical properties of the oceans, *J. Geophys. Res.*, 103 (C11), 24,955-24,968, 1998.

Barnes, R.A., A.W. Holmes, W.L. Barnes, W.E. Esaias, C.R. McClain, and T. Svitek, SeaWiFS Prelaunch Radiometric Calibration and Spectral Characterization, NASA Technical Memorandum, 1994.

Beardsley, G.F., H.J. Pak, and K.L. Carder, Light scattering and suspended particles in the Eastern Equatorial Pacific ocean, *J. Geophys. Res.*, 75 (15), 2837-2845, 1970.

Behrenfeld, M.J., and P.G. Falkowski, A consumer's guide to phytoplankton primary productivity models, *Limnol. Oceanogr.*, 42, 1479-1491, 1997.

Behrenfeld, M.J., J.T. Randerson, C.R. McClain, G.C. Feldman, S.O. Los, C.J. Tucker, P.G. Falkowski, C.B. Field, R. Frouin, W.E. Esaias, D.D. Kolber, and N.H. Pollack, Biospheric primary production during an ENSO transition, *Science*, 291, 2594-2597, 2001.

Blanchard, D.C., and L.D. Syzdek, Film drop production as a function of bubble size, *J. Geophys. Res.*, 93, 3649-3654, 1988.

Blanchard, D.C., and A.H. Woodcock, Bubble formation and modification in the sea and its meteorological significance, *Tellus*, 9, 145-158, 1957.

Bogucki, D.J., J.A. Domaradzki, D. Stramski, and J.R.V. Zaneveld, Comparison of near-forward light scattering on oceanic turbulence and particles, *Appl. Opt.*, 37 (21), 4669-4677, 1998.

Bohren, C.F., and D.R. Huffman, *Absorption and scattering of light by small particles*, 530 pp., John Wiley & Sons, New York, 1983.

Bricaud, A., A. Morel, M. Babin, K. Allali, and H. Claustre, Variations of light absorption by suspended particles with chlorophyll a concentration in oceanic (case 1) waters: Analysis and implication for bio-optical models, *J. Geophys. Res.*, 103 (C13), 31,033-31,044, 1998.

Bricaud, A., A. Morel, and L. Prieur, Absorption by dissolved organic matter of the sea (yellow substance) in the UV and visible domains, *Limnol. Oceanogr.*, 26 (1), 43-53, 1981.

Bricaud, A., C. Roesler, and J.R.V. Zaneveld, In situ methods for measuring the inherent optical properties of ocean waters, *Limnol. Oceanogr.*, 40 (2), 393-410, 1995.

Brown, O.B., and H.R. Gordon, Two component Mie scattering models of Sargasso Sea particles, *Appl. Opt.*, 17, 2461-2465, 1973.

Brown, O.B., and H.R. Gordon, Size-refractive index distribution of clear coastal water particulates from light scattering, *Appl. Opt.*, 13, 2874-2881, 1974.

Cartmill, J., and M.-Y. Su, Bubble size distribution under saltwater and freshwater breaking waves, *Dynamics of Atmospheres and Oceans*, 20, 25-31, 1993.

Chavez, F.P., P.G. Strutton, G.E. Friederich, R.A. Feely, G.C. Feldman, D.G. Foley, and M.J. McPhaden, Biological and Chemical Response of the Equatorial Pacific Ocean to the 1997-98 El Nino, *Science*, 286, 2126-2131, 1999.

Claustre, H., A. Morel, M. Babin, C. Cailiau, D. Marie, J.-C. Marty, D. Tailliez, and D. Vaulot, Variability in particle attenuation and chlorophyll fluorescence in the tropical Pacific: Scales, patterns, and biogeochemical implications, *J. Geophys. Res.*, 104 (C2), 3401-3422, 1999.

Clay, C.S., and H. Medwin, *Acoustical Oceanography: Principles and Applications*, 544 pp., John Wiley & Sons, New York, 1977.

Commander, K.W., and R.J. McDonald, Finite-element solution of the inverse problem in bubble swarm acoustics, *J. Acoust. Soc. Am.*, 31, 592-597, 1991.

Commander, K.W., and E. Moritz, Off-resonance contributions to acoustical bubble spectra, *J. Acoust. Soc. Am.*, 85 (6), 2665-2669, 1989.

Crawford, G.B., and D.M. Farmer, On the spatial distribution of ocean bubbles, *J. Geophys. Res.*, 92, 8231-8243, 1987.

D'Arrigo, J.S., C. Saiz-Jimenez, and N.S. Reimer, Geochemical properties and biochemical composition of the surfactant mixture surrounding natural microbubbles in aqueous media, *J. Colloid Interface Sci.*, 100 (1), 96-105, 1984.

Davis, G.E., Scattering of light by an air bubble in water, *J. Opt. Soc. Am.*, 45 (7), 572-581, 1955.

Deane, G.B., Sound generation and air entrainment by breaking waves in the surf zone, *J. Acoust. Soc. Am.*, 192 (5), 2671-2689, 1997.

Deane, G.B., Air entrainment processes and bubble size distribution in the surf zone, *J. Phys. Oceanogr.*, 29, 1393-1403, 1999.

Debnath, L., *Nonlinear Water Waves*, 544 pp., Academic Press, Boston, 1994.

Detsch, R.M., Small air bubbles in reagent grade water and seawater 1. Rise velocities of 20- to 1000-μm-diameter bubbles, *J. Geophys. Res.*, 96 (C5), 8901-8906, 1991.

Detwiler, A., and D.C. Blanchard, Aging and bursting bubbles in trace-contaminated water, *Chem. Eng. Sci.*, 33, 9-13, 1978.

Dugdale, R.C., A. Morel, A. Bricaud, and F.P. Wilkerson, Modeling new production in upwelling centers: A case study of modeling new production from remotely sensed temperature and color, *J. Geophys. Res.*, 94 (12), 18119-18132, 1989.

Dumbrell, H.A., Comparison of excess attenuation and backscatter measurements of ship wakes, in *Natural Physical Processes associated with Sea Surface Sound*, edited by T.G. Leighton, pp. 171-178, University of Southampton, Southampton, 1997.

Ezerskii, A.B., B.M. Sandler, and D.A. Selivanovskii, Echo-ranging observations of gas bubbles near the sea surface, *Sov. Phys. Acoust.*, 35 (5), 483-485, 1989.

Farmer, D.M., C.L. McNeil, and B.D. Johnson, Evidence for the importance of bubbles in increasing air-sea gas flux, *Nature*, 361, 620-623, 1993.

Farmer, D.M., and S. Vagle, Waveguide propagation of ambient sound in the ocean-surface bubble layer, *J. Acoust. Soc. Am.*, 86 (5), 1897-1808, 1989.

Feldman, G.C., D. Clark, and D. Halpern, Satellite color observations of the plankton distribution in the eastern equatorial Pacific during the 1982-1983 El Niño, *Science*, 226 (1069-1070), 1984.

Field, C.B., M.J. Behrenfeld, J.T. Randerson, and P.G. Falkowski, Primary production of the biosphere: integrating terrestrial and oceanic components, *Science*, 281, 237-240, 1998.

Fielder, P.C., Satellite observations of the 1982-1983 El Niño along the U.S. Pacific Coast, *Science*, 224, 1251-1254, 1984.

Fournier, G.R., and J.L. Forand, Analytical phase function for ocean water, *SPIE Ocean Optics XII*, 2258, 194-201, 1994.

Frouin, R., M. Schwindling, and P.-Y. Deschamps, Spectral reflectance of sea foam in the visible and near-infrared: In situ measurements and remote sensing implications, *J. Geophys. Res.*, 101 (C6), 14,361-14,371, 1996.

Garrett, C., M. Li, and D.M. Farmer, The connection between bubble size spectra and energy dissipation rates in the upper ocean, *J. Phys. Oceanogr.*, 30, 2163-2171, 2000.

Gavrilov, L.R., On the size distribution of gas bubbles in water, *Sov. Phys. Acoust.*, 15 (1), 22-24, 1969.

Glazman, R.E., Effects of adsorbed films on gas bubble radial oscillations, *J. Acoust. Soc. Am.*, 74, 980-986, 1983.

Gordon, H.R., Dependence of the diffuse reflectance of natural waters on the Sun angle, *Limnol. Oceanogr.*, 34, 1484-1489, 1989.

Gordon, H.R., Diffuse reflectance of the ocean: influence of nonuniform phytoplankton pigment profile, *Appl. Opt.*, 31 (12), 2116-2129, 1992.

Gordon, H.R., Sensitivity of radiative transfer to small-angle scattering in the ocean: Quantitative assessment, *Appl. Opt.*, 32 (36), 7505-7511, 1993.

Gordon, H.R., Atmospheric correction of ocean color imagery in the Earth Observing System era, *J. Geophys. Res.*, 102 (D14), 17,081-17,106, 1997.

Gordon, H.R., and O.B. Brown, A theoretical model of light scattering by Sargasso Sea particulates, *Limnol. Oceanogr.*, 17, 826-832, 1972.

Gordon, H.R., O.B. Brown, R.H. Evans, J.W. Brown, R.C. Smith, K.S. Baker, and D.K. Clark, A semianalytic radiance model of ocean color, *J. Geophys. Res.*, 93 (9), 10909-10924, 1988.

Gordon, H.R., O.B. Brown, and M.M. Jacobs, Computed relationships between the inherent and apparent optical properties of a flat homogeneous ocean, *Appl. Opt.*, 14 (2), 417-427, 1975.

Gordon, H.R., and A. Morel, *Remote Assessment of Ocean Color for Interpretation of Satellite Visible Imagery, a Review*, 114 pp., Springer-Verlag, New York, 1983.

Gordon, H.R., and M. Wang, Influence of oceanic whitecaps on atmospheric correction of ocean-color sensors, *Appl. Opt.*, 33 (33), 7754-7763, 1994a.

Gordon, H.R., and M. Wang, Retrieval of water-leaving radiance and aerosol optical thickness over the oceans with SeaWiFS: a preliminary algorithm, *Appl. Opt.*, 33 (3), 443-452, 1994b.

Haines, M.A., and B.D. Johnson, Injected bubble populations in seawater and fresh water measured by a photographic method, *J. Geophys. Res.*, 100 (C4), 7057-7068, 1995.

Hennings, I., R. Romeiser, W. Alpers, and A. Viola, Radar imaging of Kelvin arms of ship wakes, *Int. J. Remote Sensing*, 20 (13), 2519-2543, 1999.

Hovis, W.A., D.K. Clark, F. Anderson, R.W. Austin, W.H. Wilson, E.T. Baker, D. Ball, H.R. Gordon, J.L. Muller, S.Z. El-Sayed, B. Sturm, R.C. Wrigley, and C.S. Yentsch, Nimbus-7 Coastal Zone Color Scanner: System description and initial imagery, *Science*, 210 (3), 60-63, 1980.

IOCCG, *Medium Resolution Ocean Colour Sensors*, http://www.ioccg.org/sensors/500m.html, January, 2001.

Johnson, B.D., Bubble populations: Background and breaking waves, in *Oceanic Whitecaps and their role in air-sea exchange processes*, edited by E.C. Monahan, and G. Mac Niocail, pp. 69-73, D. Reidel, Dordrecht, Holland, 1986.

Johnson, B.D., and R.C. Cooke, Bubble populations and spectra in coastal waters. A photographic approach, *J. Geophys. Res.*, 84, 3761-3766, 1979.

Johnson, B.D., and R.C. Cooke, Organic particle and aggregate formation resulting from the dissolution of bubbles in seawater, *Limnol. Oceanogr.*, 25 (4), 653-661, 1980.

Johnson, B.D., and R.C. Cooke, Generation of stabilized microbubbles in seawater, *Science*, 213, 209-211, 1981.

Johnson, B.D., and R.M. Gershey, Bubble formation at a cylindrical frit surface in a shear field, *Chem. Eng. Sci.*, 46 (10), 2753-2756, 1991.

Johnson, B.D., and P.J. Wangersky, Microbubbles: stabilization by monolayers of adsorbed particles, *J. Geophys. Res.*, 92, 14641-14647, 1987.

Kirk, J.T.O., Monte Carlo study of the nature of the underwater light field in, and relationships between optical proterties of, turbid yellow waters, *Aust. J. Mar. Freshwater Res.*, 32, 517-532, 1981.

Kirk, J.T.O., Dependence of relationship between inherent and apparent optical properties of water on solar altitude, *Limnol. Oceanogr.*, 29 (2), 350-356, 1984.

Koepke, P., Effective reflectance of oceanic whitecaps, *Appl. Opt.*, 23 (11), 1816-1824, 1984.

Koepke, P., Remote sensing signatures of whitecaps, in *Oceanic Whitecaps and Their Role in Air-Sea Exchange Processes*, edited by E.C. Monahan, and G.M. Niocaill, pp. 251-260, D. Reidel Publishing, Boston, 1986.

Koga, M., Bubble entrainment in breaking wind waves, *Tellus*, 34, 481-189, 1982.

Kolovayev, D.A., Investigation of the concentration and statistical size distribution of wind-produced bubbles in the near-surface ocean, *Oceanology. Eng. Trans.*, 15, 659-661, 1976.

Kullenberg, G., Scattering of light by Sargasso Sea water, *Deep-Sea Res.*, 15, 423-432, 1968.

Lamarre, E., and W.K. Melville, Air entrainment and dissipation in breaking waves, *Nature*, 351, 469-472, 1991.

Langmuir, I., Surface motion of water induced by wind, *Science*, 87 (2250), 119-123, 1938.

Lee, M.E., and M.R. Lewis, New principles of measurements of volume scattering function over wide range of scattering angles in sea water, *in preparation of submittal to Journal of Atmospheric and Oceanic Technology*, 2001.

Leeuw, G.d., and L.H. Cohen, Bubble size distribution in coastal seas, in *Air-Water Gas Transfer*, edited by B. Jahne, and E.C. Monahan, AEON Verlag & Studio, Hanau, 1995.

Leighton, T.G., *The Acousitc Bubble*, 613 pp., Academic Press, San Diego, 1997.

LEO-15, *LEO-15 Longterm Ecosystem Observatory*, http://marine.rutgers.edu/mrs/LEO15.html, March, 2001.

Levich, V.G., *Physicochemical Hydrodynamics*, 700 pp., Prentice-Hall, Englewood Cliffs, N.J., 1962.

Lewis, M.R., Satellite ocean color observations of global biogeochemical cycles, in *Primary Productivity and Biogeochemical Cycles in the Sea*, edited by P.G. Falkowski, and A.D. Woodhead, pp. 139-154, Plenum Press, New York, 1992.

Lewis, M.R., M.-E. Carr, G.C. Feldman, W.E. Esaias, and C.R. McClain, Influence of penetrating solar radiation on the heat budget of the equatorial Pacific Ocean, *Nature*, 347 (6293), 543-545, 1990.

Lewis, M.R., J.J. Cullen, and T. Platt, Phytoplankton and thermal structure in the upper ocean: consequences of nonnuiformity in chlorophyll profile, *J. Geophys. Res.*, 88, 2565-2570, 1983.

Ling, S.C., and H. Pao, P., Study of micro-bubbles in the North Sea, in *Sea Surface Sound*, edited by B.R. Kerman, pp. 197-210, Kluwer Academic Publishers, New Yorke, 1988.

Loisel, H., and A. Morel, Light scattering and chlorophyll concentration in case 1 waters: A reexamination, *Limnol. Oceanogr.*, 34 (5), 847-858, 1998.

Lyden, J.D., R.R. Hammond, D.R. Lyzenga, and R.A. Shuchman, Synthetic aperture radar imaging of surface ship wakes, *J. Geophys. Res.*, 93 (C10), 12,293-12,303, 1988.

Maffione, R.A., and D.R. Dana, Instruments and methods for measuring the backward-scattering coefficient of ocean water, *Appl. Opt.*, 36 (24), 6057-6067, 1997.

Maffione, R.A., and R.C. Honey, Instrument for measuring the volume scattering function in the backward direction, *SPIE Ocean Optics XI*, 1750, 15-26, 1992.

Marston, P.L., Critical angle scattering by a bubble: physical-optics approximation and observations, *J. Opt. Soc. Am.*, 69 (9), 1205-1211, 1979.

Marston, P.L., B. Billette, and C. Dean, Scattering of light by a coated bubble in water near the critical and Brewster scattering angles, *SPIE 925 Ocean Optics IX*, 925, 308-316, 1988.

McClain, C.R., Review of major CZCS applications: U.S. case studies, in *Ocean Colour: Theory and Applications in a Decade of CZCS Experience*, edited by V. Barale, and P.M. Schlittenhaidt, pp. 167-188, ECSC, EEC, EAEC, Brussels and Luxembourg, 1993.

McGlynn, J.D., S.R. Stewart, and D.J. Witte, Advances in sensing and detection of thermal infrared ship wakes, in *Oceans' 90: Engineering in the Ocean Environment*, edited by I.O.E. Society, pp. 591, Washington D. C., 1990.

Medwin, H., *In situ* acoustic measurements of bubble populations in coastal ocean waters, *J. Geophys. Res.*, 75 (599-611), 1970.

Medwin, H., *In situ* acoustic measurements of microbubbles at sea, *J. Geophys. Res.*, 82, 971-976, 1977.

Medwin, H., and N.D. Breitz, Ambient and transient bubble spectral densities in quiescent seas and under spilling breakers, *J. Geophys. Res.*, 94, 12751-12759, 1989.

Medwin, H., and C.S. Clay, *Fundamentals of Acoustical Oceanography*, 712 pp., Academic Press, San Diego, 1998.

Messinó, D., D. Sette, and F. Wanderlingh, Statistical approach to ultrasonic cavitation, *J. Acoust. Soc. Am.*, 35 (10), 1575-1583, 1963.

Mitchell, B.G., Coastal zone color scanner retrospective, *J. Geophys. Res.*, 99 (C4), 7291-7292, 1994.

Mobley, C.D., *Light and water: radiative transfer in natural waters*, 592 pp., Academic Press, San Diego, 1994.

Mobley, C.D., L.K. Sundman, and E. Boss, Phase function effects on oceanic light fields, *Submitted to Applied Optics*, 2001.

Monahan, E.C., The ocean as a source for atmospheric particles, in *The Role of Air-Sea Exchange in Geochemical Cycling*, edited by P. Buat-Menard, pp. 129-163, Reidel, Dordrecht, Holland, 1986.

Monahan, E.C., and H.G. Dam, Bubbles: An estimate of their role in the global oceanic flux of carbon, *J. Geophys. Res.*, 106 (C5), 9377-9383, 2001.

Monahan, E.C., and M. Lu, Acoustically relevant bubble assemblages and their dependence on meteorological parameters, *IEEE Journal of Oceanic Engineering*, 15 (4), 340-349, 1990.

Moore, K.D., K.J. Voss, and H.R. Gordon, Spectral reflectance of whitecaps: Their contribution to water-leaving radiance, *J. Geophys. Res.*, 105 (C3), 6493-6499, 2000.

Morel, A., The scattering of light by seawater: Experimental results and theoretical approach, pp. 161, AGARD, NATO, 1973.

Morel, A., Optical properties of pure water and pure sea water, in *Optical Aspects of Oceanography*, edited by N.G. Jerlov, and E.S. Nielsen, pp. 1-24, Academic Press, New York, 1974.

Morel, A., Optical modeling of the upper ocean in relation to its biogenous matter content (Case I waters), *J. Geophys. Res.*, 93 (C9), 10749-10768, 1988.

Morel, A., Light and marine photosynthesis: A spectral model with geochemical and climatological implications, *Prog. Oceanogr.*, 26, 263-306, 1991a.

Morel, A., Optics of marine particles and marine optics, in *Particle Analysis in Oceanography*, edited by S. Demers, pp. 141-188, Springer-Verlag, New York, 1991b.

Morel, A., and Y.-H. Ahn, Optics of heterotrophic nanoflagellates and ciliates: A tentative assessment of their scattering role in oceanic waters compared to those of bacterial and algal cells, *J. Mar. Res.*, 49, 177-202, 1991.

Morel, A., and A. Bricaud, Theoretical results concerning the optics of phytoplankton, with special reference to remote sensing application, in *Oceanography from Space*, edited by J.F.R. Gower, pp. 313-327, Plenum Press, New York, 1981.

Morel, A., and B. Gentili, Diffuse reflectance of oceanic waters: its dependence on Sun angle as influenced by the molecular scattering contribution, *Appl. Opt.*, 30 (30), 4427-4438, 1991.

Morel, A., and B. Gentili, Diffuse reflectance of oceanic waters. II. Bidirectional aspects, *Appl. Opt.*, 32 (33), 6864-6879, 1993.

Morel, A., and B. Gentili, Diffuse reflectance of oceanic waters. III. Implication of bidirectionality for the remote-sensing problem, *Appl. Opt.*, 35 (24), 4850-4862, 1996.

Morel, A., and S. Maritorena, Bio-optical properties of oceanic waters: A reappraisal, *J. Geophys. Res.*, 106 (C4), 7163-7180, 2001.

Morel, A., and L. Prieur, Analysis of variations in ocean color, *Limnol. Oceanogr.*, 22 (4), 709-722, 1977.

Mulhearn, P.J., Distribution of microbubbles in coastal waters, *J. Geophys. Res.*, 86, 6429-6434, 1981.

O'Hern, T.J., L. d'Agostino, and A.J. Acosta, Comparison of holographic and Coulter counter measurement of cavitation nuclei in the ocean, *J. Fluids Eng.*, 110, 200-207, 1988.

Oishi, T., Significant relationship between the backward scattering coefficient of sea water and the scatterance at 120°, *Appl. Opt.*, 29 (31), 4658-4665, 1990.

O'Reilly, J.E., S. Maritorena, B.G. Mitchell, D.A. Siegel, K.L. Carder, S.A. Garver, M. Kahru, and C.R. McClain, Ocean color chlorophyll algorithm for SeaWiFS, *J. Geophys. Res.*, 103 (C11), 24,937-24,953, 1998.

Osborn, T., S. Vagle, M. Cure, and A.J. Hall, Bubble plumes and turbulence, in *Natural Physical Sources of Underwater Sound*, edited by B.R. Kerman, pp. 519-525, Kluwer Academic, Netherlands, 1993.

Pegau, W.S., J.R.V. Zaneveld, and K.J. Voss, Toward closure of the inherent optical properties of natural waters, *J. Geophys. Res.*, 100 (C7), 13,193-13,199, 1995.

Peltzer, R.D., O.M. Griffin, W.R. Barger, and J.A.C. Kaiser, High-resolution measurement of surface-active film redistribution in ship wakes, *J. Geophys. Res.*, 97 (C4), 5231-5252, 1992.

Pernetta, J.C., and J.D. Milliman, Land-Ocean Interactions in the Coastal Zone: Implementation Plan, pp. 215, IGBP Global Change Report, 1995.

Petzold, T.J., Volume scattering function for selected ocean waters, pp. 79, Scripps Institute of Oceanography, La Jolla, 1972.

Platt, T., C.M. Caverhill, and S. Sathyendranath, Basin-scale estimates of oceanic primary production by remote sensing: The North Atlantic, *J. Geophys. Res.*, 96 (8), 15147-15159, 1991.

Platt, T., S. Sathyendranath, C.M. Caverhill, and M.R. Lewis, Ocean primary production and available light: further algorithms for remote sensing, *Deep-Sea Res.*, 35 (6), 855-879, 1988.

Pope, R.M., and E.S. Fry, Absorption spectrum (380-700 nm) of pure water. II. Integrating cavity measurements, *Appl. Opt.*, 36 (33), 8710-8723, 1997.

Preisendorfer, R.W., *Hydrologic Optics: Foundations*, 400 pp., Pacific Mar. Environ. lab/NOAA, Seattle, 1976a.

Preisendorfer, R.W., *Hydrologic Optics: Introduction*, 218 pp., Pacific Mar. Environ. lab/NOAA, Seattle, 1976b.

Pumphrey, H.C., and P.A. Elmore, The entrainment of bubbles by drop impacts, *J. Fluid Mech.*, 220, 539-567, 1990.

Reed, A.M., R.F. Beck, O.M. Griffin, and R.D. Peltzer, Hydrodynamics of remotely sensed surface ship wakes, *SNAME Transactions*, 98, 319-363, 1990.

Rey, M., J.K.E. Tunaley, and T. Sibbald, Use of the Dempster-Shafer algorithm for the detection of SAR ship wakes, *IEEE Trans. Geosci. Remote Sensing*, 31 (5), 1114-1118, 1993.

Sathyendranath, S., Remote Sensing of Ocean Colour in Coastal, and Other Optically-Complex, Waters, pp. 140, International Ocean-Colour Coordinating Group, 2000.

Sathyendranath, S., A.D. Gouveia, S.R. Shetye, P. Ravindran, and T. Platt, Biological control of surface temperature in the Arabian Sea, *Nature*, 349, 54-56, 1991a.

Sathyendranath, S., T. Platt, E.P.W. Horne, W.G. Harrison, O. Ulloa, R. Outerbridge, and N. Hoepffner, Estimation of new production in the ocean by compound remote sensing, *Nature*, 353 (12), 129-133, 1991b.

Shedmin, O.H., Synthetic aperture radar imaging of ship wakes in the Gulf of Alaska, *J. Geophys. Res.*, 95 (C9), 16,319-16,338, 1990.

Shemer, L., L. Kagan, and G. Zilman, Simulation of ship wakes image by an along-track interferometric SAR, *Int. J. Remote Sensing*, 17 (18), 3577-3597, 1996.

Siegel, D.A., M. Wang, S. Maritorena, and W. Robinson, Atmospheric correction of satellite ocean color imagery: the black pixel assumption, *Appl. Opt.*, 39 (21), 3582-3591, 2000.

Smith, R.C., and K.S. Baker, Optical properties of the clearest natural waters, *Appl. Opt.*, 20 (2), 177-184, 1981.

Smith, R.C., and K.S. Baker, Oceanic chlorophyll concentrations as determined by satellite (Nimbus-7 coastal zone color scanner), *Mar. Biol.*, 66, 269-279, 1982.

Stabeno, P.J., and E.C. Monahan, The influence of whitecaps on the albedo of the sea surface, in *Oceanic Whitecaps and Their Role in Air-Sea Exchange Processes*, edited by E.C. Monahan, and G.M. Niocaill, pp. 261-266, D. Reidel Publishing, Boston, 1986.

Stapleton, N.R., Ship wakes in radar imagery, *Int. J. Remote Sensing*, 18 (6), 1381-1386, 1997.

Stramski, D., Gas microbubbles: An assessment of their significance to light scattering in quiescent seas, *SPIE Ocean Optics XII*, 2258 (Ocean Optics XII), 704-710, 1994.

Stramski, D., and D.A. Kiefer, Light scattering by microorganisms in the open ocean, *Prog. Oceanogr.*, 28, 343-383, 1991.

Su, M.Y., and J. Cartmill, Low-frequency underwater sound speed variations due to oceanic bubbles, in *Sea Surface Sound '94*, edited by M.J. Buckingham, and J.R. Potter, pp. 351-365, World Scientific, Singapore, 1994.

Su, M.Y., S.C. Ling, and J. Cartmill, Optical microbubble measurements in the North Sea, in *Sea Surface Sound*, edited by B.R. Kerman, pp. 211-223, Kluwer Academic Publishers, New York, 1988.

Su, M.Y., D. Todoroff, and J. Cartmill, Laboratory comparison of acoustic and optical sensors for microbubble measurement, *J. Atmos. Ocean Tech.*, 11, 170-181, 1994.

Tate, J.T., and L.J. Spitzer, Physics of Sound in the Sea: Summary Technical Report of Division 6, pp. 566, U.S. Government Printing Office, Washington D.C., 1946.

Terrill, E.J., and W.K. Melville, A broadband acoustic technique for measuring bubble size distributions: laboratory and shallow water measurements, *J. Atmos. Ocean Tech.*, 17, 220-239, 2000.

Terrill, E.J., W.K. Melville, and D. Stramski, Bubble entrainment by breaking waves and their effects on the inherent optical properties of the upper ocean, in *Ocean Optics XIV*, Kailua-Kona, Hawaii, USA, 1998.

Terrill, E.J., W.K. Melville, and D. Stramski, Bubble entrainment by breaking waves and their influence on optical scattering in the upper ocean, *J. Geophys. Res.*, 106 (C8), 16,815-16,823, 2001.

Thorpe, S.A., On the clouds of bubbles formed by breaking wind waves in deep water, and their role in air-sea transfer, *Phil. Trans. R. Soc. Lond. A*, 304, 155-210, 1982.

Thorpe, S.A., The effect of Langmuir circulation on the distribution of submerged bubbles caused by breaking wind waves, *J. Fluid Mech.*, 142, 151-170, 1984.

Thorpe, S.A., Small-scale processes in the upper ocean boundary layer, *Nature*, 318 (12), 519-522, 1985.

Thorpe, S.A., Bubble clouds: A review of their detection by sonar, of related models, and of how K_v may be determined, in *Oceanic Whitecaps*, edited by E.C. Monahan, and G.M. Niocaill, pp. 57-68, D. Reidel Publishing, Dordrecht, 1986a.

Thorpe, S.A., Measurements with an automatically recording inverted echo sounder; ARIES and the bubble clouds, *J. Phys. Oceanogr.*, 16, 1462-1478, 1986b.

Thorpe, S.A., Bubble clouds and the dynamics of the upper ocean, *Quarterly Journal of the Royal Meteorological Society*, 118 (503), 1-22, 1992.

Thorpe, S.A., and A.J. Hall, The characteristics of breaking waves, bubble clouds, and near-surface currents observed using side-scan sonar, *Continental Shelf Research*, 1 (4), 353-384, 1983.

Thorpe, S.A., and P.N. Humphries, Bubbles and breaking waves, *Nature*, 283, 463-465, 1980.

Trevorrow, M.V., S. Vagle, and D.M. Farmer, Acoustical measurements of microbubbles within ship wakes, *J. Acoust. Soc. Am.*, 95 (4), 1922-1930, 1994.

Turner, W.R., Microbubbles persistence in fresh water, *J. Acoust. Soc. Am.*, 33 (9), 1223-1233, 1961.

Ulloa, O., S. Sathyendranath, and T. Platt, Effect of the particle-size distribution on the backscattering ratio in seawater, *Appl. Opt.*, 33 (30), 7070-7077, 1994.

Ulloa, O., S. Sathyendranath, T. Platt, and R.A. Quiñones, Light scattering by marine heterotrophic bacteria, *J. Geophys. Res.*, 97 (C6), 9619-9629, 1992.

Urick, R.J., *Ambient Noise in the Sea*, 205 pp., Peninsula Publishing, 1986.

Vagle, S., and D.M. Farmer, The measurement of bubble-size distributions by acoustical backscatter, *J. Atmos. Ocean Tech.*, 9, 630-644, 1992.

Walsh, A.L., and P.J. Mulhearn, Photographic measurements of bubble populations from breaking wind waves at sea, *J. Geophys. Res.*, 92, 14553-14565, 1987.

Whitlock, C.H., D.S. Bartlett, and E.A. Gurganus, Sea foam reflectance and influence on optimum wavelength for remote sensing of ocean aerosols, *Geophys. Res. Let.*, 9 (6), 719-722, 1982.

Woolf, D.K., and S.A. Thorpe, Bubbles and the air-sea exchange of gases in near-saturation conditions, *J. Mar. Res.*, 49, 435-466, 1991.

Wu, J., Bubble population and spectra in near surface ocean: Summary and review of field measurements, *J. Geophys. Res.*, 86, 457-463, 1981.

Wu, J., Bubbles in the near surface ocean: A general description, *J. Geophys. Res.*, 93, 587-590, 1988.

Wu, J., Individual characteristics of whitecaps and volumetric description of bubbles, *IEEE Journal of Oceanic Engineering*, 17 (1), 150-158, 1992.

Wu, J., Bubbles in the near-surface ocean: Their various structures, *J. Phys. Oceanogr.*, 24, 1955-1965, 1994.

Xu, W., M.H. Jericho, I.A. Meinertzhagen, and H.J. Kreuzer, Digital in-line holography for biological applications, *PNAS*, 98 (20), 11301-11305, 2001.

Yoder, J.A., C.R. McClain, G.C. Feldman, and W.E. Esaias, Annual cycles of phytoplankton chlorophyll concentrations in the global oceans: A satellite view, *Global Biogeochem. Cycles*, 7, 181-193, 1993.

Yount, D.E., Skins of varying permeability. A stablization mechanism for gas cavitation nuclei, *J. Acoust. Soc. Am.*, 65, 1429-1439, 1979.

Yount, D.E., On the evolution, generation, and regeneration of gas cavitation nuclei, *J. Acoust. Soc. Am.*, 71 (6), 1473-1481, 1982.

Yount, D.E., E.W. Gillary, and D.C. Hoffman, A microscopic investigation of bubble formation nuclei, *J. Acoust. Soc. Am.*, 76, 1511-1521, 1984.

Zaneveld, J.R.V., A theoretical derivation of the dependence of the remotely sensed reflectance of the ocean on the inherent optical properties, *J. Geophys. Res.*, 100 (C7), 13,135-13,142, 1995.

Zaneveld, J.R.V., and J.C. Kitchen, The variation in the inherent optical properties of phytoplankton near an absorption peak as determined by various models of cell structure, *J. Geophys. Res.*, 100 (C7), 13,309-13,320, 1995.

Zedel, L., and D.M. Farmer, Organized structures in subsurface bubble clouds: Langmuir circulation in the open ocean, *J. Geophys. Res.*, 96 (C5), 8889-8900, 1991.

Zhang, X., Light Scattering by Microbubbles in the Ocean, Master thesis, Dalhousie University, Halifax, 1998.

Zhang, X., M.R. Lewis, and B.D. Johnson, Influence of bubbles on scattering of light in the ocean, *Appl. Opt.*, 37 (27), 6525-6536, 1998.

Zhang, X., M.R. Lewis, M. Lee, B.D. Johnson, and G. Korotaev, Volume Scattering Function of Bubbles, *submitted to Limnology and Oceanography*, 2001.